

MARINE GAS HYDRATES: SEISMIC ANALYSES AND THERMAL REGIME

By

Nilanjan Ganguly

B.Sc. Indian Institute of Technology, Kharagpur, India, 1994

M.Sc. Indian Institute of Technology, Kharagpur, India, 1996

A Thesis Submitted in Partial Fulfillment of the
Requirement for the Degree of

MASTER OF SCIENCE

In the School of Earth and Ocean Sciences
University of Victoria

We accept this thesis as conforming to the required standard

[Redacted Signature]

Dr. George D. Spence, Co-supervisor (School of Earth and Ocean Sciences)

[Redacted Signature]

Dr. N. Ross Chapman, Co-supervisor (School of Earth and Ocean Sciences)

[Redacted Signature]

Dr. Roy D. Hyndman, Member (Pacific Geoscience Centre, Geological Survey of Canada)

[Redacted Signature]

Dr. Earl E. Davis, External Examiner (Pacific Geoscience Centre, Geological Survey of Canada)

© Nilanjan Ganguly, 1998
University of Victoria

All rights reserved. This thesis may not be reproduced in whole or part, by photocopy or other means, without the permission of the author.

Supervisors: Dr. George D. Spence and Dr. N. Ross Chapman

ABSTRACT

In September 1996, a collaborative marine seismic experiment between the University of Victoria and the Geological Survey of Canada was carried out to investigate the marine gas hydrate layer found on the continental slope off Vancouver Island. The methane hydrate bottom simulating reflector (BSR), which is at the base of the hydrate stability zone, was examined using high resolution short-offset multichannel seismic reflection data. The BSR was studied in two regions: (1) near the top of the continental slope (water depth as shallow as 500 m), where the BSR was expected to approach the seafloor, and (2) in areas of topographic highs where the amplitudes of the BSR were expected to be the highest. The study included: (1) mapping the heat flow from the depth of the BSR, and (2) calculation of the seafloor and BSR reflection coefficients.

Detailed analysis of the seismic data revealed the heat flow patterns of the region, estimated from the depth of the BSR. The average heat flow of the region was found to be between 70 and 80 mW/m². Although there are many second order variations, there is a clear regional trend of heat flow decreasing landward across the continental margin. This regional trend reflects the combined effects of the processes of sedimentation in the Cascadia basin, tectonic sediment thickening in the accretionary prism and subduction of the Juan de Fuca plate. In addition, a consistent pattern of high heat flow over the flanks of topographic highs and low heat flow over the topographic highs themselves was observed. This correlation between heat flow and seafloor topography was attributed mainly to the effects of topography on superficial thermal gradients. No strong evidence of channeled migration of fluids along faults and other hydrologic conduits was observed.

In the second part of the thesis, reflection coefficients of the seafloor and the BSR were examined. No correlation between seafloor reflection coefficients and seafloor topography was detected. However, a certain correlation between the BSR

reflection coefficients and the seafloor topography was observed. High reflection coefficients for the BSR were also observed over a channel between two topographic highs.

Examiners:

[Redacted]

Dr. George D. Spence, Co-supervisor (School of Earth and Ocean Sciences)

[Redacted]

Dr. N. Ross Chapman, Co-supervisor (School of Earth and Ocean Sciences)

[Redacted]

Dr. Roy D. Hyndman, External member, Pacific Geoscience Centre, Geological Survey of Canada, Sidney, B.C. Department of Physics and School of Earth and Ocean Sciences, University of Victoria.

[Redacted]

Dr. Earl E. Davis, External examiner, Pacific Geoscience Centre, Geological Survey of Canada, Sidney, B.C.

TABLE OF CONTENTS

ABSTRACT	ii
TABLE OF CONTENTS.....	v
LIST OF FIGURES.....	vii
LIST OF TABLES	x
ACKNOWLEDGEMENT	xi
CHAPTER ONE	INTRODUCTION
1.1	What are gas hydrates ?1
1.2	Global distribution of hydrates3
1.2.1	Gas hydrates in polar regions 3
1.2.2	Gas hydrates in oceanic regions5
1.3	Importance of gas hydrates6
1.3.1	Gas hydrates as fuel resource6
1.3.2	Gas hydrates as geologic hazards.....7
1.3.3	Role of gas hydrates in global climate change.....9
1.4	Formation of methane hydrates11
1.4.1	In situ formation model14
1.4.2	Fluid expulsion model15
1.4.3	Free gas migration model17
1.5	The Cascadia margin18
1.5.1	Tectonic setting18
1.5.2	Earlier studies of the Cascadia margin20
1.5.3	Gas hydrates of the Cascadia margin23
1.5.4	Thermal regime of the Cascadia margin 26
1.6	Objectives of the present study28

CHAPTER TWO ACQUISITION AND PROCESSING OF SEISMIC DATA

2.1	Overview	30
2.2	Acquisition of multichannel seismic data	31
2.3	Processing of the seismic data	33
	2.3.1 Processing flow chart	33
	2.3.2 Offset dependent ghost	42
2.4	Preliminary observations of seismic sections.....	43

CHAPTER THREE HEAT FLOW VARIATIONS FROM BOTTOM SIMULATING REFLECTORS ON THE CASCADIA MARGIN

3.1	Overview	46
3.2	Methodology of heat flow calculations	47
3.3	Errors in heat flow estimates	52
3.4	Results and discussion	56
3.5	Effect of topography on superficial thermal gradients	63

CHAPTER FOUR STUDY OF THE SEAFLOOR AND BSR REFLECTION COEFFICIENTS

4.1	Overview	69
4.2	Methodology of calculation of reflection coefficients	70
	4.2.1 Picking of amplitudes	72
	4.2.2 Determination of conversion factor	73
4.3	Results and discussion	77

CHAPTER FIVE CONCLUSIONS

BIBLIOGRAPHY	98
--------------------	----

LIST OF FIGURES

Figure 1.1	Unit cell of gas hydrate structure I	1
Figure 1.2	Impedance model of the BSR	2
Figure 1.3	Worldwide gas hydrate occurrence map	4
Figure 1.4	Submarine slides as a result of gas hydrate dissociation	8
Figure 1.5	Pressure-Temperature phase diagram for methane hydrate stability field	13
Figure 1.6	Fluid expulsion model of hydrate BSR formation	16
Figure 1.7	The continental margin in the vicinity of the northern Cascadia margin	19
Figure 1.8	Offshore-onshore structural cross section across southern Vancouver Island margin	21
Figure 2.1	Area of study	31
Figure 2.2	Track chart of multichannel seismic lines	32
Figure 2.3	Pre-stack processing flow chart	33
Figure 2.4	Sample shot gather and amplitude spectrum after frequency filtering	35
Figure 2.5	Sample shot gather and amplitude spectra after predictive deconvolution	38
Figure 2.6	Sample stack section after predictive deconvolution	40
Figure 2.7	Stack section after post stack predictive deconvolution	41
Figure 2.8	Migrated stack section	41
Figure 2.9	Post stack processing flow chart	42
Figure 2.10	Shot gather and amplitude spectra showing the offset dependent ghost reflection	44
Figure 2.11	Migrated stack section showing the presence of BSR at	

	a channel between two topographic highs	45
Figure 3.1	Models of P-wave velocity, density, seafloor temperature and thermal conductivity that were used for heat flow calculations	48
Figure 3.2	Spatial distribution of data points used to compute heat flow	49
Figure 3.3	Contour map showing the heat flow patterns	51
Figure 3.4	Contour map showing variation of heat flow with respect to seafloor topography	51
Figure 3.5	Variation of heat flow with respect to distance from the deformation front	56
Figure 3.6	Heat flow over part of line L-17	58
Figure 3.7	Heat flow over part of line L-19	59
Figure 3.8	Heat flow over part of line L-21	60
Figure 3.9	Heat flow over part of line L-22	61
Figure 3.10	Heat flow over part of line L-27	62
Figure 3.11	Comparison of observed heat flow with those predicted by numerical models	66
Figure 3.12	Alternative explanation for the localized heat flow patterns	67
Figure 4.1	Spatial distribution of amplitude data points	71
Figure 4.2	Seafloor and BSR reflection coefficient calculation Using multiple/primary method	74
Figure 4.3	Computation of conversion factor	76
Figure 4.4	Distribution of seafloor and BSR reflection coefficient values	79
Figure 4.5	Contour maps of seafloor reflection coefficients	81
Figure 4.6	Reflection coefficient profiles over lines L-09,	

	L-10 and L11	83
Figure 4.7	Reflection coefficient profiles over lines L-16, L-17 and L-18	86
Figure 4.8	Reflection coefficient profiles over lines L-21 and L-22	88
Figure 4.9	Contour maps of BSR reflection coefficients	90
Figure 4.10	High BSR reflection coefficients over topographic high	91
Figure 4.9	High BSR reflection coefficients over a channel Between topographic highs	94

LIST OF TABLES

Table 3.1	Heat flow estimates using different velocity models	52
Table 3.2	Heat flow estimates using different density models	53
Table 3.3	Comparison of heat flow values computed using hydrostatic and lithostatic model	54
Table 4.1	Comparison of seafloor reflection coefficients from Seismic and core data	78

ACKNOWLEDGEMENT

I want to extend my thanks to my supervisors, Dr. George D. Spence and Dr. N. Ross Chapman whose constant guidance and encouragement made this work a reality. Dr. Chapman was particularly helpful in the final stages of the work, devoting an appreciable amount of his free time to review the manuscript and suggest a number of useful changes.

I would also like to thank my committee member Dr. Roy D. Hyndman and my external examiner, Dr. Earl E. Davis for their valuable suggestions, comments, helps and revisions to this thesis.

Thanks are due to Dr. Tianson Yuan for his help and advice regarding seismic data processing. I am also grateful to Dr. Rakesh Walia and Mr. Yanpeng Mi for all their help during the various stages of the work. I would also like to take this opportunity to thank the captain and crew of the scientific vessel John P. Tully.

Finally, I would like to thank Mr. Partha Chakraborty, Mr. Anubрати Mukherjee, Ms. Neelam Jolly, Dr. Kamran Behdinan and Mr. Debasish Sasmal for making my stay in Victoria a very memorable one.

CHAPTER 1 INTRODUCTION

1.1 What are gas hydrates ?

Gas hydrates are ice-like solids belonging to the class of clathrate compounds where the gas molecules are trapped within water molecule cages. (Figure 1.1). They

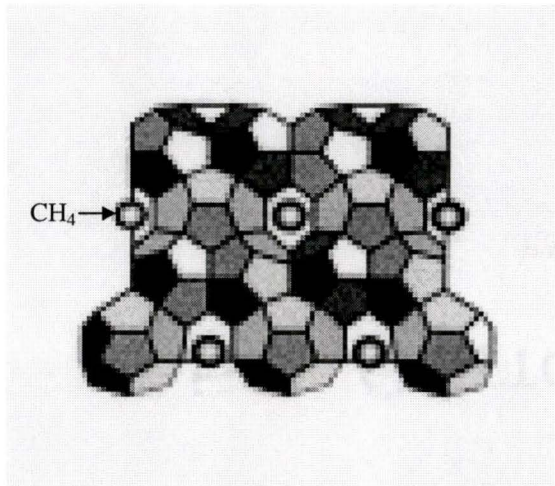


Figure 1.1: gas hydrate structure I. Each methane molecule is effectively trapped by rigid cages of hydrogen-bonded water molecules. Structure is stable when ~90% of cages are filled. From Kvenvolden (1993).

are not true (stoichiometric) chemical compounds. Because of their small size (less than 5.8 Angstrom), methane molecules can fit in the voids of an isometric (Structure I) lattice that contains 46 water molecules per unit cell (Kvenvolden, 1993).

Hydrates were first reported by Davy (1811), who described the formation of a yellow precipitate as a result of chlorine gas bubbled through water. Initially, hydrate studies were purely academic. In the 1930's, it was discovered that hydrates could form from natural gas and effectively block gas flow. Research was aimed at inhibiting the formation of hydrates in natural gas pipelines in the colder regions. In the 1950's and 1960's, shallow gas release during drilling in the Arctic and offshore led to the speculation that there could be natural occurrences of hydrate. It was suggested that they could

represent a fuel resource. This led to the studies aimed at developing hydrate deposits that are economically viable. These studies got a major boost after Soviet scientists reported success at the recovery of natural gas from the hydrate deposits of Siberia (Makogon, 1972).

Seismic evidence of marine gas hydrates was first observed by Markl et al. (1970)

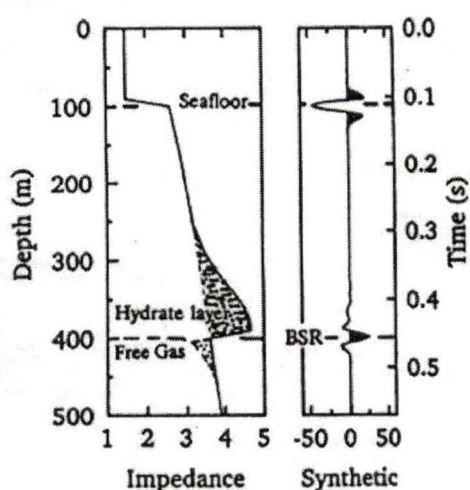


Figure 1.2: Impedance model of the BSR (adapted from Hyndman and Spence, 1992).

over the Blake Outer Ridge off south east United States. Since then, numerous studies have inferred the presence of hydrate most commonly in the continental slope areas over subduction zone accretionary wedges. In the seismic sections of Blake Outer Ridge, an anomalous reflector running parallel to the seafloor, cutting across stratigraphic reflectors, was observed. Because of this characteristic,

the reflector was named the Bottom Simulating Reflector or the BSR. Further studies have confirmed that the BSR occurs close to the base of the hydrate stability zone (Kvenvolden and MacDonald, 1985; Sloan, 1990; Hyndman et al., 1994; Trehu et al., 1995). The main characteristics of the BSR are (Figure 1.2):

- The reflection polarity is consistently reversed with respect to the seafloor indicating, for a simple impedance contrast, a lower seismic impedance below the boundary;
- The reflection amplitudes are large at the frequencies of the multichannel seismic surveys, up to 50% of that of the seafloor. The observed reflection coefficients

require a large impedance contrast, and if the BSR is generated by a layer, the layer must be at least 1/8 wavelength thick i.e. greater than about 7 m (Hyndman and Spence, 1992).

- The BSR reflection is generally a single symmetrical pulse characteristic of a simple interface. Even in some high frequency small air-gun surveys, only a single pulse is usually observed (Fink, 1995; Fink and Spence, 1998).

1.2 Global distribution of hydrates

1.2.1 Gas hydrates in polar regions

The cold surface temperature of the polar regions allows gas hydrates to form at relatively low pressures or shallow depths. Onshore gas hydrates are known to occur at the Messoyakha gas field of western Siberia (Makogon et al., 1972) and it is believed that they also occur in many other permafrost areas of northern Russia, including the Timan-Pechora province, the eastern Siberia craton and the northeastern Siberian and Kamchatka areas (Cherskiy et al., 1985).

Permafrost-associated gas hydrate is also present in the North American Arctic (Kvenvolden and Grantz, 1990). Well log responses indicating the presence of hydrates were obtained in the Mackenzie Delta (Bily and Dick, 1974; Judge, 1982), Sverdrup Basin, Arctic Platform and Arctic Islands (Davidson et al., 1978; Judge, 1982) and on the North Slope of Alaska (Collet et al., 1990). Pressure core samples obtained at the Kuparuk River and the Prudhoe Bay oilfields of the North Slope show strong indications of the presence of hydrates (Kvenvolden and McMenamin, 1980).

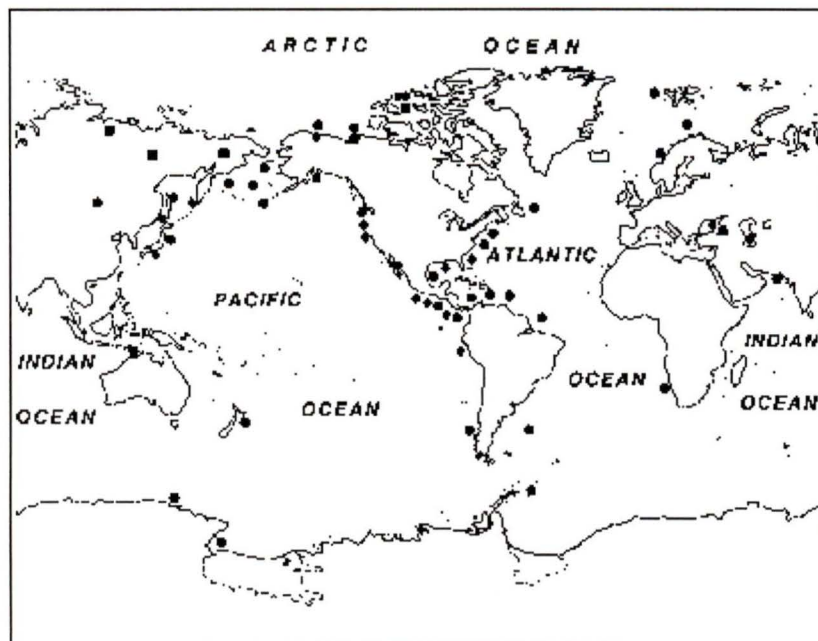


Figure 1.3: Map showing the worldwide locations of known and inferred gas hydrate deposits in continental (permafrost) regions (squares) and in oceanic (aquatic) sediments (circles). Locations where gas hydrate has been recovered are indicated (diamonds). From Kvenvolden, 1994.

In addition to the onshore permafrost regions, gas hydrates are also known to occur within the offshore permafrost areas of the Beaufort Sea shelf of Canada (Neave et al., 1978; Weaver and Stewart, 1982). Offshore gas hydrate is probably present in parts of the vast continental shelf of Siberia (Bell, 1983). The distribution of gas hydrate associated with the offshore permafrost is similar to that of the onshore permafrost.

The information from Arctic gas hydrate studies shows that in polar regions of permafrost, gas hydrates are present at depths of 130 m to 2000 m (Hitchon, 1974; MacDonald, 1983). Gas hydrates may also occur in offshore and onshore permafrost regions of Antarctica but few data are available. Land temperature profiles for

Antarctica suggest that gas hydrates are stable and may be found even at depths of 2000 m (Kvenvolden, 1994).

1.2.2 Gas hydrates in oceanic regions

Various marine geophysical surveys (Markl et al., 1970; Stoll et al., 1971; Tucholke et al., 1977; Shipley et al., 1979) and offshore drilling by the Deep Sea Drilling Project (DSDP) and Ocean Drilling Program (ODP) confirm that gas hydrates are present in almost 10% of the global oceanic area (Kvenvolden, 1994). Their presence is mainly restricted to the rise and slope of continental margins.

A compilation of the global distribution of gas hydrates among the world's oceans was first carried out by Kvenvolden and McMenamin (1980), who showed nine areas where geophysical and geochemical evidence suggest the presence of gas hydrates. Much geophysical evidence was based on the presence of the Bottom Simulating Reflector. By 1982, the number of regions identified which showed presence of hydrates rose to 18 (Kvenvolden, 1982) and by 1983 it reached 23 (Kvenvolden and Bernard, 1983). By combining all the geophysical and geochemical information, a list of 47 locations where gas hydrates can be expected was compiled (Figure 1.3) (Kvenvolden et al., 1993). At 14 of these 47 locations, gas hydrates have been recovered, showing irrefutable evidence for the occurrence of submarine gas hydrates. Deep ocean drilling has recovered hydrates at nine locations. These include offshore Peru, Costa Rica, Guatemala, Mexico, southeastern United States, two locations offshore Japan and the Gulf of Mexico. Shallow sediment coring has also recovered gas hydrates from six locations – Black Sea, Caspian Sea, offshore northern

California, northern Gulf of Mexico and two locations in the Okhotsk Sea (Kvenvolden, 1994).

1.3 Importance of gas hydrates

1.3.1 Gas hydrates as fuel resource

Gas hydrates are exciting prospects as an energy resource of the future. This is mainly for two reasons. Firstly, there is a large amount of methane gas trapped within the hydrate molecules. For example, from a volume of 1 cubic meter of hydrate, the amount of methane available is 164 cubic meters at STP (Sloan, 1990). Thus, the concentration of methane maybe almost 10 times greater than other unconventional sources of natural gas (Kvenvolden, 1988; MacDonald, 1990; Gornitz and Fung, 1994). Secondly, hydrates are distributed widely throughout the world's oceans (Figure 1.3), primarily on the continental slopes.

Though gas hydrates are a major storehouse of methane gas, little progress has been achieved in the extraction and recovery of the gas in a way that is of commercial importance. There are three principal methods for the extraction of gas from hydrates. They are thermal stimulation, depressurization and inhibitor (antifreeze) injection (Holder et al., 1984; Sloan, 1990). All of these three methods try to bring the methane out of the hydrate stability zone into the free gas zone. In thermal stimulation, the temperature of the hydrate stability layer is artificially increased so that the hydrate is no longer stable and it dissociates into methane gas. In case of depressurization, the pressure of the hydrate layer is lowered beyond the stability field. Injection of inhibitors or antifreeze like methanol has been found to prevent the formation of

hydrates of pipelines. Such inhibitors may also be used for the recovery of methane from naturally occurring hydrates.

Development of Messoyakha gas field in Western Siberia during the past 25 years has proven that some methane can be recovered from naturally occurring hydrates (Makogon, 1995; Sloan, 1990). However, the methanol injection method proved to be prohibitively expensive. Recovery of gas hydrates in pressurized core barrels at the Arco-Exxon N.W. Eileen State No. 2 wildcat well on the North Slope of Alaska confirmed the presence of hydrates in the region of Prudhoe Bay and Kuparuk River oilfields (Kvenvolden and McMenamin, 1980), but no effort was made at commercial recovery of gas from the hydrates. Thus, even though methane hydrate could be viewed as a potential fuel resource, the technology to achieve its wide scale recovery are not yet available.

1.3.2 Gas hydrates as geologic hazards

During the formation of hydrates, water and methane molecules become immobilized as a solid, restricting the pore spaces and retarding the migration of fluids. An ice-like solid, in place of liquid water, occupies the pore spaces and the processes of consolidation and mineral sedimentation are inhibited. As more sediments are deposited, the base of the stability zone moves up. Hydrates dissociate to gas below the stability zone - gas that may rise to concentrate hydrate just above the stability zone. Just below the stability zone, the solid gas-water mixture (hydrate) becomes liquid gas-water mixture. The sediment below base of the hydrate is unconsolidated and possibly over-pressured due to the release of the free gas, leading

to a zone of weakness. At these zones of weakness, failures could be easily triggered by gravitational loading or seismic disturbances leading to large submarine landslides (e.g. McIver, 1982).

The same conditions that cause hydrate dissociation at the base of the stability field during continued sedimentation could also be brought about by the lowering of sea level or by an increase in

bottom water temperatures that change the in situ pressure and temperature conditions. In adjusting to these new pressure-temperature conditions, the bottom of the gas hydrate may dissociate producing a less rigid layer. Submarine slope failures can follow, giving rise

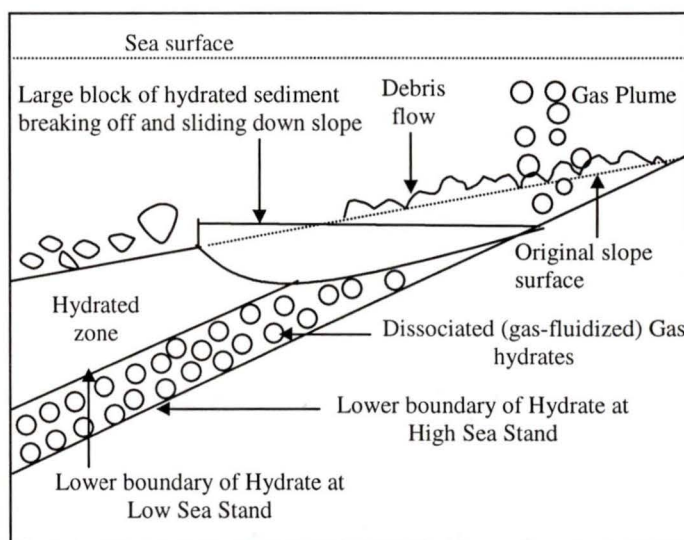


Figure 1.4: Diagram showing the effects of changes in pressure and temperature on submarine gas hydrate and the resulting seafloor failures and gas releases (from Kvenvolden, 1993)

to debris flows, slumps and slides, accompanied by the release of methane gas into the water column. A scenario showing the submarine slope failure is shown in Figure 1.4.

McIver (1977) first recognized the possible connection between gas hydrate boundaries and submarine slides. Possible examples of this phenomenon include surficial slides and slumps on the continental slope and rise of South West Africa (Summerhayes et al., 1979), slumps on the United States Atlantic continental slope (Carpenter, 1981), large submarine slides on the Norwegian continental margin (Jansen et al., 1987; Bugge et al., 1987), sediment blocks on the seafloor in British

Columbia fjords (Bornhold and Prior, 1989) and massive bedding-plane slides and rotation slumps on the Alaskan Beaufort Sea continental margin (Kayen and Lee, 1991). In the Caspian Sea (Ginsburg et al., 1992) and offshore North Panama (Reed et al., 1990), submarine mud volcanoes, another kind of geologic hazard, have also been attributed to the release of gas from hydrates.

1.3.3 Role of gas hydrates in global climate change

Methane is an important trace component of the atmosphere with current total volume of $6.9 \times 10^{12} \text{ m}^3$ (2.4×10^{12} Tcf). According to the Potential Gas Committee (1981), this is approximately half of the methane that occurs in gas hydrate of Arctic permafrost regions. The concentration of methane is increasing at the rate of 1% per year (Watson, et al., 1990) probably as a consequence of leakage in natural gas production and delivery. Because methane is radiatively active, it is a greenhouse gas that has a global warming potential 20 times greater than an equivalent weight of carbon dioxide when integrated over a time span of 100 years (Shine et al., 1990). The amount of methane that is trapped in gas hydrates on and offshore is perhaps 3000 times the amount that is present in the atmosphere (MacDonald, 1990). Thus dissociation of hydrates releasing free methane gas can have a significant effect on the radiative properties of the global atmospheric system and consequently on global warming.

Pleistocene climate changes could have triggered release of free methane gas as explained in the previous section. However, the reverse can also be true, i.e. release of methane gas could have caused a change in global climate (Nisbet, 1990). During

the global warming, the glaciers and ice cap melt, contributing water to the oceans. This rise in sea level causes an increase in subsurface hydrostatic pressure which further stabilizes the submarine gas hydrates on the outer continental margins and on polar continental shelves. At the same time, the rise in onshore air temperatures destabilizes the continental gas hydrate over a time scale of hundreds to thousands of years (Kvenvolden, 1994). A part of the methane that is released as a result of temperature rise, may eventually reach the atmosphere. Water temperature generally increases with global warming, though the change may not be significant at greater ocean depths. Thus for submarine gas hydrates on continental margins at water depths greater than 300 to 500 m, the pressure effects on hydrate stability caused by increasing sea level outweigh the destabilizing effect of any possible increase in bottom water temperature.

This conclusion does not apply to gas hydrates underlying shallow polar continental shelves. Increasing air temperatures increase shallow shelf water temperatures. Of greater importance is the increase of surface temperatures caused by the transgression of the polar ocean as sea level rises over the previously exposed, very cold continental shelf surface. Flooding of the shelf by relatively warm ocean water outweighs the stabilizing effect of the sea level rise. Thus, at polar continental shelves, methane is released from hydrates as a result of global warming. Methane is added to the atmosphere, contributing further to the global warming trend.

During cycles of global cooling, the reverse situation takes place. The water in the oceans thermally contracts, leading to a fall in sea level and regression of the sea from the continental shelves. In addition a significant fall in the sea level occurs as

water is taken up in the ice caps. During this regression, there is a decrease in the hydrostatic pressure over the gas hydrates and the deepest gas hydrates become unstable. At the polar continental shelves, the colder temperature leads to the stabilization of the gas hydrate. So, during global cooling, the addition of methane from hydrates can only be from the submarine deposits. This methane has to travel a long way up through the overlying sediment without reforming as hydrate and up through the water column without being dissolved or oxidized. Thus, it is clear that gas hydrate deposits respond to the changes in global climate variations.

1.4 Formation of methane hydrates

Gas hydrates are formed at conditions of relatively low temperatures and high pressures, and two opposing factors control the distribution of hydrates in the earth. The first is the geothermal gradient or the increase in temperature associated with the increase in sediment or crustal depth. Average gradients in sediments are typically from $50^{\circ}\text{C}/\text{km}$ to $70^{\circ}\text{C}/\text{km}$ and those in the continental crust are from $25^{\circ}\text{C}/\text{km}$ to $35^{\circ}\text{C}/\text{km}$, although the range can vary considerably. As hydrates are stable only at relatively low temperatures, these geothermal gradients limit the occurrence to shallow, cooler regions of the crust.

The second factor that plays an important role in the formation of hydrate is the increase of pressure with increasing sediment and water depths. Hydrates are more stable at higher pressure, which are at greater depths and hence at higher temperatures. Figure 1.5 shows the pressure-temperature stability conditions controlling the formation of hydrates (Hyndman et al., 1994). An increase in temperature or a

decrease in pressure will move the hydrate out of the stability field and cause dissociation of the hydrates. A close look at Figure 1.5 reveals that along the hydrate stability curve, the change in temperature is much more significant than the corresponding change in pressure. Thus, the depth of the overburden above the BSR is more strongly a function of temperature than pressure.

One feature of marine gas hydrates that is not apparent from the phase diagram in Figure 1.5 is the amount of methane that is required for gas hydrate formation. Gas hydrates will form with about 90% of the cages of the clathrates filled (Sloan, 1990). This requirement for a source of enormous amounts of methane for gas hydrate formation limits the regions where significant gas hydrates can be expected and found.

Although thermogenic gas hydrates occur (Brooks et al., 1985; Kvenvolden, 1993), studies of the relatively few DSDP/ODP drillcore, or gravity-cored samples (e.g. Westbrook et al., 1994) indicate that most methane in hydrates are of biogenic (bacterial) origin (MacDonald, 1990). This evidence is based on the isotopic composition of the methane, and the ratio of methane to ethane-plus-propane in both the clathrates and the surrounding pore water. Methane should constitute ~99% of the hydrocarbon gas mixture if the gas is biogenic. The isotopic composition of biogenic methane ($\delta^{13}\text{C}$) is expected to be between ~-5.5‰ and ~-8.5‰, compared to the composition of thermogenic methane, which lies between ~-2.5‰ and ~-6.0‰ (Sloan, 1990). The decomposition of fermentable organic matter in the anaerobic environment of marine sediments (i.e. commonly below about 10 m of sediment) yields methane as the primary product. The temperature range for biogenic methane production is broad, estimated at between 4°C and 55°C with an optimum between 35°C and 42°C

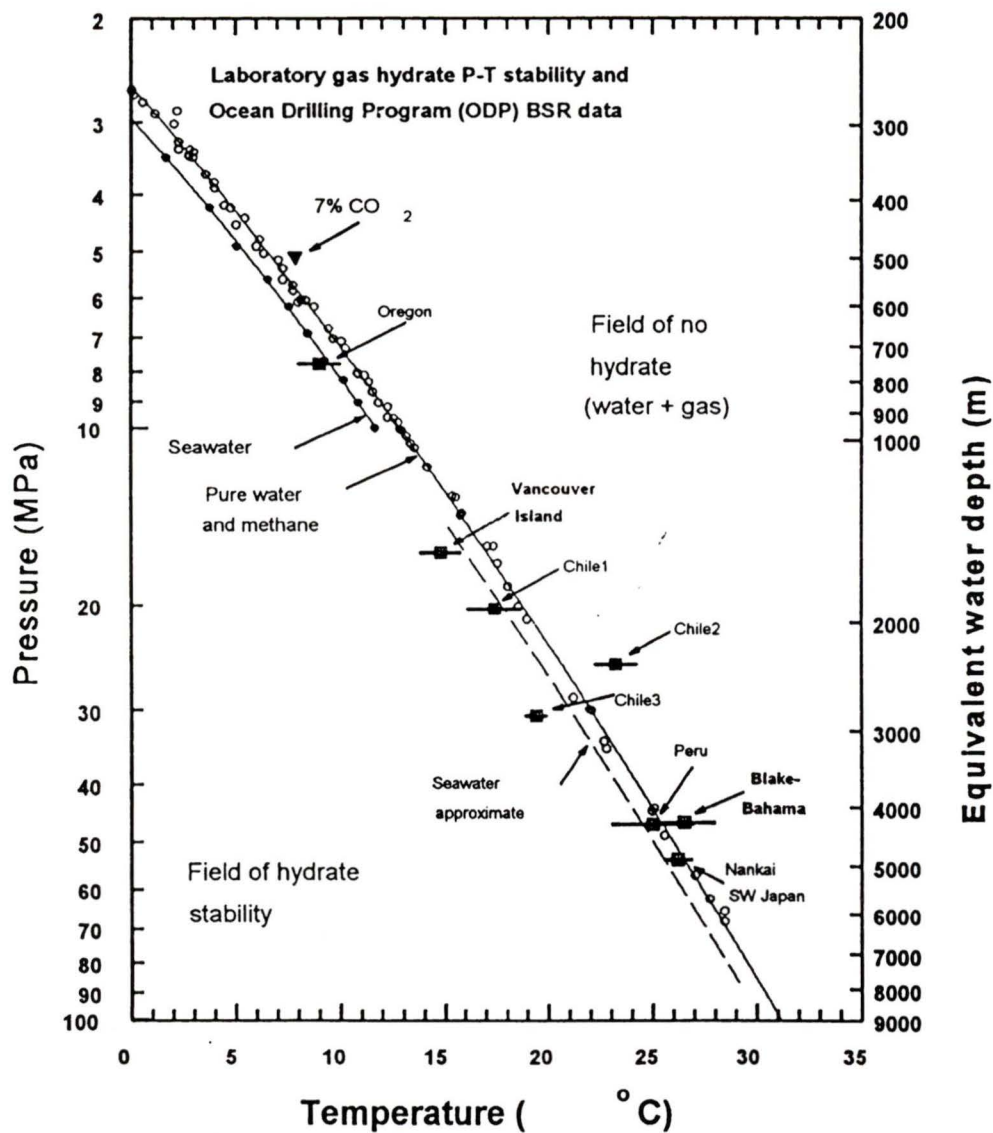


Figure 1.5: The pressure temperature phase diagram for methane hydrate stability field. The solid line seawater curve is from the equation-of-state computation for artificial seawater by Englezos and Bishnoi (1988) and Dickens and Quinby-Hunt (1994). Extensive laboratory data for pure water/methane and limited data on the influence of CO₂ are also illustrated. Estimates of in situ P-T conditions at the base of hydrate stability field measured at DSDP/ODP sites agree well with the laboratory data (from Hyndman, et al., 1994).

MacDonald, 1990). A detailed description of biogenic methane production is given in Makogan (1974). Makogan predicts that, in order for clathrate hydrates to form, the methane concentration must exceed the solubility of methane in pore water. However, the necessity of methane over-saturation prior to hydration has been challenged by Hyndman and Davis (1992), and the issue is currently unresolved.

Three different models have been proposed for the formation of naturally occurring hydrates. Broadly speaking, in order for gas hydrates to form within deep-sea sediments, two conditions must be met:

1. The temperature and pressure requirements must be satisfied;
2. There must be sufficient amount of natural gas to form hydrates. Large amounts of natural gas are either produced locally or a mechanism for the concentration of the gas above the BSR must occur.

1.4.1 In situ formation

In the first model, Paull et al. (1994) postulated the sequence of events that is necessary for in situ production of gas hydrates:

1. Microbial sulphate reduction reduces the amount of sulphate dissolved in pore fluids;
2. Biogenic methane production occurs at the base of the sulphate reduction zone;
3. Once saturation is reached, any amount of additional methane generation results in either gas hydrate or free gas, depending on the pressure and temperature conditions.

According to this model, the amount of methane that can be produced in a closed system (i.e. no gas migration) is controlled by the amount of metabolizable organic carbon. However, this model does not address the following questions:

1. Neither the original amount nor the quality of organic carbon can actually be determined for buried sediment;
2. Large quantities of methane required for significant hydrate formation may not be produced locally from the common concentration of organic carbon in a closed system;
3. Free gas over a large depth range below the hydrate stability zone, with concentration equal to that in the hydrate above the stability zone, is generally not detected seismically or measured in drill holes. An exception is on the Blake Outer Ridge where the free gas layer is greater than 200 m thick, and the amount of methane stored in the gas phase is comparable to that stored in hydrate;
4. Hydrates and corresponding BSR's are not seen in normal marine sediment settings where methane production is expected but no mechanism of upward methane concentration or migration occurs.

1.4.2 Fluid expulsion model

The second formation model, the fluid expulsion model proposed by Hyndman and Davis (1992), involves methane migration into the hydrate stability zone by upward fluid flow from greater depths (Figure 1.6). In this model, most of the methane is generated biogenically below the level of hydrate stability field and carried by

upward fluid expulsion, which is a result of tectonic thickening and sediment loading. As the methane-rich but perhaps unsaturated fluids pass into the hydrate stability field, much of the hydrate is removed. The hydrate zone builds upward from the base of the stability field, thus forming a sharp base and a transitional top. This model explains the source of the large quantities of methane required to form the observed hydrate. Free gas below the stability zone is neither required nor excluded in this model. The most unconstrained aspect of the model is the efficiency with which methane is removed and hydrate formed as pore fluids pass into the hydrate stability field. Figure 1.6 illustrates the methane production and hydrate formation processes in an accretionary prism where upward fluid expulsion carries dissolved methane into the stability field. In the normal depositional regime seaward of the deformation front, there is no upward fluid flow into the stability field (Hyndman and Davis, 1992). The

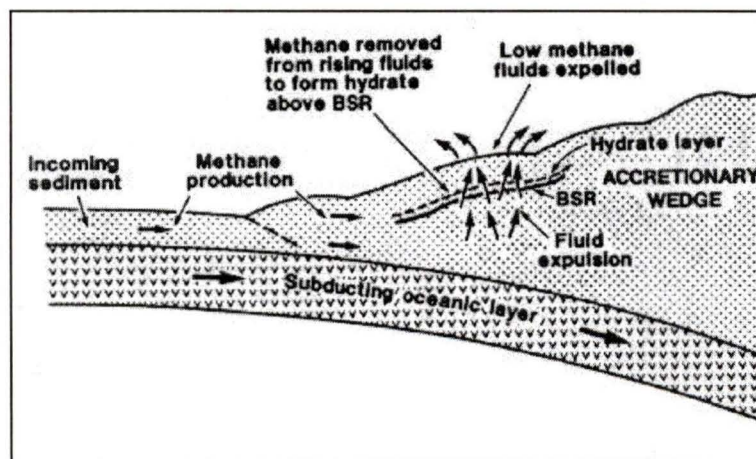


Figure 1.6: Illustration of fluid expulsion model of hydrate BSR formation through methane removal from rising fluids that are tectonically expelled from an accretionary prism (modified from Hyndman and Davis, 1992).

maximum fluid expulsion probably takes place near the deformation front, and the methane hydrate formation and BSR is expected to occur in an area just landward of the deformation front.

1.4.3 Free gas migration model

The third model, proposed by Minshull et al. (1994), suggests that the mechanism of formation is by upward migration of free methane gas bubbles. It was argued that this mechanism is consistent with gas concentration sometimes over structural highs, seen on multichannel seismic data collected offshore Columbia. If gas bubbles are permitted to travel some distance into the hydrate stability field before becoming incorporated in hydrate, the problem of a self-sealing hydrate layer is avoided. Once hydrate crystals have been formed some distance above the base of the stability zone, the hydrate may then build downward as more free gas migrates up. Indirect evidence that free gas migration through the stability field does occur at least locally comes from hydrates collected in piston cores at water depths of 530-560 m in the Gulf of Mexico (Brooks et al., 1984). BSR depths and hydrothermal gradient estimates suggest that the base of the stability field in this region is 570 m below the seafloor, and thus the methane must have traveled a distance of this order before being incorporated in hydrates.

1.5 The Cascadia margin

1.5.1 Tectonic setting

A summary of the regional geophysics and structural framework of the Vancouver Island accretionary prism has been given by Hyndman et al. (1994). Much of the continental margin of the western North America lies along the right-lateral transform fault boundary between the Pacific and North American plates. The San Andreas fault system extends from the Gulf of California to Cape Mendocino in northern California, and the Queen Charlotte fault system extends from just north of Vancouver Island to the Aleutian Trench of Alaska (Figure 1.7). Along the intervening margin of Northern California, Oregon, Washington and southern British Columbia, subduction of the Juan de Fuca plate takes place at the Cascadia subduction zone. The Juan de Fuca plate is a remnant of the larger Farallon plate that has been fragmented as a result of the convergence of East Pacific spreading centre and the North American continent, and the northern movement of the southern Mendocino triple junction (Atwater, 1970). The northern triple junction appears to have been stable off northern Vancouver Island since the Eocene (Riddihough, 1984; Stock and Molnar, 1988; Engebretson et al., 1984; Engebretson et al., 1985; Atwater, 1989).

The modern Juan de Fuca Plate margin exhibits most of the common characteristics of a subduction zone. These include:

1. A series of active volcanoes extending from northern California to southern British Columbia (Wells et al., 1984);
2. Extensive seismicity (Crosson and Owens, 1987; Rogers, 1983);

3. The characteristic pattern of low heat flow in the fore-arc inland from the margin, with an abrupt increase just seaward of the volcanic arc (Lewis et al., 1988; Lewis et al., 1991; Blackwell, 1991, Hyndman et al., 1993);
4. The characteristic low gravity couple represented by low values over the outer margin (trench) and high values at the continental edge (Riddihough, 1979);
5. An extensive accretionary prism (Davis and Hyndman, 1989);

The northern Cascadia accretionary prism is bounded at its base by the underthrusting oceanic crust and on its landward side by the landward dipping

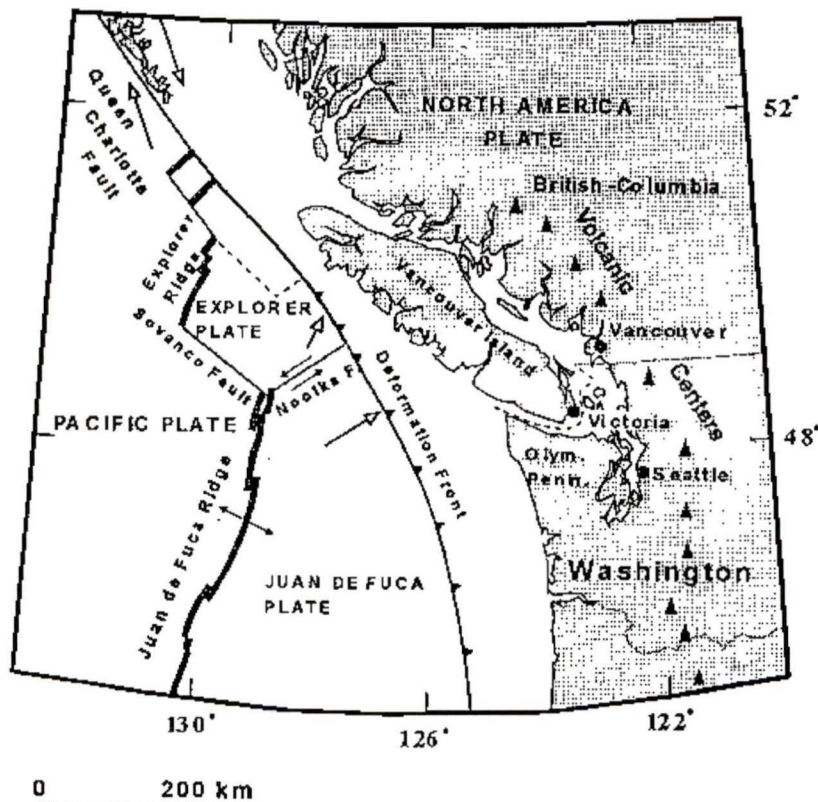


Figure 1.7: The continental margin in the vicinity of the northern Cascadia subduction zone, showing the plate-tectonic regime and major tectonic elements. The spreading ridge segments are shown with heavy lines, and the boundary between the oceanic plates and the boundary between the oceanic plates and the continental plates is shown with fault line (from Yuan, 1996).

Crescent Terrane (Figure 1.8). The Tofino fore-arc basin overlies the prism. The incoming Juan de Fuca plate surface and underthrusting oceanic crust are exceptionally smooth with very few seamounts. Off southern Vancouver Island, the dip of the oceanic crust increases from 3° to 4° just seaward of the deformation front to 10° under the edge of the shelf and then to 15° beneath the coast.

The frontal portion of the accretionary prism has been well surveyed and imaged by multichannel seismic reflection, acoustic imagery and swath bathymetry, revealing its surface morphology, cross sectional geometry and deformation style (Davis and Seeman, 1981; Spence et al., 1991a; Spence et al., 1991b; Davis et al., 1986). No significant bathymetric trench is present adjacent to the Cascadia accretionary prism. The oceanic crust dips gently landward towards the deformation front, with a corresponding thickening of the incoming sediment section. At the deformation front, sediments of the Cascadia Basin are folded and faulted into elongated, anticlinal ridges that stand as much as 700 m above the seafloor. These anticlinal ridges are usually 20-30 km long and often asymmetric with their steep sides facing seaward. The anticlines are developed over a thrust ramp which extends down to near the top of the oceanic crust, indicating that the present decollement is near the base of the sediment section and that most of the sediments are scraped off the subducting oceanic plate at the deformation front (Davis and Hyndman, 1989).

1.5.2 Earlier studies of the Cascadia margin

In the 1960's, Shell Canada Ltd. carried out an extensive exploration program in the Tofino Basin on the Vancouver Island continental shelf. The investigations

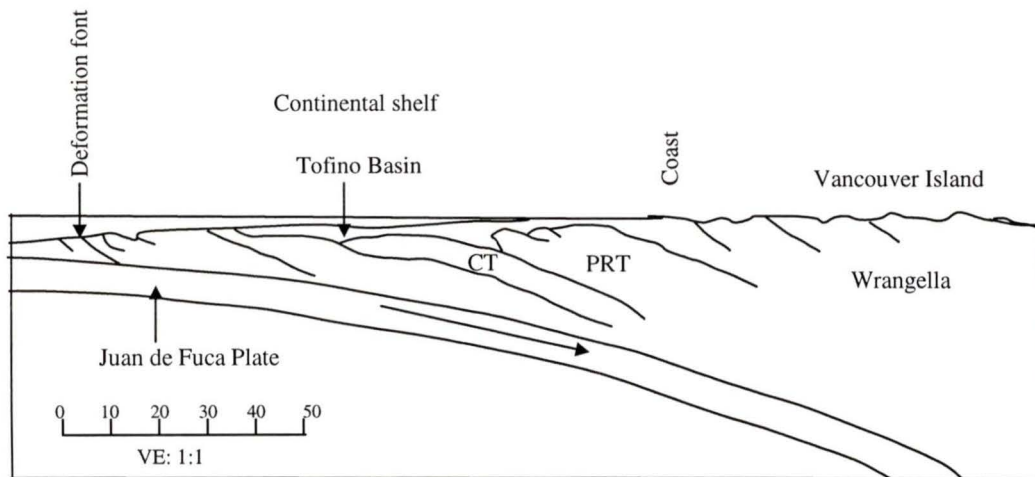


Figure 1.8: Offshore-onshore structural cross-section across southern Vancouver Island margin, showing increase in subducting slab dip angle landward (from Hyndman et al., 1990). Note: CT-Crescent Terrane and PT-Pacific Rim Terrane

included limited resolution seismic surveys and drilling of 7 exploratory wells (Shouldice, 1971). In 1980, a 350 km long offshore-onshore refraction profile perpendicular to the continental margin was recorded to determine the crustal structure from the oceanic Juan de Fuca plate to the inland volcanic arc (Spence et al., 1985; Waldron et al., 1990). In 1984, Phase I of the Canadian LITHOPROBE program, a multidisciplinary geoscience program, carried out detailed investigations at the Cascadia margin. High quality vibroseis multichannel seismic reflection data were collected on Vancouver Island (Yorath et al., 1985; Green et al., 1986; Clowes et al., 1987a; Clowes et al., 1987b). In 1985, a multichannel marine seismic survey with widely spaced lines was carried out across the continental shelf and slope of the northern Cascadia margin as part of the Frontier Geoscience Program of Geological Survey of Canada (Yorath et al., 1987; Davis and Hyndman, 1989; Davis et al., 1990).

Hyndman et al. (1990) presented a summary of the onshore and offshore geophysical work done on the region, which included multichannel seismic reflection, shallow single channel seismic reflection, gravity and magnetic data, seismicity, geothermal and magneto-telluric studies.

In 1989, as a part of site surveys preliminary to the Ocean Drilling Program Leg 146, new marine multichannel seismic data were acquired across the northern Cascadia convergent margin and the adjacent Juan de Fuca ridge (Spence et al., 1991a; Spence et al., 1991b). In addition to the marine seismic lines, wide angle seismic data were acquired at land sites to obtain deep velocity information (Wang and Clowes, 1995). The survey provided information on the detailed three dimensional geometry of the accretionary wedge and the accreted terranes. The data also revealed the variation in the thrust and fold structure at the deformation front and the characteristics of the gas hydrate BSR (Hyndman et al., 1994; Yuan et al., 1994; Yuan et al., 1996). In 1992 ODP Leg 146 penetrated the accretionary wedge sediments to investigate the relationship between fluid expulsion and tectonics in the development of the subduction zone accretionary prism as well as the nature of the widely distributed BSR (Westbrook et al., 1994; Carson et al., 1995). At all sites of the Cascadia margin and the Oregon margin, detailed measurements were made of the in situ physical and chemical conditions. Sonic log and Vertical Seismic Profile (VSP) studies were also carried out to provide information about the formation velocity (MacKay et al., 1994).

In 1993, another seismic program was carried out near ODP Leg 146 Hole 889/890. Wide angle seismic data were collected on ocean bottom seismometers and single channel seismic reflection data were recorded over closely spaced grid of lines

(Fink, 1995; Fink and Spence, 1998; Hobro, 1998). This investigation led to an understanding of the detailed areal distribution of the hydrate BSR. A two ship expanding spread profile survey near the ODP drill site was also carried out in 1993 by the Defence Research Establishment Pacific (DREP) to examine the seafloor reflection character and to constrain the seismic velocity structure of the hydrate zone (Hannay, 1995).

The wealth of geophysical and geological information has made the Cascadia margin one of the most thoroughly studied subduction regions of the world. During the last twenty years, the knowledge of the Cascadia margin has evolved from the mere acknowledgement of the subduction process to a more comprehensive understanding of its tectonic, geological and geophysical processes.

1.5.3 Gas hydrates of the Cascadia margin

The gas hydrates at the Cascadia margin have been extensively studied on the basis of multichannel seismic reflection data (Hyndman and Spence, 1992; Spence et al., 1995, Yuan et al., 1996, Yuan et al., 1998), single channel seismic reflection data (Fink, 1995; Fink and Spence, 1998), borehole data providing calibration for the seismic interpretation, and Vertical Seismic Profiles (VSP) (MacKay et al., 1994). The BSR is visible over much of the continental slope, from the lower slope 10–20 km landward of the deformation front to the upper slope where the water depth is about 800 m (Hyndman et al., 1994; Spence et al., 1995). Hydrate is not stable at shallower water depths because of higher seafloor temperatures and lower pressures.

From multichannel seismic data near the ODP sites 889/890 on the lower slope of the Cascadia margin off Vancouver Island, Hyndman and Spence (1992) concluded that a high velocity layer existed above the BSR, having a sharp base and transitional top. Their conclusions were based on velocity analyses, synthetic seismogram modeling and AVO studies. No free gas below the BSR was interpreted from the velocity and AVO analyses. Hyndman and Spence (1992) concluded: (1) that the hydrate is concentrated in a layer at the base of the stability field, just above the BSR; (2) that 30% of pore spaces were required to be filled with hydrate if BSR contrast was due to only high velocity sediments; and (3) that if there is free gas beneath the BSR, it is of low concentration (less than several percent) or very thin (less than a few meters) such as not to be seismically resolvable.

Subsequent downhole logging and VSP data at ODP sites 889 and 892 indicated low velocity immediately below the BSR, implying the presence of free gas (Mackay et al., 1994). The study concluded that there is only a small velocity enhancement due to hydrates above the BSR and that the BSR is generated primarily from the top of the free gas layer. Singh and Minshull (1994), from full waveform inversion of the multichannel seismic data of Hyndman and Davis (1992), reached similar conclusions. However, it should be noted, that in these velocity estimates, there had been little direct constraint on the normal no-hydrate/no-gas velocity depth profile and hence there was little constraint whether the BSR contrast is from high velocity/normal interface or normal/low velocity interface. In order to make a proper estimate of the concentration of hydrates from the velocities of the BSR, one should have a reference velocity-depth profile of a sediment unaffected by either high

velocity hydrate or low velocity free gas. Full waveform inversion results, including good estimate of the reference velocity profile, indicated that the velocity contrast at the BSR was more due to high velocity hydrates than to low velocity gas (Yuan et al., 1998).

From the large offset multichannel seismic reflection data across the Vancouver Island subduction zone margin, Yuan et al. (1994) concluded that sediment velocities in the Cascadia Basin sediments increase towards the deformation front of the accretionary wedge. Their results indicated an initial over consolidation and a surprisingly high rate of pore fluid expulsion ($0.0012 \text{ m}^3 \text{ m}^{-2} \text{ a}^{-1}$). Where frontal thrusts are present along the deformation front, velocities increase landward toward each thrust. Farther landward in the main accretionary zone, where the wedge thickens rapidly and sediments within the wedge are strongly deformed, much lower velocities were observed compared with the basin sediments at the same depths. The lower velocities indicated much higher porosities at given depths and thus underconsolidation with respect to the Cascadia Basin section. Sediment thickening by overthrusting, folding and internal deformation increases the overburden stress in the wedge faster than the sediments can respond by fluid expulsion. Increased fluid pressures must result and substantial porosity loss and fluid expulsion are delayed to 15-20 km farther inland. The sediments continue to lose pore fluids and exhibit pervasive fluid flow as they are incorporated into the accretionary wedge.

From an integrated analysis of multichannel seismic reflection data, ODP downhole data and VSP velocity-depth profile, Yuan et al. (1996) determined a semi-quantitative estimate of the hydrate concentration. The semblance velocities

determined in this study give the only estimate yet available for the reference velocity profile, i.e. for no-hydrate/no-gas. The estimated hydrate concentration-depth profiles indicate a total concentration of $800 \text{ m}^3/\text{m}^2$ at STP. The total methane gas is estimated to be about 200 Tcf in an area of $20 \times 300 \text{ km}$ where clear BSR has been observed in the Vancouver Island continental margin.

1.5.4 Thermal regime of the Cascadia accretionary prism

A regional compilation of the early heat flow data in the Juan de Fuca region was prepared by Hyndman (1983). Davis et al. (1990) reported detailed heat probe results across the Vancouver Island deformation front and lower continental slope. In the Davis et al. (1990) study, heat-flow probe measurements were collected along two transects where a layer of soft sediments permitted penetration of the probe. Initial heat flow measurements were also made from the depth of gas hydrate BSR.

From these results, Davis et al. (1990) recognized a general trend with heat flow decreasing landwards across the continental margin from an average of $120 \text{ mW}/\text{m}^2$ in the Cascadia margin, to about $90 \text{ mW}/\text{m}^2$ over the lower continental slope, to about $50 \text{ mW}/\text{m}^2$ at the continental shelf. The basin values are in agreement with the values predicted for 6 Ma old oceanic crust (Parsons and Sclater, 1977), after accounting for the effects of sedimentation. The landward decrease in heat flow is due to the combined process of subduction of the oceanic plate and the thickening of sediments at the accretionary wedge (Hyndman and Wang, 1993; Hyndman et al., 1994).

Davis et al. (1990) also used the heat flow data to constrain the nature of pore fluid expulsion from the accretionary prism. The lack of strong local anomalies suggested that only minor channelized migration of pore fluid occur along faults and other hydrologic conduits. Most of the pore fluid from the consolidated accretionary prism must be expelled pervasively. On the lower slope, a consistent discrepancy was observed between the heat probe data and the estimates from gas hydrate BSR – the former being almost 30% higher. Initially, this discrepancy was attributed to advective heat transport from distributed vertical pore fluid flow. However, later quantitative modeling shows that this effect is too small given reasonable fluid flow velocities (Wang et al., 1993) and the discrepancy remains unexplained.

From a more detailed study of the variations in BSR depth, Hyndman et al. (1993) obtained a broad distribution of the heat flow patterns along all of the available multichannel seismic lines. The heat flow across the seaward portion of the northern Cascadia margin was found to be 20% lower than that predicted by a regional model without sediment thickening and fluid expulsion (Hyndman and Wang, 1993, Wang et al., 1993). It was inferred that the heat flow is reduced as a consequence of horizontal shortening and thickening of the sediment section that vertically stretches the isotherms faster than thermal re-equilibration can occur. The recovery of heat flow farther landward in the prism was explained by the effect of upward advection of heat associated with fluid expulsion. These conclusions were substantiated by variations in porosity-depth across the prism determined from multichannel seismic velocity data (Yuan et al., 1994).

1.6 Objective of the present study

A primary objective of the present study is to obtain an understanding of the thermal regime of the Cascadia margin based on the variation of the BSR depth from multichannel seismic reflection data. On a regional scale, the thermal structure is important for the diagenetic and metamorphic development of accretionary prisms, for hydrocarbon maturation, and for the depth extent of major subduction thrust earthquakes. Local variations of heat flow values can lead to an understanding of the nature of fluid flow in the accretionary wedge, whether it is pervasive or channeled along faults. In accretionary prisms, fluid rock interactions occur in the most dynamic structural environments on Earth; this dynamism acts on sediments undergoing consolidation and burial, resulting in a complex history of structural and fluid processes. As accretionary prisms are nascent orogenic belts, the chemical and physical influence of the fluid flow is necessary for the proper understanding of the evolution of mountain belts. In addition, fluid flow estimates are important for determining the fluid budgets in the accretionary wedge, along with the budget for dissolved elements like carbon which are a part of a larger global cycle.

In the second part of the thesis, the character of the seafloor and the methane hydrate BSR was studied by examining the reflection coefficients from multichannel seismic data. Reflection coefficient values for the BSR can be used as a measure of hydrate saturation (Fink, 1995; Fink and Spence, 1998). Thus, the reflection coefficient values are expected to give an understanding as to where the highest hydrate concentrations may occur for future resource exploration and the association

with geological structures. This also may provide an insight into the formation mechanisms of the hydrates.

In the next chapter, the acquisition and processing of the multichannel seismic data are described. Chapter 3 investigates the heat flow patterns across the Cascadia margin from seismic observations of the BSR. In chapter 4, the character of the seafloor and the BSR and their correlation with topography, are studied by analyzing the reflection coefficients. The conclusions of the study are summarized in chapter 5.

CHAPTER 2 ACQUISITION AND PROCESSING OF SEISMIC DATA

2.1 Overview

In September 1996, a collaborative seismic reflection experiment between the University of Victoria and the Geological Survey of Canada was carried out. The project focussed on the marine gas hydrate layer found on the continental slope off Vancouver Island. The bottom simulating reflector (BSR) at the base of the hydrate stability layer was examined using high resolution multichannel seismic data. A primary objective of the project was to obtain high resolution images of the reflectors associated with the gas hydrate layer in two regions: (1) near the top of the continental slope (water depth as shallow as 500 m) where the base of the hydrate stability field is expected to approach the seafloor, and (2) in areas of local topographic highs, where the amplitudes of the BSR are expected to be the highest (Fink, 1995). The topographic highs may identify regions of recent uplift, and near the top of the slope such uplift may shift the hydrate layer near the seafloor to shallower depths where it is no longer stable and is prone to dissociation.

A second primary objective of the survey (Mi, 1998) was to sample sediments at the seafloor with a piston core in a variety of regions covering a range of expected values of vertical methane flux. Geochemical analyses included measurements of pore water sulphate profiles, which may indicate methane flux toward the seafloor from the

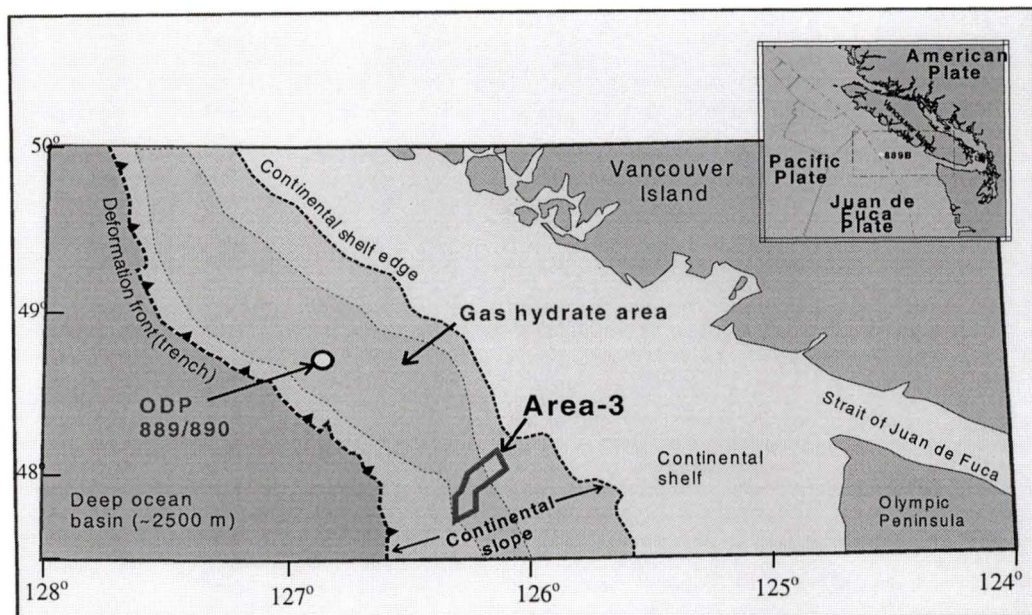


Figure 2.1: Northern Cascadia margin offshore Vancouver Island. The polygon (Area-3) indicates the area of detailed seismic survey. The location of Ocean Drilling Program site 889/890 is indicated by a solid circle. The area of gas hydrate BSR is also shown.

underlying gas hydrate (Borowski, 1996). Cores were also collected near areas where very strong seafloor reflectivity was previously interpreted as evidence for carbonate pavement just at or below the seafloor.

2.2 Acquisition of multichannel seismic data

The region of investigation lies approximately 100 km west of the Vancouver Island (Figure 2.1). The area of study (Area-3) is one of four sub-regions in the seismic survey. A total of 35 lines, with lengths varying from 4 to 12 km, were shot in this sub-region, along a direction parallel to multichannel seismic (MCS) line 89-03 (Figure 2.2). The source for the Area-3 portion of the survey was a 120 cubic inch Bolt 1500C airgun (dominant frequency of 75 Hz). The estimated shot depth was 4 m. The receiver was a 24 channel ITC streamer with a group interval of 8 m. Each group

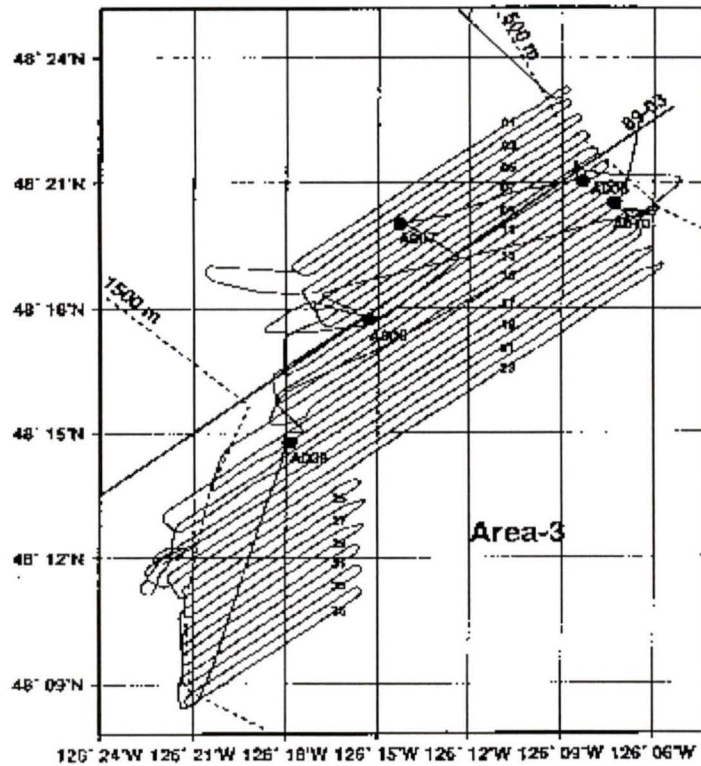


Figure 2.2: Track chart of the multichannel seismic lines. A total of 35 lines, with lengths varying from 4 to 12 km, were shot using a 120 cubic inch Bolt 1500C airgun

contained 3 hydrophones separated by 1.5 m. The centre of the first group was offset from the stern of the ship by 106 m, and the centre of the last group was at a maximum offset of 290 m. Nominal streamer depth was 4 m, but later analyses showed that the receiver depth varied significantly from group-to-group and from shot-to-shot. The data was recorded in SEG-2 multiplexed format using a Strataview recording instrument with a sampling interval of 2 ms.

2.3 Processing of the seismic data

2.3.1 Processing flowchart

The processing of the seismic data was done using INSIGHT/ITA (version 5.1.1) processing software. The prestack processing steps are summarized in Figure 2.3. The first step was to convert data from the multiplexed (SEG-2) format to de-

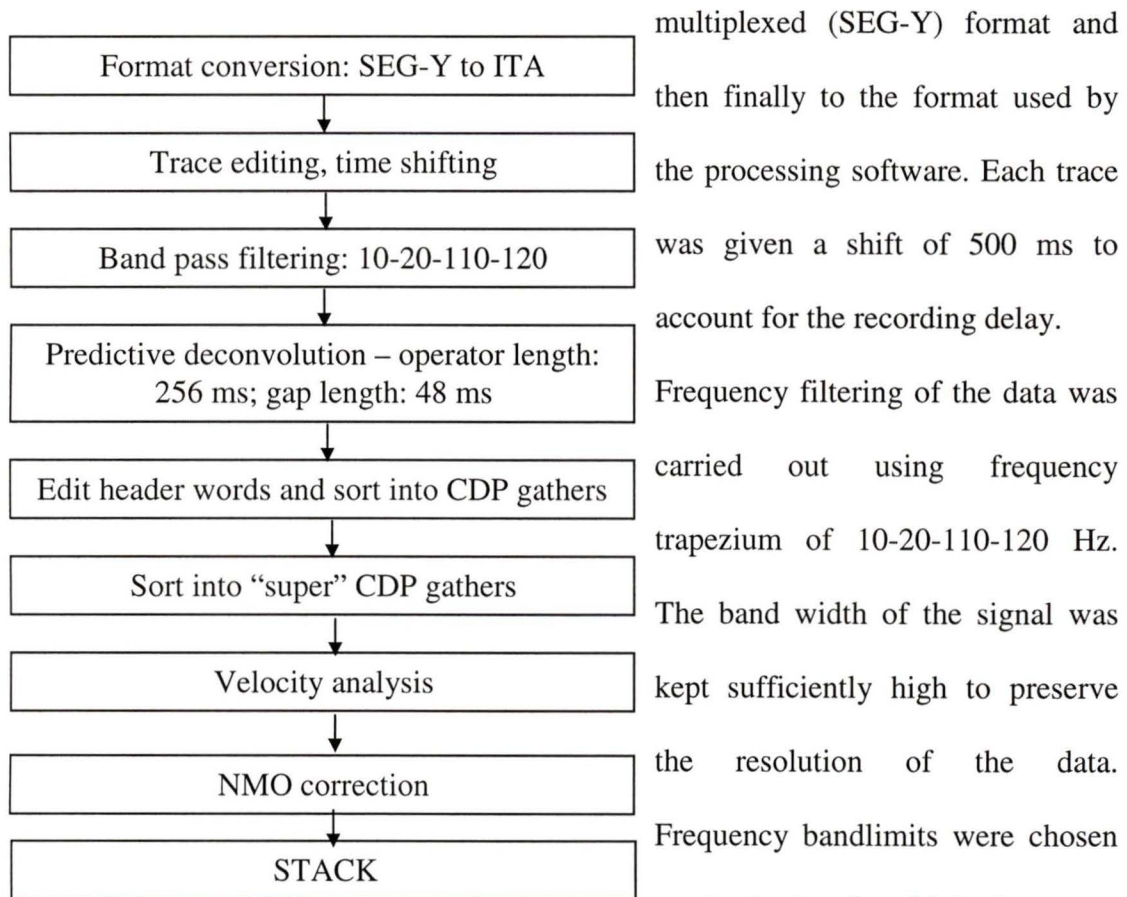


Figure 2.3: pre-stack processing flow chart

many frequency spectra (Figure 2.4).

The next step in the processing sequence was predictive deconvolution. The objective of this filter was to remove the bubble pulse found at about 100 ms after the primary pulse. Deconvolution was carried out using a number of values of operator

multiplexed (SEG-Y) format and then finally to the format used by the processing software. Each trace was given a shift of 500 ms to account for the recording delay.

Frequency filtering of the data was carried out using frequency trapezium of 10-20-110-120 Hz. The band width of the signal was kept sufficiently high to preserve the resolution of the data. Frequency bandlimits were chosen on the basis of multiple frequency panels and close examination of

length and prediction lag. The filter with operator length of 256 ms and a prediction lag of 48 ms was found to be most effective at removing the bubble pulse (Figure 2.5).

The shot gathers were then sorted into common midpoint (CMP) gathers. As the group interval of the data was extremely short (8 m) compared with the shot interval (24 m), the resulting subsurface foldage was only four. This led to difficulty in picking the velocities required for normal moveout (NMO) correction. To overcome this problem, six consecutive CMP's were combined to yield a "super" CMP gather which contained 24 traces in each gather. Semblance based velocity analyses were carried out. The determination of NMO velocities from this "super" CMP gathers becomes considerably easier since the continuity of the events could be more easily identified from a gather of 24 traces. However, due to the short source-receiver offset, the velocities determined may not be very accurate. The "super" CMP gathers were then corrected for normal moveout and stacked.

On the stack section (Figure 2.6), pre-stack predictive deconvolution was not completely successful in removing the bubble pulse. This might be due to the variation of the predictive nature of the bubble with respect to the source-receiver offset. Hence, post-stack predictive deconvolution, with operator length of 128 ms and prediction length of 16 ms, was applied to the stack section and thus was successful in reducing the amplitude of the bubble pulse. (Figure 2.7). The stack section was migrated (Figure 2.8) with a phase shift migration scheme (Amestoy, 1987), in which a seawater velocity of 1470 m/s and sediment velocity of 1550 m/s were used as input parameters. Frequency filtering (frequency trapezium of 10-20-110-120 Hz) was done

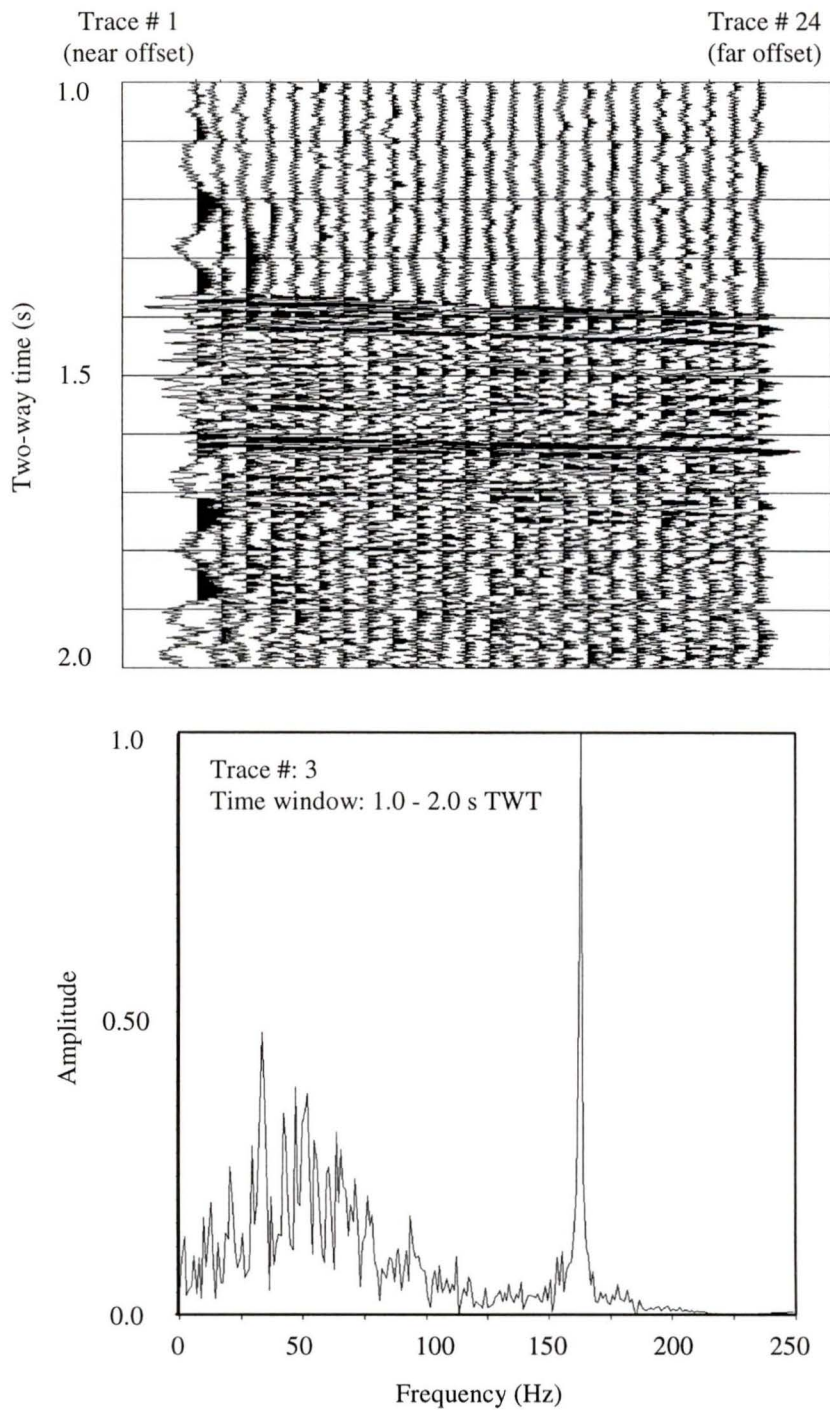


Figure 2.4(a): A sample shot gather and amplitude spectrum of the raw seismic data. There is a high frequency noise at around 160 Hz.

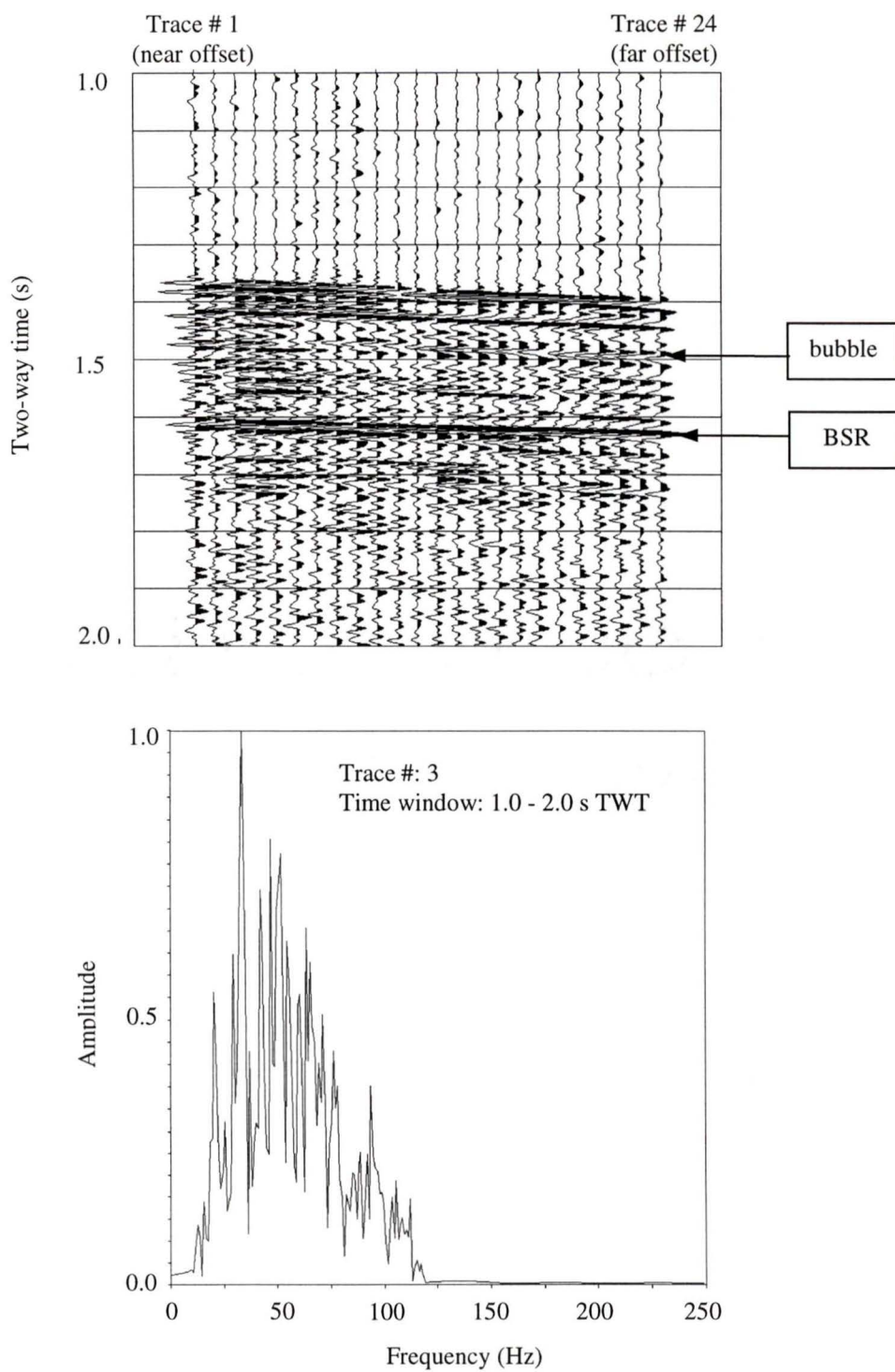


Figure 2.4(b): Shot gather of and amplitude spectrum of 2.4(a) after bandpass frequency filtering. The frequency trapezium of the filter was 10-20-110-120 Hz.

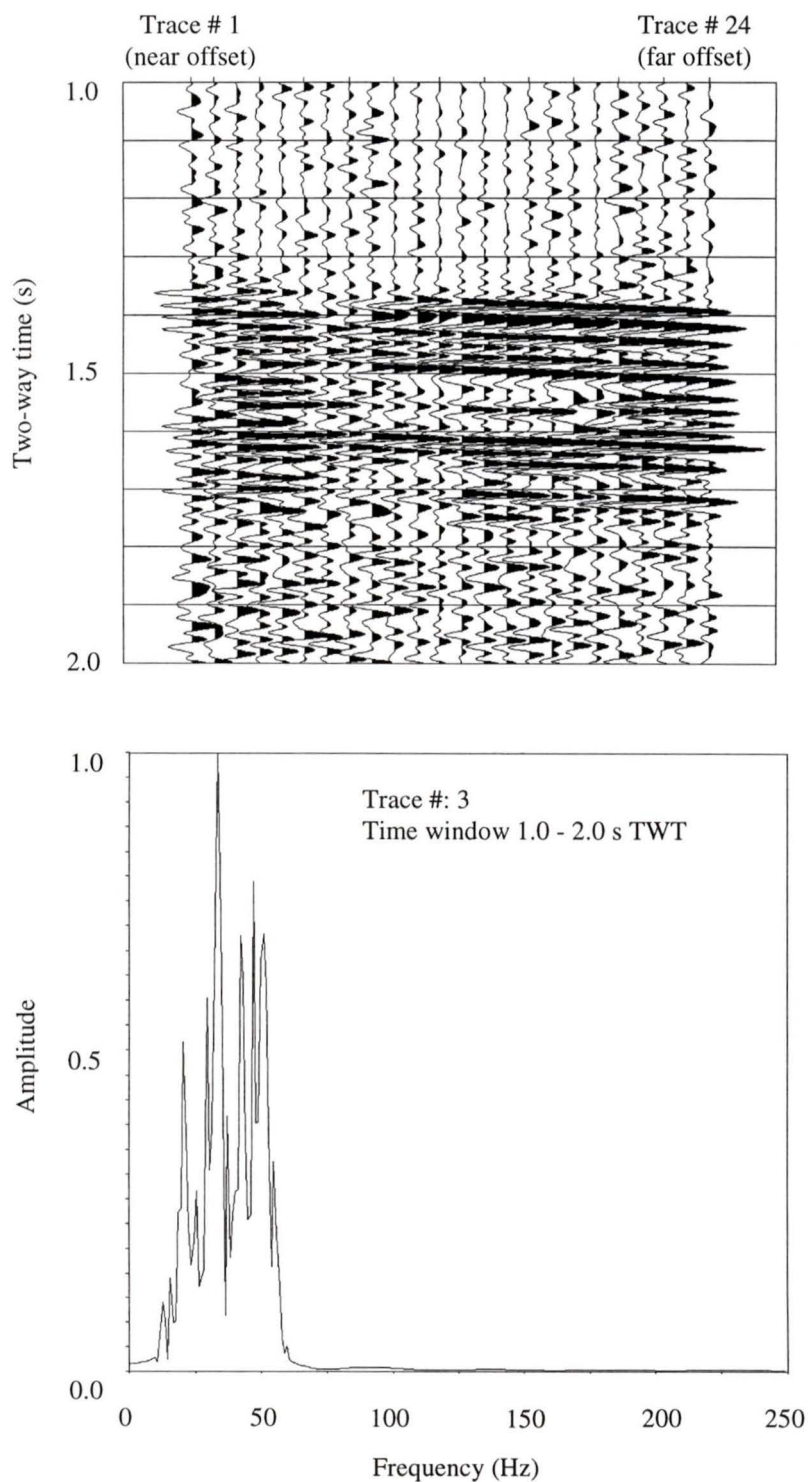


Figure 2.4(c): Shot gather and amplitude spectrum of 2.4(a) after frequency filtering. The frequency trapezium of the filter was 10-20-50-60 Hz. Compared to (b), there is a high loss in the resolution of the data.

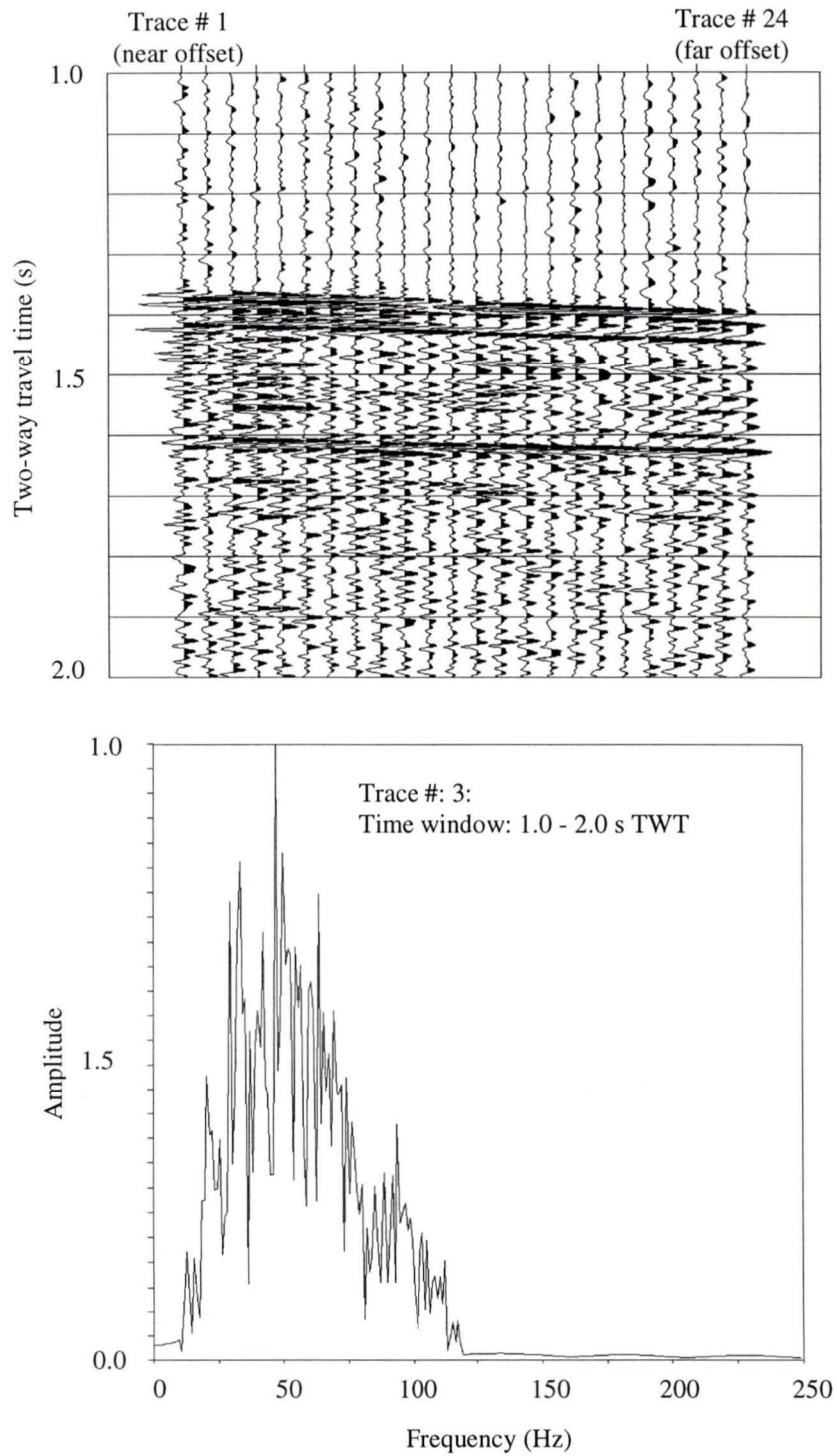


Figure 2.5(a); Shot gather of Figure 2.4(a) after predictive deconvolution. The operator length of the deconvolution operator was 256 ms and the prediction lag was 48 ms. The bubble pulse is removed to a large extent

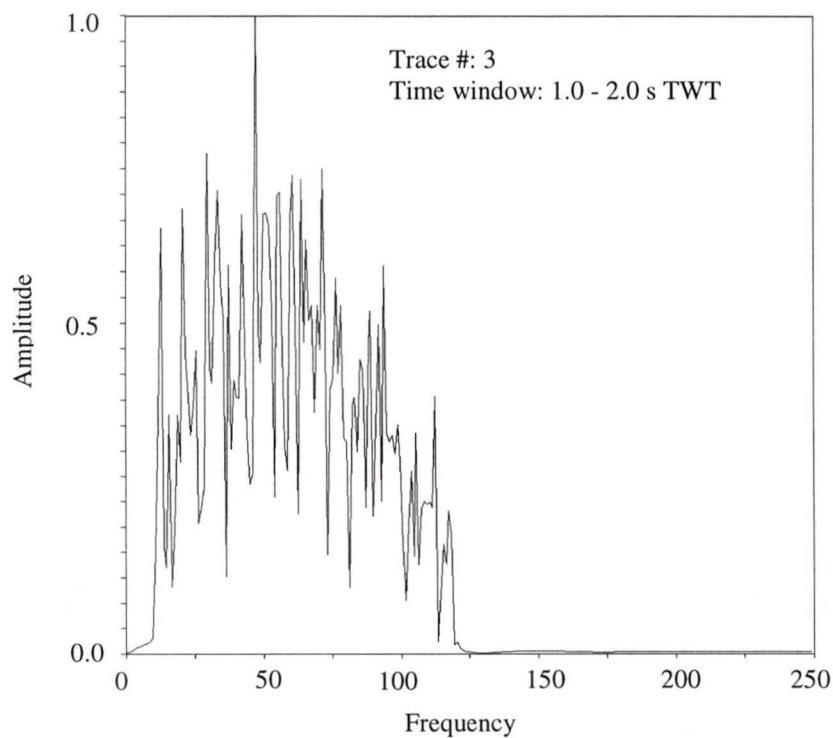
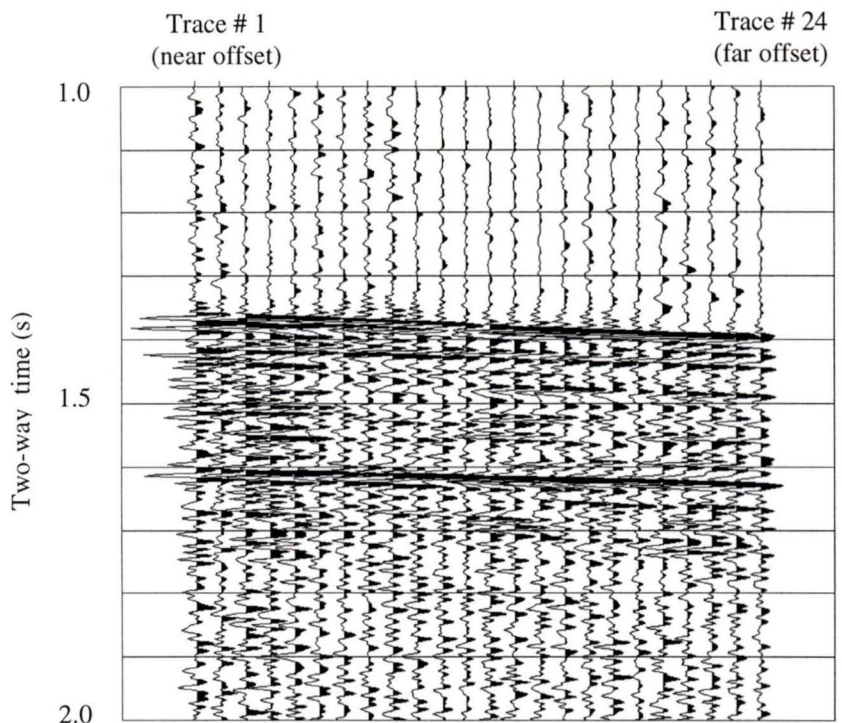


Figure 2.5(b): Shot gather of Figure 2.4(a) after predictive deconvolution. The operator length was 128 ms and the prediction lag was 8 ms. The deconvolution is not very successful in removing the bubble pulse

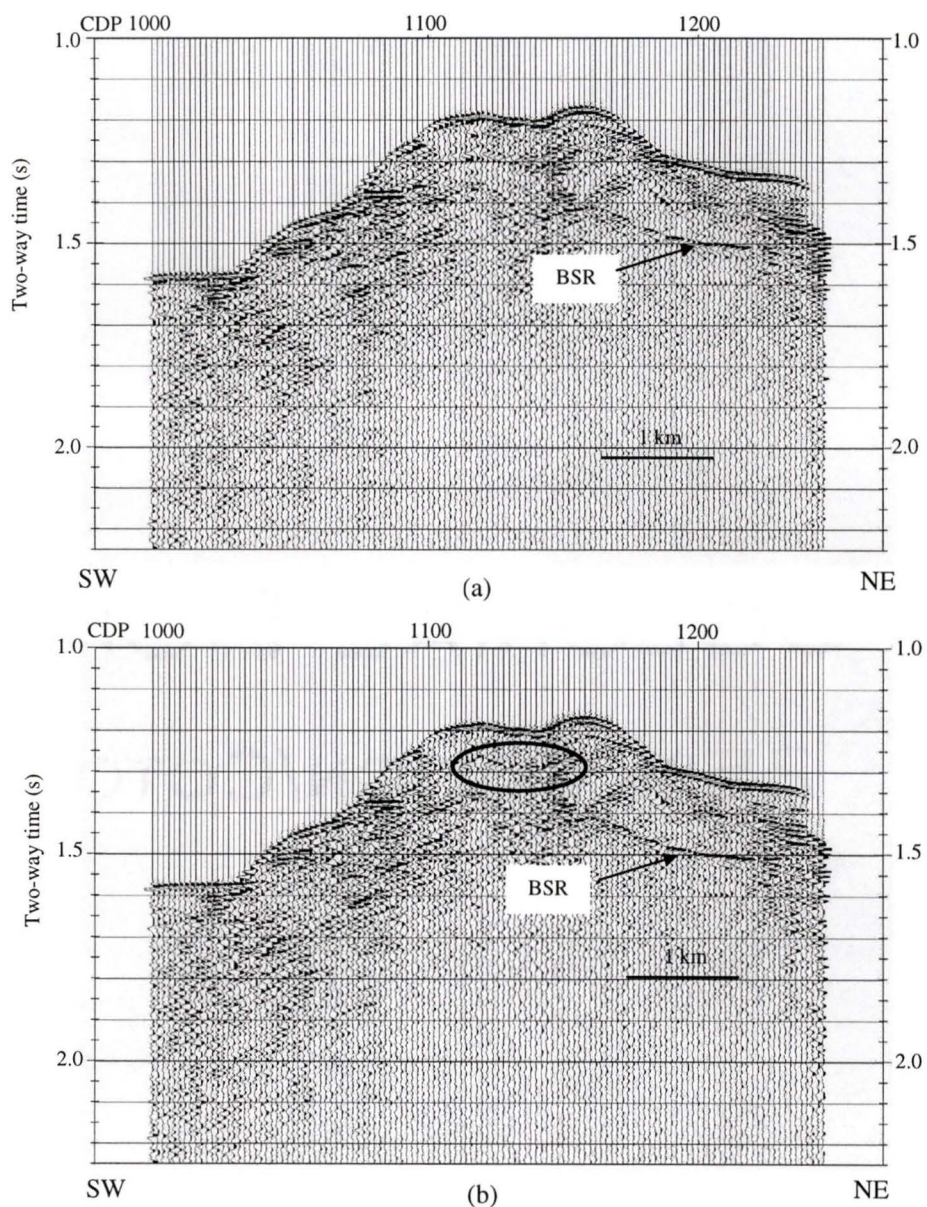


Figure 2.6: (a) Stack section obtained from shot gathers of 2.5 (a). The bubble pulse, though not removed completely, is reduced to a large extent; (b) Stack obtained from shot gathers of 2.5 (b). There is a strong presence of the bubble pulse

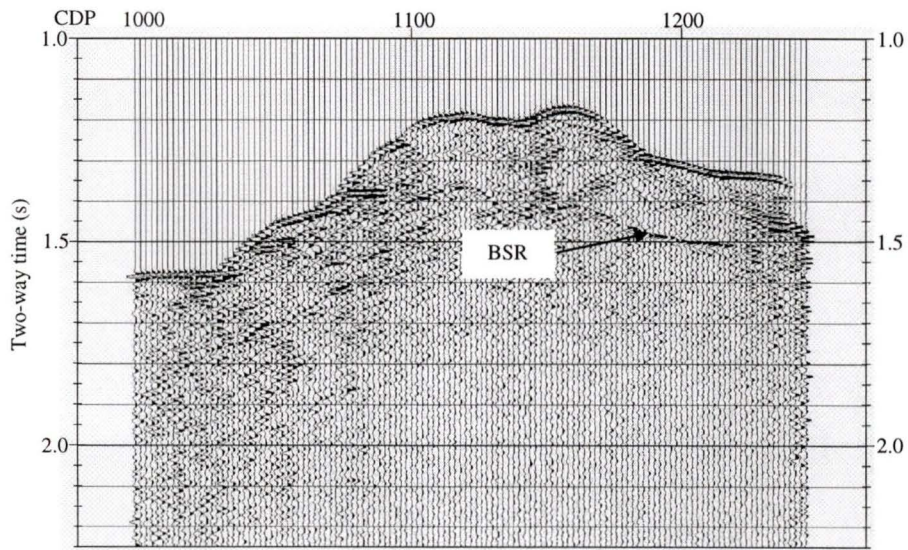


Figure 2.7: Stack section of Figure 2.6(a) after post-stack predictive deconvolution. The operator length of the filter is 128 ms and the prediction length is 16 ms. The bubble pulse is finally removed completely

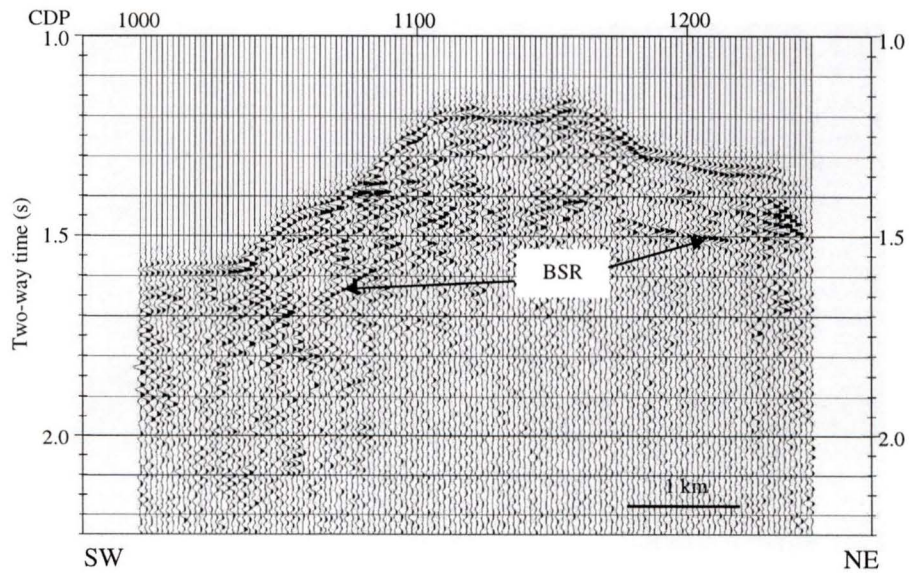


Figure 2.8: Stack section of Figure 2.7 after phase shift migration. There is considerable improvement in the S/N ratio as well as in the continuity of the reflectors.

to remove any high frequency noise that might have been generated during the processing steps. The steps of post-stack processing are summarized in Figure 2.9.

2.3.2 Offset dependent ghost

A ghost reflection is a reflection from the sea surface occurring at a point just above either the shot or the receiver. Usually, ghost reflection can be removed to a large extent, if not completely, by predictive deconvolution and other classical

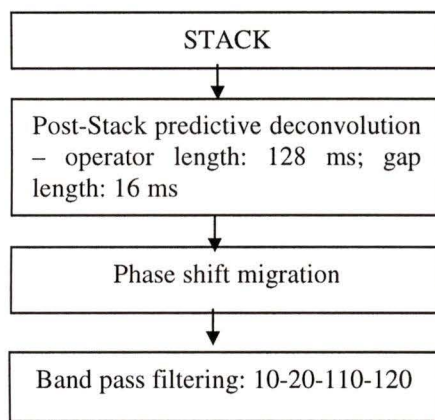


Figure 2.9: Post-stack processing flow chart

deghosting techniques (Jovanovich et al., 1993; Robinson and Treitel, 1980; Sinton et al., 1978; Griffiths et al., 1978; Pflueger, 1972; Backus, 1978). However, in the current survey, it appeared that steamer cable, instead of remaining parallel to the sea surface, typically increased in depth with increasing offset. Thus the ghost reflection did not have the same predictive nature at the near offset

as at the far offset.

In Figure 2.10a, the seafloor reflection separates into two distinct wavelets at far offsets, the primary seafloor reflection and the ghost reflection at the receiver. The time separation of the wavelet is ~ 20 ms (TWT). A closer look at the frequency spectrum of the far offset data (Figure 2.10c) reveals that the ghost reflection gives rise to a notch between 40 and 65 Hz. For a streamer at depth d and data with dominant frequency λ , the surface reflection will interfere destructively with the direct arrival at $d = \lambda/2$. Thus, the notch near 55 Hz (Figure 2.10c) implies that the streamer

depth was about 13 m. This value is consistent with the ~20 ms (TWT) delay between the primary and the ghost, which implies a steamer depth of around 15 m. For the nominal steamer depth of 4m, the notch should occur at a frequency of 185 Hz. (Figure 2.10b), much greater than the maximum frequencies of the data

One solution to the receiver ghost problem was to reduce the bandwidth of the data below this notch. However, this reduction in bandwidth would lead to a significant loss in resolution of the data. Hence, the primary means of reducing the ghost amplitude was in the stacking process itself, since the primary reflections add constructively but the ghost reflections do not.

2.4 Preliminary observations of seismic sections

Preliminary migrated seismic sections show the presence of a strong BSR, not only at regions of topographic highs, but also in a channel between two topographic highs near the base of the channel sediments (Figure 2.11). At several locations, the BSR depth deviated from its normal behaviour, in which a greater BSR depth is expected for greater water depths or pressures. For example, in the seismic section of Figure 2.11, near the topographic high the BSR increased in sub-seafloor depth. These observations call for a detailed study of the variation of the BSR character with respect to the seafloor topography that might give a better understanding of the nature of fluid flow and the distribution and the character of the BSR.

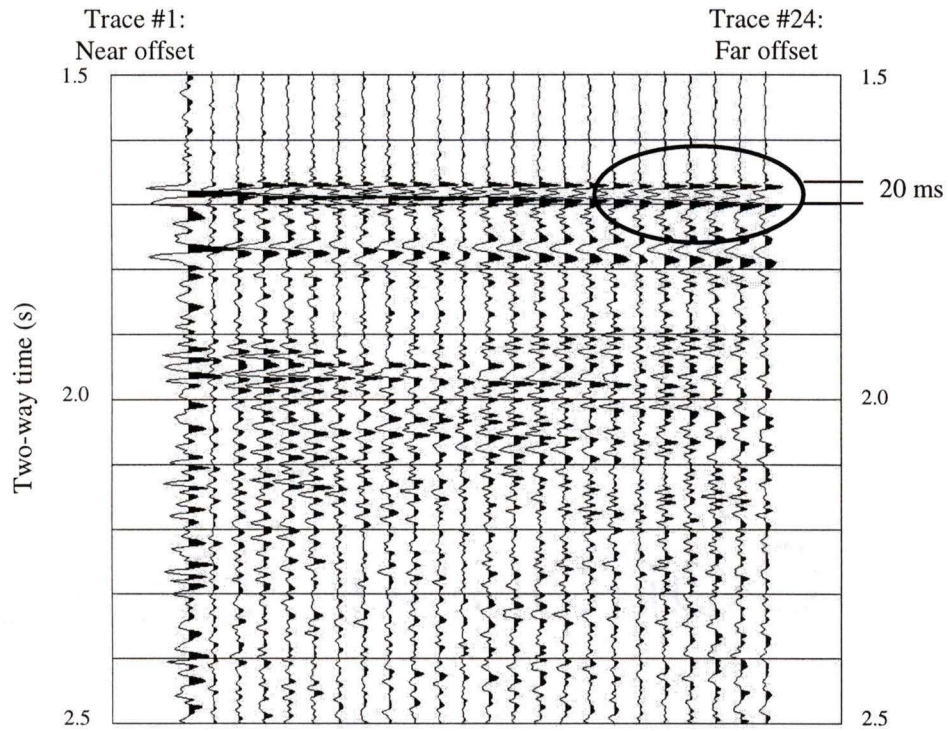


Figure 2.10(a) Shot gather showing the offset dependent ghost reflection. The problem is more severe at the far offset where a doublet appears

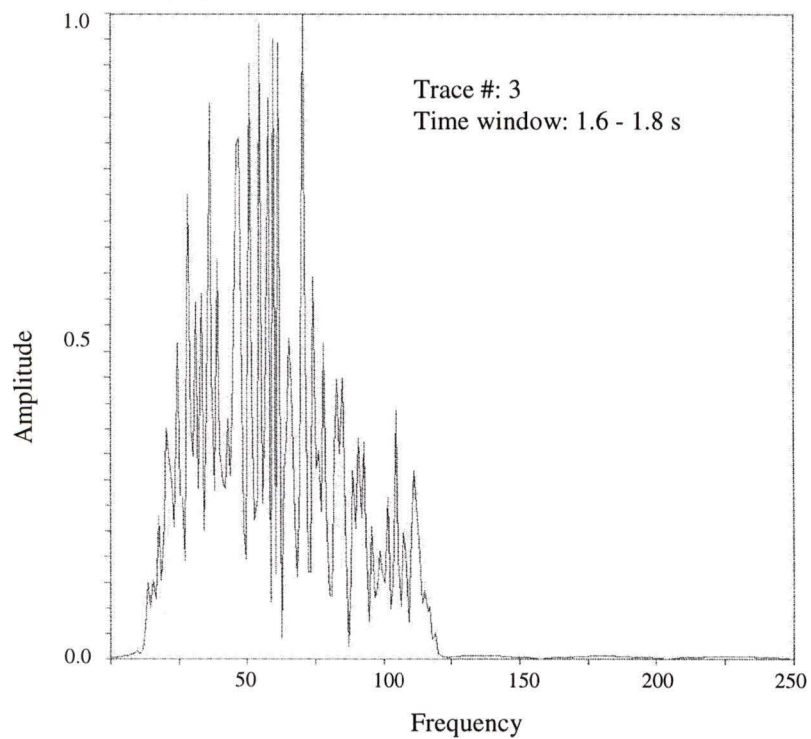


Figure 2.10(b) Amplitude spectrum of near offset trace for shot gather shown in (a).

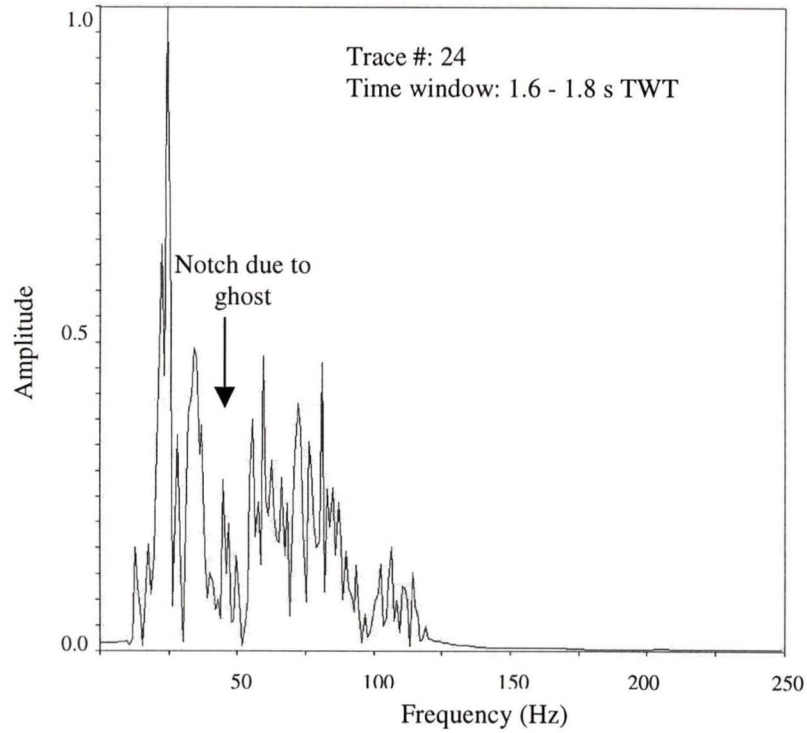


Figure 2.10(c): Amplitude spectrum of far-offset trace for shot gather shown in (a). There is a notch at around frequency of 50 Hz

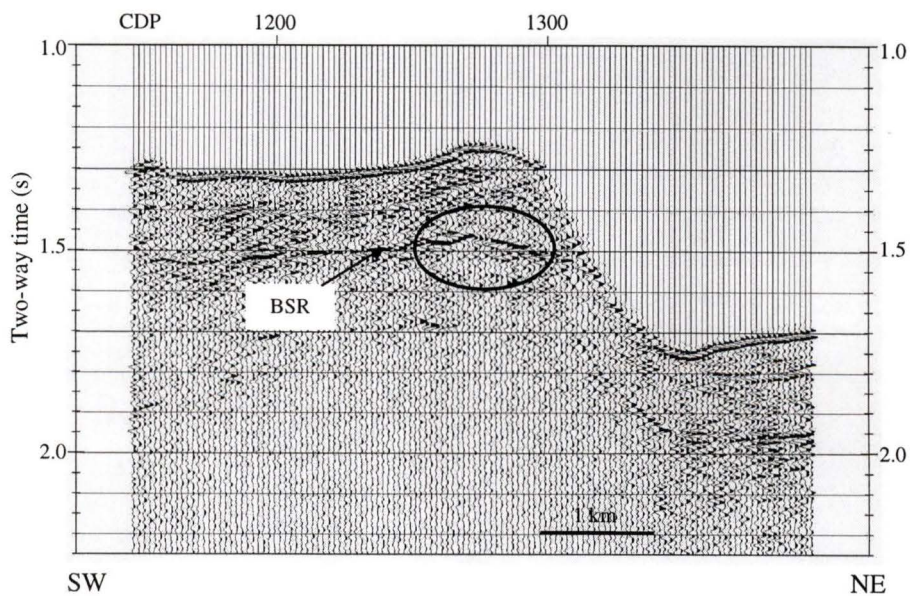


Figure 2.11: Part of line L-21 (migrated) showing the presence of strong BSR at a topographic high as well as at a channel between two topographic highs. The sub-sea floor depth of the BSR, which is supposed to decrease below the topographic high (in circle), is found to rather increase.

CHAPTER 3 HEAT FLOW VARIATIONS FROM BOTTOM SIMULATING REFLECTORS ON THE CASCADIA MARGIN

3.1 Overview

This chapter describes the heat flow patterns in the region of study, estimated from the depth of the BSR. The methodology followed in determining the heat flow values is described in detail and the regional heat flow variations as well as some striking local perturbations are discussed.

Numerous studies have been made on heat flow estimates based on the BSR depth since the first study by Yamano et al (1982). Regional studies of BSR heat flow have identified regional trends, such as arcward decrease of heat flow at the accretionary prisms of Barbados (Fisher and Hounslow, 1990), Nankai (Ashi and Taira, 1993) and Cascadia (Davis et al., 1990; Hyndman et al., 1993). From multichannel seismic reflection profiles across the Cascadia subduction zone offshore Oregon, Trehu et al. (1995) observed that the heat flow through the midslope region is relatively uniform, except for localized zones of higher apparent heat flow related to a small fault and to the intersection of the BSR with the seafloor. Use of BSR depth to identify local heat flow anomalies has been limited but includes an anomaly associated with a thrust fault in Makran (Minshull and White, 1989) and thermal responses to slope failure in Cascadia (Davis et al., 1990) and New Zealand (Townend, 1997). Across the Oregon accretionary prism, Zwart et al., (1995)

observed high temperature gradients over lateral distances less than 300 m which may be caused by advective heat transport mechanisms. Correlation of anomalous high temperature gradients with out-of-sequence thrusts indicated that these structures are currently acting as conduits for warm fluids.

In this chapter, the heat flow pattern across the Cascadia margin is investigated from seismic observations of the bottom simulating reflector. In addition to the general trend of regional heat flow values, the local heat flow anomalies are studied. These local variations, mostly at the flanks of the topographic highs and over topographic highs, may give insight into the channelized migration of the fluids.

3.2 Methodology of heat flow calculations

The computation of heat flow from migrated seismic sections involved the following steps (Yamano et al., 1982):

1. Traveltimes at the seafloor and the BSR were determined from migrated seismic sections. The seafloor two-way time (TWT) was picked by identifying the positive peak while the BSR TWT was picked from the negative peak;
2. The traveltimes were converted to depths (z_{bsr}) using a velocity function from prior multichannel seismic studies (Yuan et al., 1994). A simple velocity function, where the velocity increases linearly with depth, is used

$$v = 1516 + 0.5556 \times z \quad 3.1$$

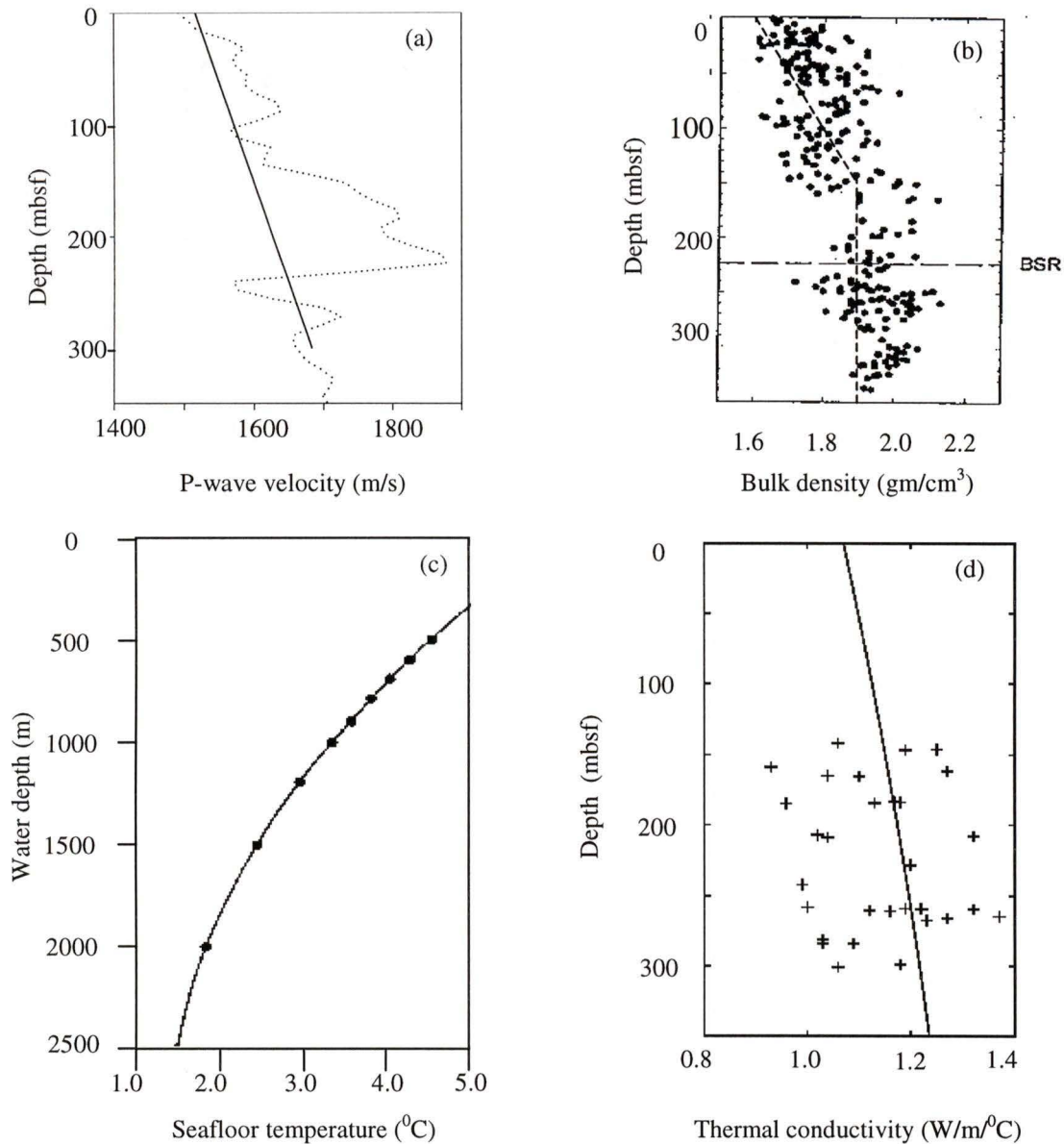


Figure 3.1: (a) P-wave velocity model (solid line) used to convert the traveltimes at the BSR to depths. A constant gradient model was used (solid line), based on general basin velocity trend, where the velocity increases linearly from 1516 m/s at the seafloor to 1680 m/s at 300 mbsf. The dashed curve shows the velocity profile obtained by inversion of multichannel seismic data (Yuan et al., 1994). (b): Density model used in heat flow calculations to estimate the lithostatic pressure at the BSR from depths. The dots represent the actual ODP core measurements (holes 889 A/B and 890B). The dashed line represents the density profile used in heat flow calculations. A two-layer density model was used. In the first layer, which is 150 m thick, density increases linearly from 1.6 gm/cm³ to 1.9 gm/cm³. Density is assumed constant (1.9 gm/cm³) for the second layer. (c): Seafloor temperature-depth profile estimated from vertical profiles in the water column and from near bottom ocean probe data (from Davis et al., 1990). The polynomial fit to the data was used in the heat flow calculations. (d): Variation of thermal conductivity with to depth below seafloor. The '+' indicates actual ODP measurements while the solid line is the polynomial fit (after Davis et al., 1990)

(Figure 3.1a). The variation of P-wave velocity with respect to depth below seafloor can be described by the following relation:

where v is the P-wave velocity in m/s and z is the depth below seafloor in metres.

- The lithostatic pressure at the BSR was calculated using a simple density model based

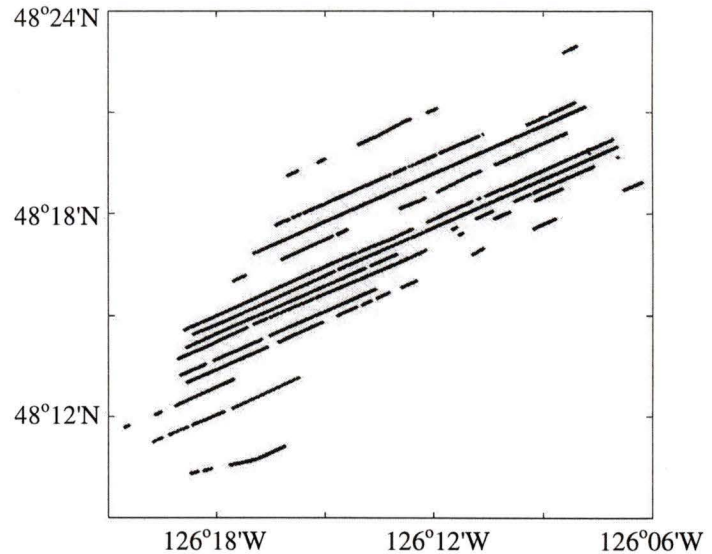


Figure 3.2: Spatial distribution of data points used in heat flow calculations.

on ODP drill hole data at site 889/890 (Carson et al., 1995) (Figure 3.1b). A water density of 1.05 gm/cm^3 was assumed. The sediment layer was divided in two layers. In the first layer, which is from the seafloor to 150 mbsf, density increased linearly from 1.6 gm/cm^3 to 1.9 gm/cm^3 . The second sediment layer was assumed to have a constant density of 1.9 gm/cm^3 .

- The temperature at the BSR depth (T_{bsr}) was determined from the pressure – temperature stability conditions for the methane hydrates. The P-T curve was extrapolated beyond 10 Mpa (Figure 1.5) as approximated by the following empirical relation (Dickens and Quinby-Hunt, 1994):

$$\frac{1}{T} = 3.79 \times 10^{-3} - 2.83 \times 10^{-4} \log(P) \quad 3.2$$

where T is the temperature in Kelvin and P is the pressure in Mpa.

5. The seafloor temperatures (T_{sea}) were taken from data provided by Davis et al. (1990) (Figure 3.1c), based on water column temperature profiles. The seafloor temperature decreased from 5°C at a depth of 300 m, to around 1.5°C at a depth of 2500 m.
6. An empirical relation between thermal conductivity (k) and depth was adopted from Davis et al. (1990) viz.

$$k = 1.07 + 5.86 \times 10^{-3} \times z - 3.24 \times 10^{-7} \times z^2 \quad 3.3$$

where k is the thermal conductivity in W/m² and z is the depth below the seafloor in metres. This relation is consistent with mean values from ODP sites 889/890 (Figure 3.1d), although the latter have a $\pm 10\%$ scatter.

7. The heat flow values (H) were calculated assuming a linear temperature gradient and using the simple conductivity relation:

$$H = k \frac{T_{bsr} - T_{sea}}{z_{bsr}} \quad 3.4$$

Heat flow was calculated over 13 of the 35 lines (Figure 3.2). Interpolation was done between the lines and also along lines to fill the missing values wherever necessary. However, no extrapolation was done beyond the region of heat flow computation. The heat flow data along the seismic lines were structured in a grid with a bin size of 180 m by 180 m. Contour maps were then generated which showed the variation of heat flow with respect to the seafloor topography (Figures 3.3 and 3.4).

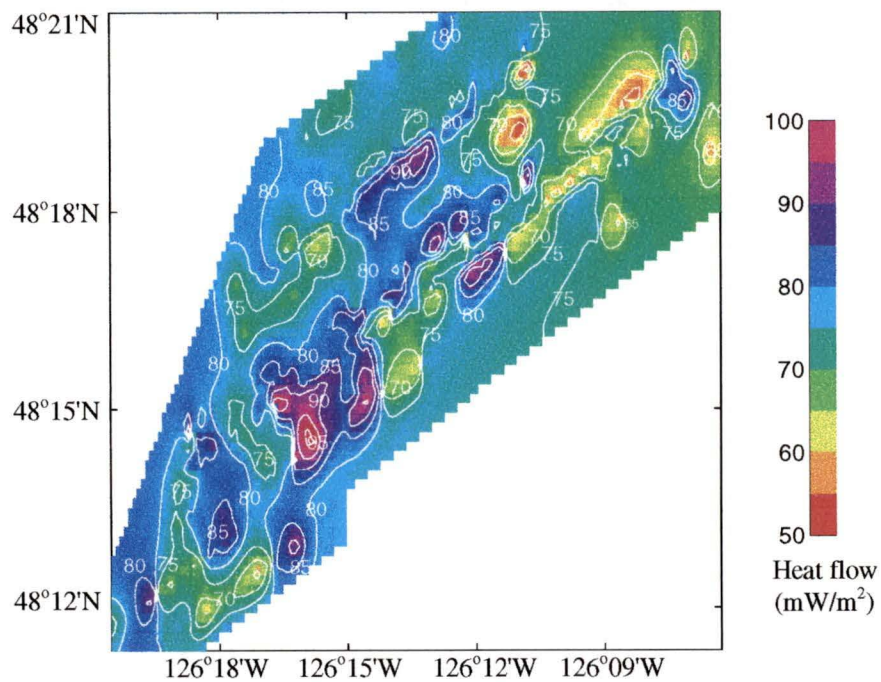


Figure 3.3: Contour map showing heat flow patterns over the area of study

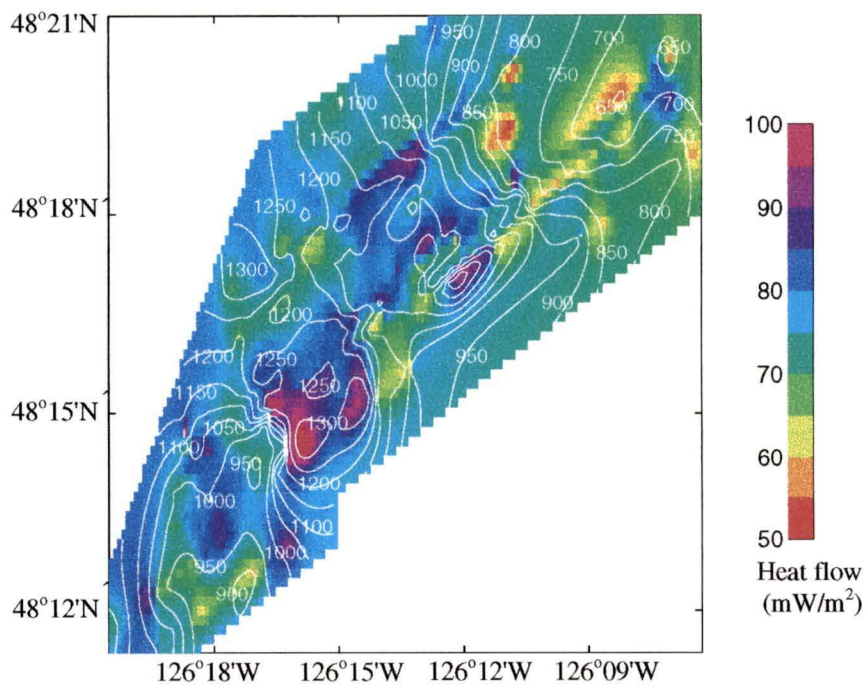


Figure 3.4: Contour map showing variation of heat flow patterns with seafloor topography. The colours represent heat flow while the contour lines indicate the depth of the seafloor

3.3 Errors in heat flow estimates

1. *P-wave velocity*: The depth of the BSR was calculated from the traveltimes by using a velocity-depth function modified after Yuan et al. (1994). A change in the depth of the BSR has direct effects on the values of thermal conductivity and BSR temperature. However, a closer look at equation 3.4 reveals that errors in P-wave velocities are neutralized to a large extent. An increment in BSR depth results in increasing both the numerator and denominator of the right hand side of equation 3.4. Consequently, heat flow values, which are relative measures, are affected only by a small degree.

t_{sea} (s)	t_{bsr} (s)	Heat flow (A) (mW/m ²)	Heat flow (B) (mW/m ²)	Percentage difference
0.824	0.987	58.248	57.176	1.84 %
1.302	1.502	78.526	75.889	3.36 %
1.656	1.870	96.473	92.989	3.61%

Table 3.1: Heat flow estimates with different velocity models. t_{sea} is the two-way travelttime for the seafloor and t_{bsr} is the two-way travelttime for the BSR. In model A, V_p increases from 1516 m/s at seafloor to 1627 m/s at 200 mbsf. In model B, V_p increases from 1516 m/s at seafloor to 1800 m/s at 200 mbsf. The percentage difference between the two models are within reasonable limits.

Heat flow values were computed using two different velocity models. In model A, based on equation 3.1, the P-wave velocity increases from 1516 m/s at the seafloor to 1627 m/s at 200 mbsf. In model B, the velocity increases from 1516 m/s at the seafloor to 1800 m/s at 200 mbsf; this takes into account the high P-wave velocity due to hydrates. The heat flow estimates computed by using both the models are shown in Table 3.1. The

difference in heat flow values in only 1 to 3%, and so the assumption of the simple velocity model applicable to the entire basin (i.e. model A) is sufficient.

2. *Density profiles*: The bulk density of the sediments above the BSR could influence the pressure at the BSR if the pressure due to the sediment layer

t_{sea} (s)	t_{bsr} (s)	Heat flow (A) mW/m ²	Heat flow (B) mW/m ²	Percentage difference
0.824	0.987	58.248	61.766	6.03%
1.302	1.502	78.526	80.549	2.57%
1.656	1.870	96.473	98.194	1.78%

Table 3.2: Heat flow values computed using two different density models. t_{sea} is the two-way traveltime for seafloor and t_{bsr} is the two-way traveltime for BSR. In both models a two layer density model is assumed. In model A, density of first layer increases linearly from 1.6 gm/cm³ at seafloor to 1.9 gm/cm³ at 150 mbsf. Density of second layer is constant at 1.9 gm/cm³. In model B, density of first layer increases from 1.6 gm/cm³ at seafloor to 2.0 gm/cm³ at 150 mbsf. Density of second layer is constant at 2.0 gm/cm³. Heat flow was found to be more sensitive to density errors at shallower depths.

above the BSR is comparable to the water column pressure. However, the effect of density on the heat flow values was small as the sediment grains contribute only a small fraction of the total pressure at the BSR. Most of the pressure was due to the weight of the water column. Also, at greater depths the changes in temperature with pressure are not very significant (Figure 1.5).

Table 3.2 shows the heat flow values computed using two different density models. In the first model (A), density of the first sediment layer increases linearly from 1.6 gm/cm³ at the seafloor to 1.9 gm/cm³ at 150 mbsf. Density of the second layer remains constant at 1.9 gm/cm³. In the second model (model B), density of the first layer increases linearly from

1.6 gm/cm³ at the seafloor to 2.0 gm/cm³ at 150 mbsf. In the second layer of model B, density remains constant at 2.0 gm/cm³. Though heat flow values were found sensitive to density errors over shallower depths (Table 3.2), the effect of density variations on heat flow estimates over most of the region of study was found to be negligible.

t_{sea}	t_{bsr}	Depth of seafloor	Heat flow (Lithostatic) (mW/m ²)	Heat flow (Hydrostatic) (mW/m ²)	Percentage difference
0.518	0.621	766.64	59.76	52.72	11.79%
0.631	0.737	933.88	70.23	64.13	8.68%
0.72	0.858	1065.6	64.3	58.7	8.7%
0.814	0.967	1204.72	64.85	59.72	7.89%

Table 3.3: Heat flow values computed using lithostatic and hydrostatic assumptions. t_{sea} is the two-way traveltime for seafloor and t_{bsr} is the two-way traveltime for BSR. The difference in heat flow values are found to be more at shallower depths.

Previous estimates of heat flow from the variation of the depth of the BSR (Davis et al., 1990; Hyndman et al., 1993; Trehu et al., 1995) have used a hydrostatic model in computing the pressure at the depth of the BSR. Hyndman et al., (1993) argued that since substantial over-pressures are unlikely at the shallow BSR sub-bottom depth, it is reasonable to use the hydrostatic model. However, their assumption not be confirmed by any in situ measurements of pressure. Thus, it is not clear which is the more accurate density model (hydrostatic or lithostatic) and this may represent an error in the heat flow calculations. Heat flow estimates computed using both the models are compared in Table 3.3. The difference between the

heat flow values computed with a hydrostatic assumption and those computed using a lithostatic assumption is greater at the shallow water depths. This behaviour is expected since at shallow depths, the fractional contribution of the sediment grains to the total pressure at the BSR depth, with respect to the contribution of the water column, is greater.

3. *Erroneous traveltimes:* The traveltimes at the BSR and seafloor were picked semi-automatically using INSIGHT/ITA. However, due to poor signal to noise ratio and inaccurate migration velocities, the traveltimes are subject to errors. The error in picking the traveltime of the BSR was estimated to be 3 to 8 ms.
4. *Thermal conductivity:* From equation 3.4 it is clear that errors in thermal conductivity values will directly affect the heat flow estimates. The thermal conductivity – depth profile used was taken from that used by Davis et al. (1990) (Figure 3.1d). The profile was consistent with ODP measurements at drill hole 889/890. The average variation between the conductivity values predicted by equation 3.2 and the observed conductivity values was estimated to be around 10% i.e. around $0.11 \text{ W m}^{-1} \text{ } ^\circ\text{C}^{-1}$ (Figure 3.1d).

It is seen that the errors in BSR depth and temperature approximately cancel and the errors in heat flow arise mainly due to the errors in thermal conductivity (around 10%). Thus, the errors associated with the heat flow values remain within moderate limits (10%).

3.4 Results and discussion

Regional variation

The heat values were projected on to a line perpendicular to the margin (Figure 3.5). The average heat flow value over the region of study was between 70 and 80 mW/m². This heat flow is consistent with values from line 89-03 (Hyndman et al., 1993), also determined from the depth of the BSR. However, Hyndman et al. (1993) used a hydrostatic assumption for determining densities, so their values were recalculated using a lithostatic assumption to be consistent with this study. This

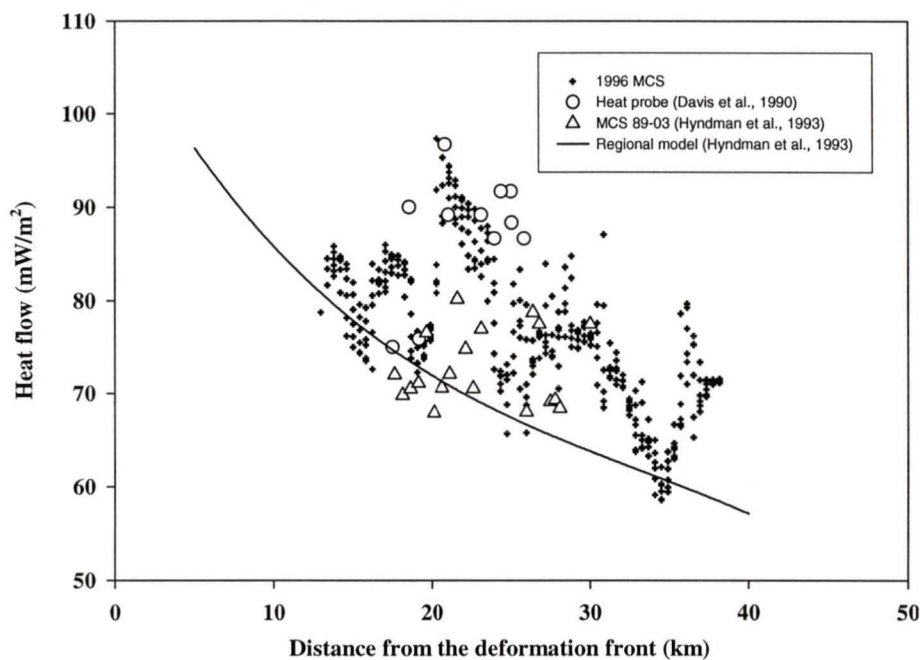


Figure 3.5: Variation of heat flow with respect to the distance from the deformation front. The solid line represents the heat flow profile predicted by the regional model of Hyndman et al. (1993) which takes into account the effects of sedimentation and fluid expulsion. The circles represent heat probe data as reported in Davis et al. (1990). The triangles are the estimates of heat flow from gas hydrate BSR from MCS line 89-03, which runs across the area of study. The heat flow estimates for line MCS 89-03 were recalculated using a lithostatic pressures. The cross hairs are the heat flow estimates from the current study. Though there are some second order variations, there is a general trend of landward decrease in heat flow

average is slightly higher than the estimates of heat flow from BSR depth computed by Davis et al. (1990) over a region 50 km farther north, where the mean was around 70 mW/m². However, the heat flow values estimated in this current study are slightly lower than the heat probe measurements, reported in Davis et al. (1990), which average around 90 mW/m². Trehu et al. (1995) computed a temperature gradient of ~0.051°C/km across the Cascadia subduction zone offshore Oregon, which corresponds to a heat flow of ~55 – 60 mW/m² (assuming thermal conductivity to be between 1.1 and 1.2 Wm⁻¹C⁻¹). This value is lower than those computed in the present study but the oceanic crust off Oregon is slightly older and colder.

The variation in heat flow with respect to the distance from the deformation front shows a general trend of landward decreasing values – from an average of 80 mW/m² at 15 km from the deformation front to an average of around 65 mW/m² at a distance of 25 km farther landward (Figure 3.5). This reflects the processes due to the sedimentation at the Cascadia margin, tectonic thickening at the outer part of the accretionary prism, and the subduction of the Juan de Fuca plate (Davis et al., 1990). The landward decrease is in agreement with the numerical models of heat flow over accretionary prisms (Hyndman et al., 1993).

Local variations

Local heat flow variations are illustrated in the contour map of Figure 3.4, where the seafloor topography is superimposed over heat flow. A consistent pattern was observed with high heat flow values over the steep flanks of topography highs and low heat flow values over the topography highs themselves. Figure 3.6 shows part of the seismic section for line L-17 and the corresponding heat flow values. Low heat

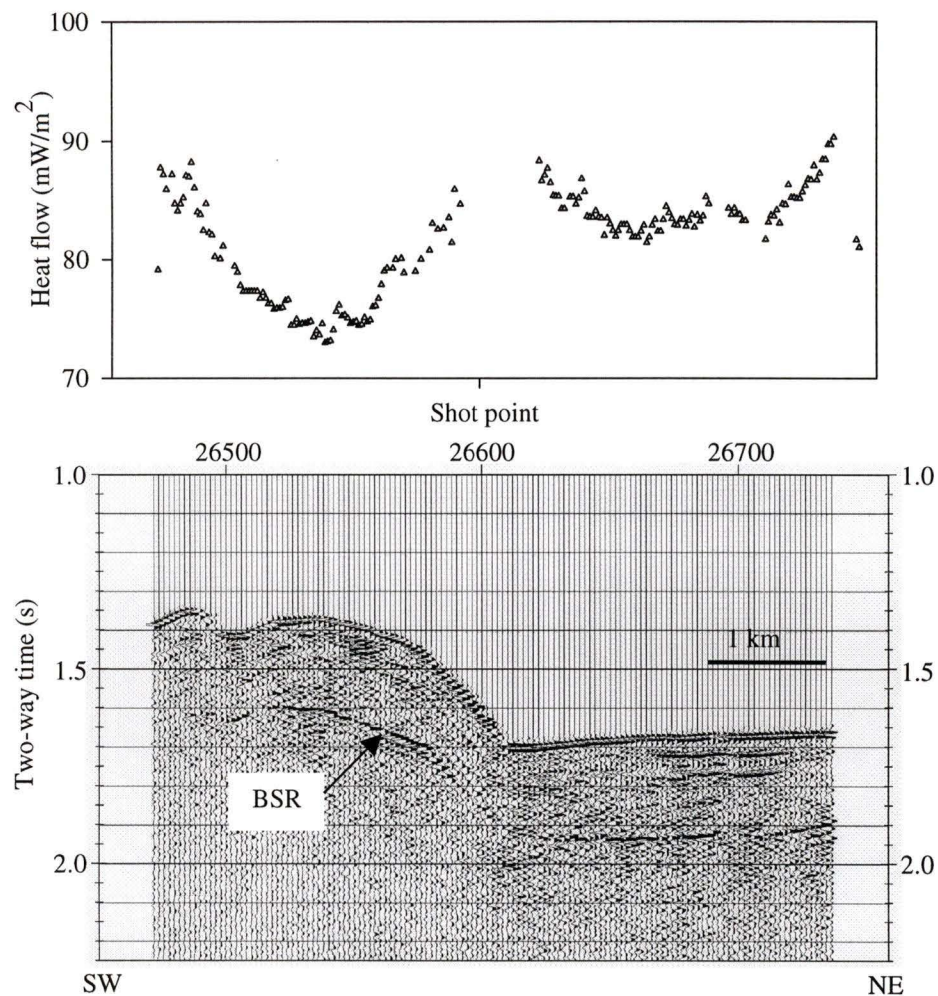


Figure 3.6: Part of line L-17 showing variation of heat flow with respect to seafloor topography. Low heat flow values were observed over topographic highs (box) and high heat flow values were observed over flanks of topographic highs

flow values were observed from shot points 26520 to 26570 (topographic high) and high heat flow values were observed from shot points 26580 to 26610 (flank of topographic high). Figures 3.7 to 3.10 further illustrate the heat flow variations along the seismic lines L-19, L-21, L-22 and L-27 respectively. For line L-27 (Figure 3.10) heat flow values over the topographic high (shot points 35370 to 35400) are comparatively low and there is a sharp increase along the flanks (shot points 35310 to 35320 and shot points 35420 to 35440).

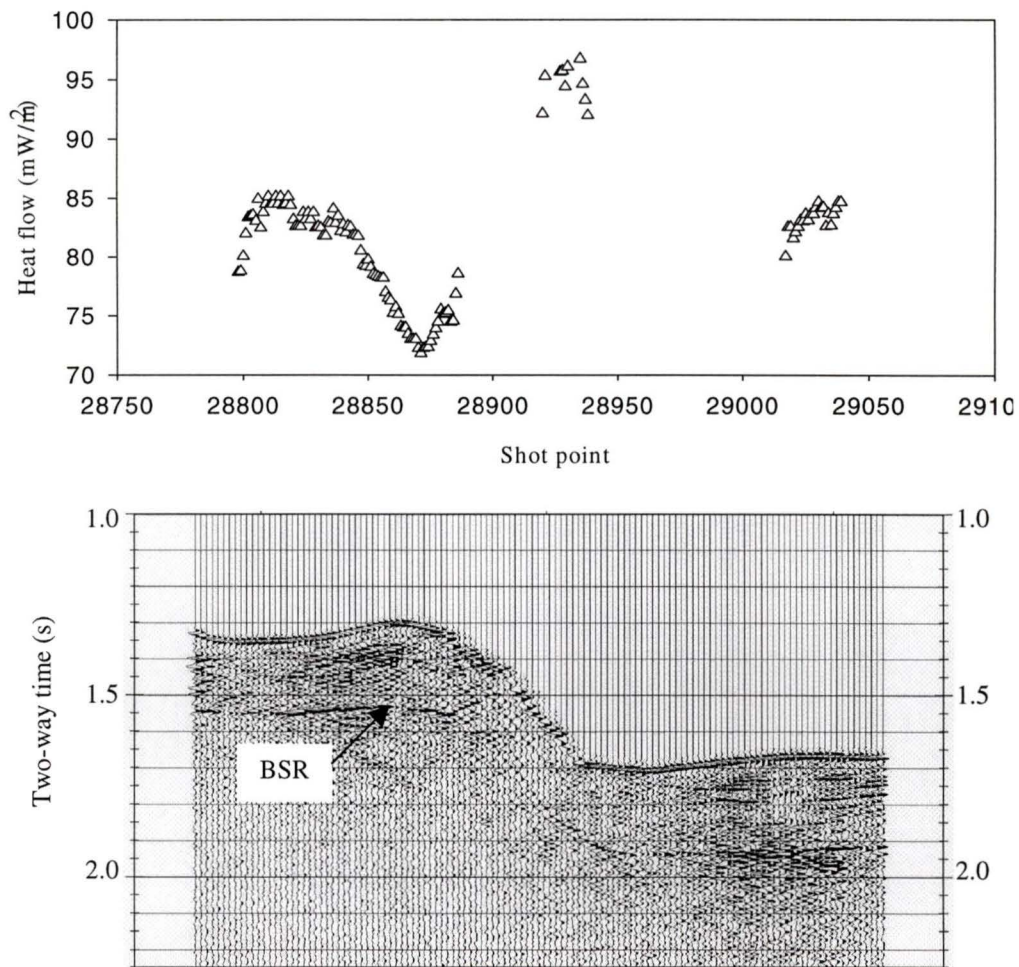


Figure 3.7: Part of line L-19 showing variation of heat flow with respect to seafloor topography.

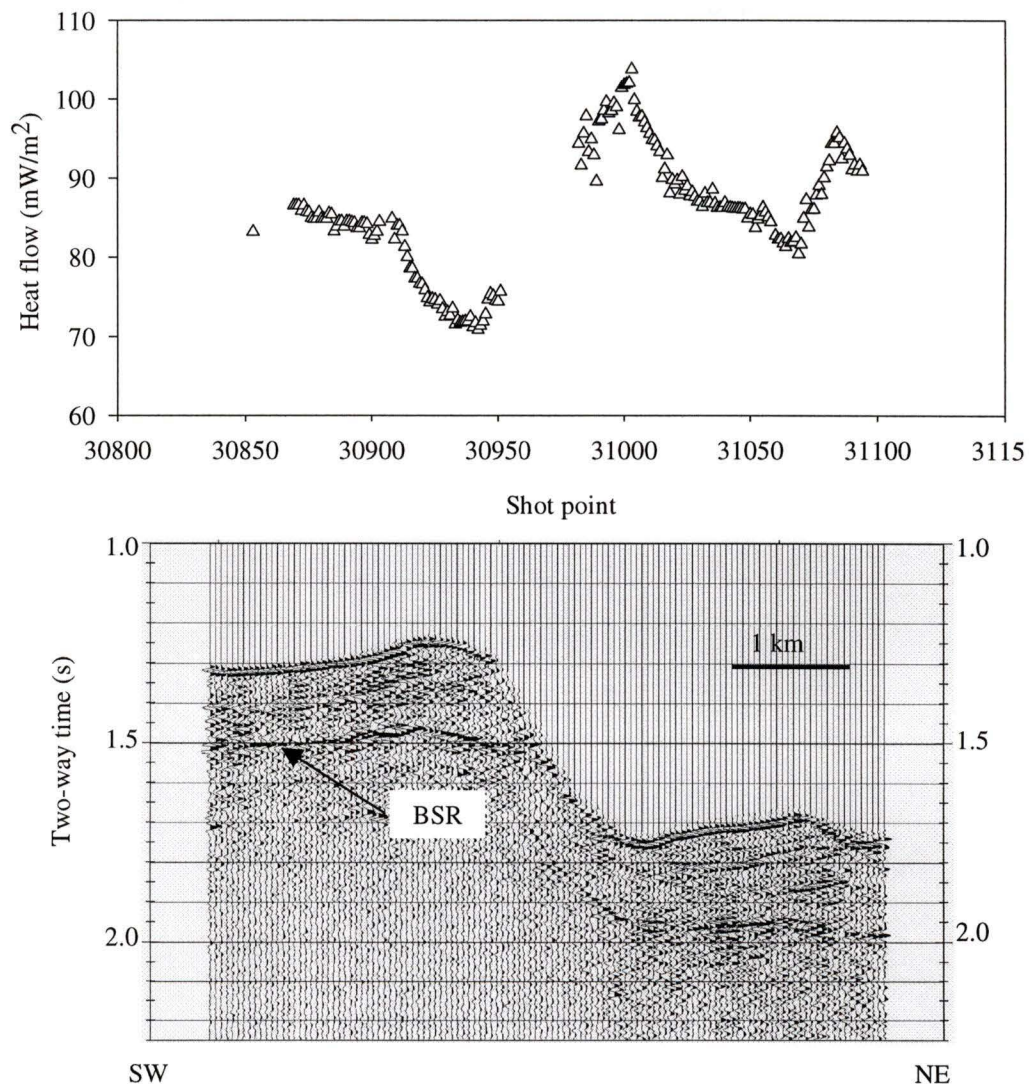


Figure 3.8: Part of line L-21 showing variation of heat flow with respect to seafloor topography.

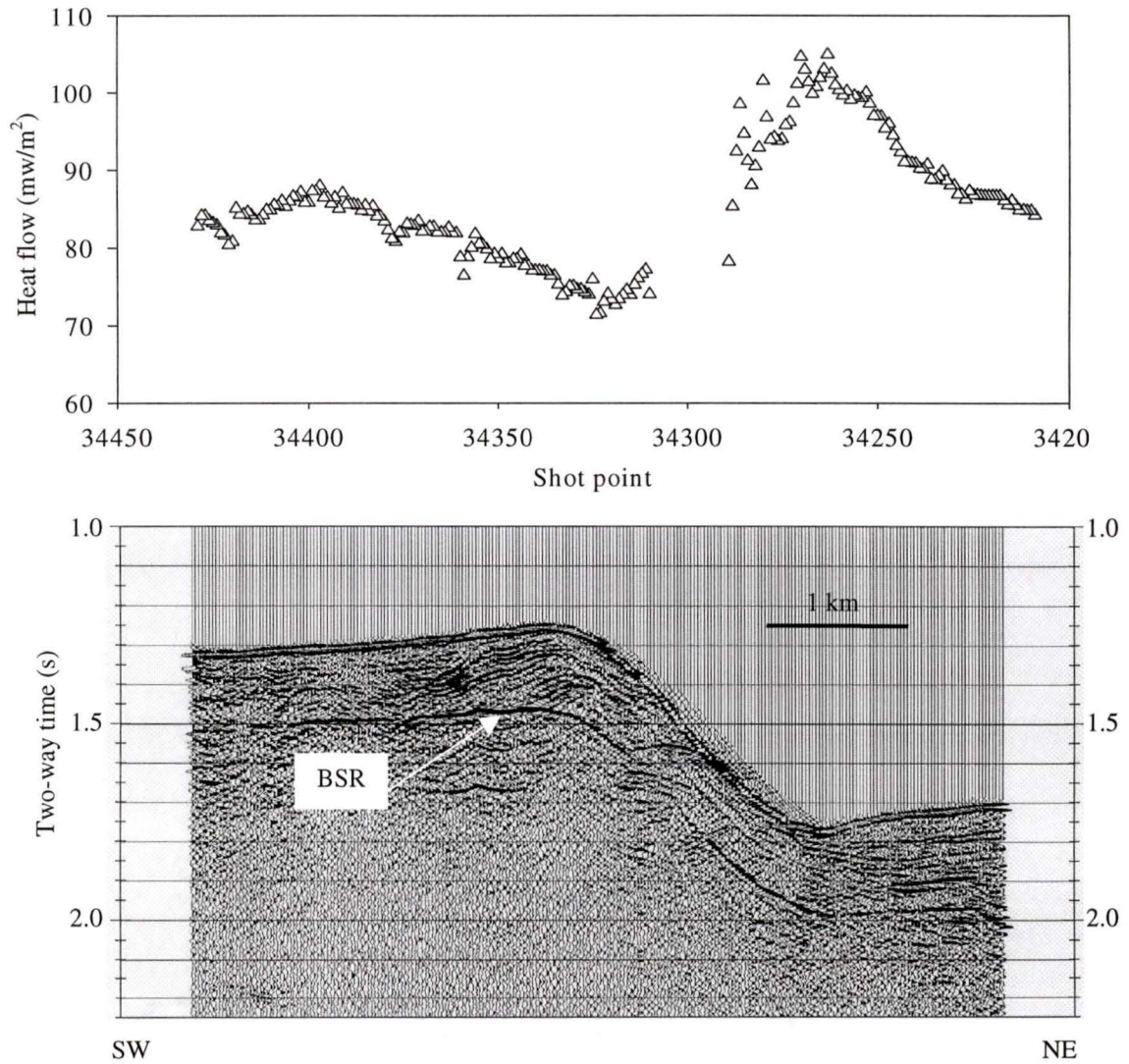


Figure 3.9: Part of line L-22 showing variation of heat flow with respect to seafloor topography.

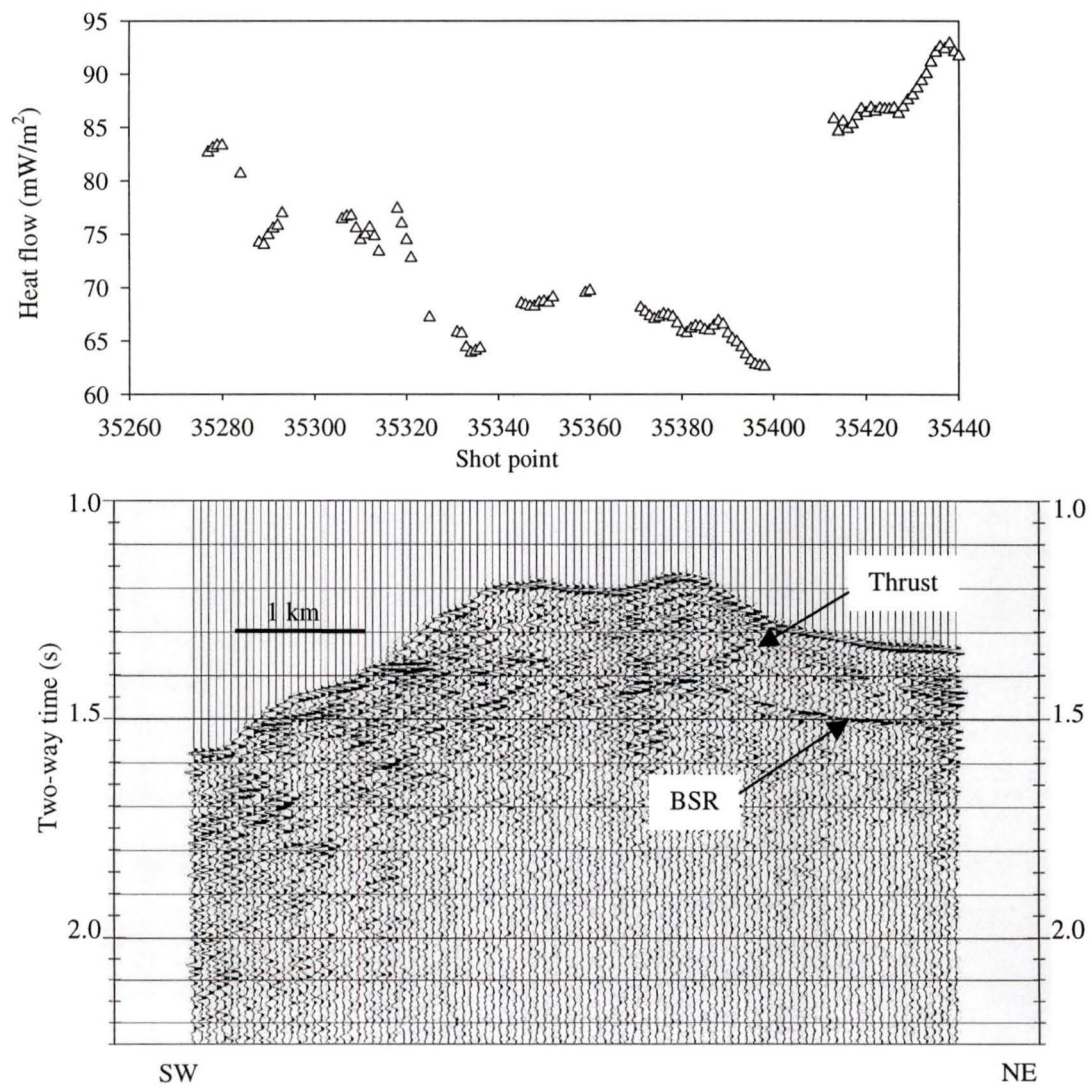


Figure 3.10: Part of line L-27 showing variation of heat flow with respect to seafloor topography. A sharp contrast in heat flow values across the fault is observed.

3.5 Effect of topographic disturbance to superficial thermal gradients

The simplest explanation for the heat flow patterns observed around the flanks of topographic highs might be due distortion due to the topography itself. The pattern of heat flow from the subsurface is distorted near the surface by topographic relief; the flux is intensified by the valleys and attenuated near the ridges. Quantitative analysis of the effect of topography on heat flow has been discussed in detail in Jaeger (1965), Jeffreys (1938), Bullard (1938), Birch (1950, 1967), Jaeger and Sass (1963) and Lachenbruch (1968). In this study, the plane slope method of Lachenbruch (1968) has been used to predict the normalized heat flow values across a dipping sea floor model (Figure 3.11a).

In the method described in Lachenbruch (1968), the irregular topographic surface is replaced by a plane reference surface whose temperature varies locally in proportion to the local relief. To evaluate the topographic effect on temperature by this model at a point with horizontal co-ordinate x_0 and subsurface depth z , a reference plane is passed through $(x_0, 0)$ (Figure 3.11a) and its temperature is assigned as

$$T(x) = Gh(x) \quad 3.5$$

where G is the regional thermal gradient and $h(x)$ is the elevation of the topographic surface relative to the reference plane. Because the vertical gradient is treated as uniform in the topographic irregularities, the effects of heat that escapes horizontally through the sloping surfaces are neglected.

If the temperature disturbance with respect to depth is denoted by $\Delta\theta$, its gradient can be written as

$$\frac{\partial \Delta \theta}{\partial z} = \frac{1}{\pi} \int_{-\infty}^{+\infty} T(x) \frac{(x - x_0)^2 - z^2}{[(x - x_0)^2 + z^2]^2} dx \quad 3.6$$

At the surface $z = 0$, the gradient disturbance approaches

$$\left[\frac{\partial \Delta \theta}{\partial z} \right]_{z=0} = \frac{1}{\pi} \int_{-\infty}^{+\infty} \frac{T(x)}{(x - x_0)^2} dx \quad 3.7$$

If $Gg(x)$ and $Qq(x)$ represent the vertical gradient and heat flow at (x) , then $g(x)$ and $q(x)$ represent these quantities normalized to the regional values G and Q .

The normalized heat flow $q(x)$ can be written as:

$$q(x) = 1 + \Delta q(x) \quad 3.8$$

Assuming positive heat flow in the direction of decreasing z ,

$$\frac{1}{G} \left[\frac{\partial \theta}{\partial z} \right]_{z=0} = g(x) - \frac{G}{G_0} = q(x) - \frac{Q}{Q_0} = \Delta q(x) = \Delta g(x) \quad 3.9$$

G_0 and Q_0 , denoting unit gradient and flux are introduced for dimensional consistency.

Equation (3.7) can be written as

$$\Delta q(x_0) = \frac{1}{\pi G} \int_{-\infty}^{+\infty} \frac{T(x)}{(x - x_0)^2} dx \quad 3.10$$

Using the assumption described in equation (3.5), an approximation of Δq is obtained as

$$\Delta q(x_0) = \frac{1}{\pi} \int_{-\infty}^{+\infty} \frac{h(x)}{(x - x_0)^2} dx \quad 3.11$$

For a plane slope of height H and angle β (between 0 and $\pi/2$), equation (3.11) yields:

$$q(x) = 1 + \Delta q(x) = 1 + \frac{1}{\pi} \tan \beta \ln \left[\frac{x}{x + H \cot \beta} \right] \quad 3.12$$

The normalized heat flow values, $q(x)$, were computed using equation 3.12 for $\beta=10^0$, which is consistent with the seismic sections shown in Figures 3.6 to 3.9. Figure 3.11 shows the predicted heat flow profiles (normalized by the regional average heat flow) with the normalized heat flow values estimated from the BSR depth. The computed heat flow values were normalized by the value of heat flow observed over the flat part of the area, as observed over the sections of Figures 3.6 and 3.8. However, it is difficult to get an estimate of this normalizing factor as other factors like fluid flow can also influence heat flow.

In Figure 3.11, the observed heat flows were plotted using two different normalizing factors. The general trend of the heat flow values estimates computed from the BSR depth is similar to that predicted by Lachenbruch's (1968) model. The observed heat flow values, normalized by a factor of 87 mW/m² (from the heat flow profiles of Figures 3.7 and 3.8), shows excellent match behind the brink of the slope, though there is some discrepancy beyond the toe. On the other hand, the observed heat flow values normalized by a factor of 78 mW/m² (corresponding to a regional average value) are in agreement with the predicted values beyond the toe but the fit is not that close behind the brink of the slope. However, in both the cases the difference is within the estimated error limit of 10% for the heat flow values.

A possible reason for the discrepancy between the predicted heat flow values and those estimated from the depth of the BSR may be the difference in physical properties (mainly thermal conductivity) over the slope basins sections compared to

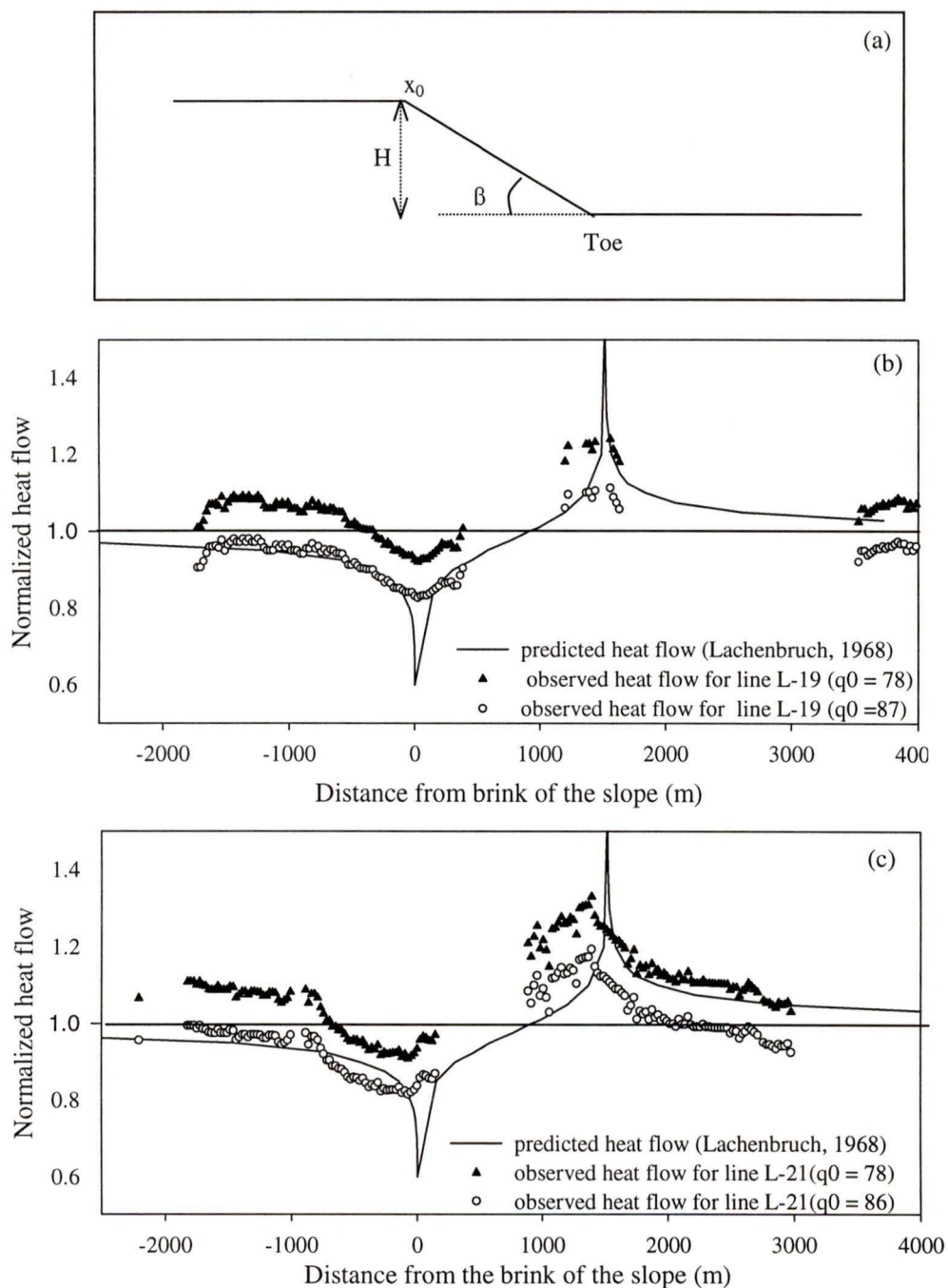


Figure 3.11: (a) Model used to compute the effect of topography on heat flow. A dip of 10° was chosen (β), consistent with the seismic sections shown in Figures 3.5 to 3.9. The value of H was chosen as 282 m for L-21 and 297 m for L-19. (b) Observed and predicted heat flow profiles over part of lines L-19 (b) and L-21 (c). The solid line represents the predicted heat flow profile, the triangles are the observed heat flow normalized by a factor of 78 mW/m² and the open circles are the observed heat flow normalized by 87 mW/m².

that of the adjacent deformed sections. Assessment of the magnitude of the difference in thermal conductivity would require independent measurements of conductivity, for instance, at sites on the hanging wall and the foot wall of thrust faults. However, a

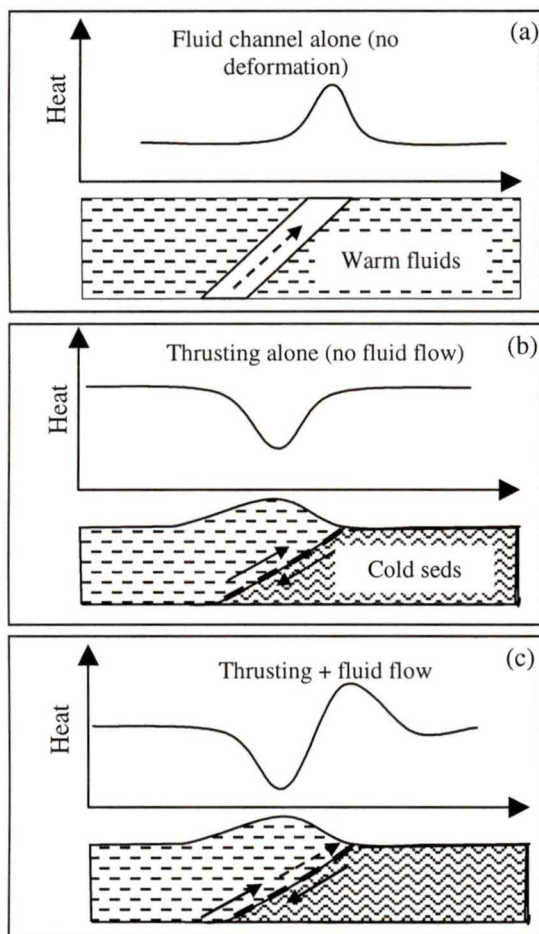


Figure 3.12: Possible explanation for the correlation between the seafloor topography and heat flow. (a) Migration of warm fluids only, upwards along a channel, leads to anomalous high heat flow. (b) Faulting, which brings down cold sediments, lowers the heat flow and causes an elevation in the seafloor. (c) When both phenomena take place, a pattern of low heat flow over topographic high and high heat flow over flanks of topographic high is observed.

review of the ODP literature (Carson et al., 1995; Westbrook et al., 1994) related to the Cascadia margin indicates that the thermal conductivity values are generally consistent over the entire region, with values similar to those shown in Figure 3.1d. Thus, without additional information regarding the difference in physical properties of seafloor material across thrusts, there is insufficient data to assess the effect of physical property variations on heat flow estimates. However, it should be noted that the computed heat flow values (normalized) are within 10% (estimated error bound) of the predicted values.

Considering the uncertainty in calculating the effect of topography, alternative processes, which can produce

the localized heat flow patterns around the flanks of topographic highs, should also be considered. Channeled migration of warm fluids along thrusts is one possible explanation of the observed correlation between heat flow and topography (Figure 3.12). Migration of warm fluids alone, upward along a channel, will give rise to anomalous high heat flow values, independent of the topography (Figure 3.12a). A fluid channel may exist along a thrust fault, which also produces a topographic high in the hanging wall block. The existence of thrust fault is indicated on the seismic sections at the base of the topographic high, particularly along line L-27 (Figure 3.10). Furthermore, thrust faulting brings the cold sediments down and thus will lead to anomalous low heat flow values over the topographic high (Figure 3.12b), as suggested by Davis et al. (1990). When both phenomena take place concurrently (Figure 3.12c), a flow pattern similar to that observed (Figures 3.6 to 3.10) may result; i.e. low heat flow over topographic highs and high heat flow over the flanks of topographic highs.

Thus, an integrated quantitative analysis, that takes into account the effects of topography, fluid flow and faulting, is required to get a complete understanding of the thermal regime of accretionary wedge.

CHAPTER 4 STUDY OF THE SEAFLOOR AND BSR

REFLECTION COEFFICIENTS

4.1 Overview

In this chapter, the reflection coefficients of the seafloor and the BSR are estimated. The methodology followed to calculate the reflection coefficients is discussed in detail and the variation of reflection coefficients (both of the seafloor and the BSR) is described.

On the Cascadia margin, prior studies of reflection coefficients of the seafloor and the BSR have been made both from single channel data (Fink, 1995; Fink and Spence, 1998) and from the short offset multichannel system used in this study (Mi, 1998). From multi-frequency single channel seismic reflection data, Fink and Spence (1998) observed a strong correlation between the seafloor topography and the BSR reflection coefficient. BSR reflection strengths were found to reach localized maximum values of 0.15 to 0.18 under topographic highs, indicating that topography provides a major control on either hydrate or gas concentrations. It was proposed that the flow of methane-bearing fluids from broad areas at depth becomes significantly more focussed under the closed topographic highs. Their hypothesis suggests that the BSR acts as a partial or temporary seal for trapped gas, at least under the topographic highs. On the flanks of topographic highs, large seafloor amplitudes were compared from data recorded with a 75 Hz source, relative to data using a 30 Hz source. By

fitting synthetic seismograms to the two data sets, Fink and Spence (1998) concluded that the high seafloor amplitudes were probably produced by a 2 m thick high-velocity layer at the seafloor, with velocities and densities corresponding to those of carbonate.

Using short-offset multichannel seismic reflection data in a nearby area, Mi (1998) observed high seafloor reflection coefficients on the west flank of a local topographic high with low reflection coefficients over the topographic high itself. This variation in reflection coefficients with respect to seafloor topography was attributed to possible enhanced fluid flow into the region, perhaps associated with a thrust fault. The BSR reflection coefficients were found to have only a slight correlation with the topographic highs in that study.

4.2 Calculation of reflection coefficients

The computation of reflection coefficients for seafloor and BSR from unmigrated stack seismic sections involved following use of multiple to primary amplitude ratios (Warner, 1990):

1. Picking of seafloor and BSR amplitudes;
2. Computation of the conversion factor that maps seafloor amplitudes to reflection coefficients, utilizing seafloor multiple-to-primary amplitude ratios;
3. Computation of BSR reflection coefficients by using the ratio of BSR amplitudes to seafloor amplitudes and by accounting for seafloor transmission losses.

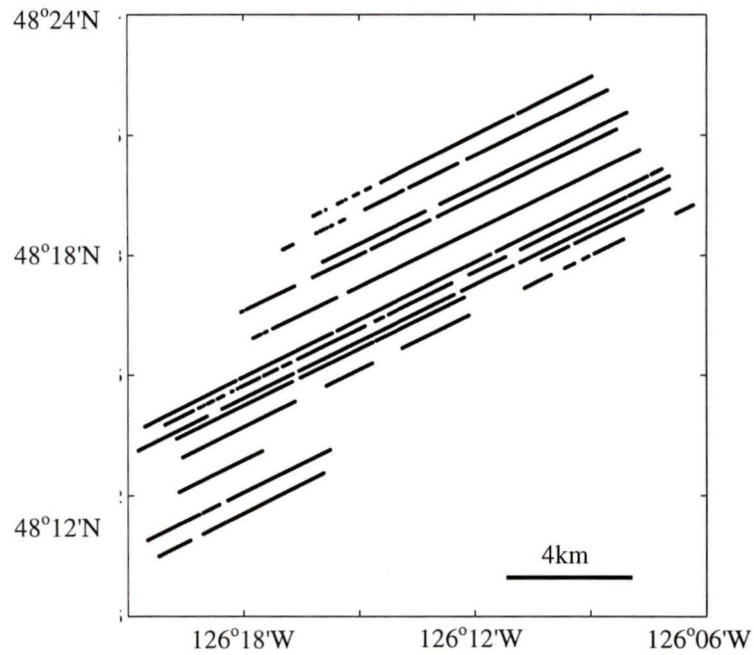


Figure 4.1(a): Spatial distribution of points over which seafloor amplitudes were picked

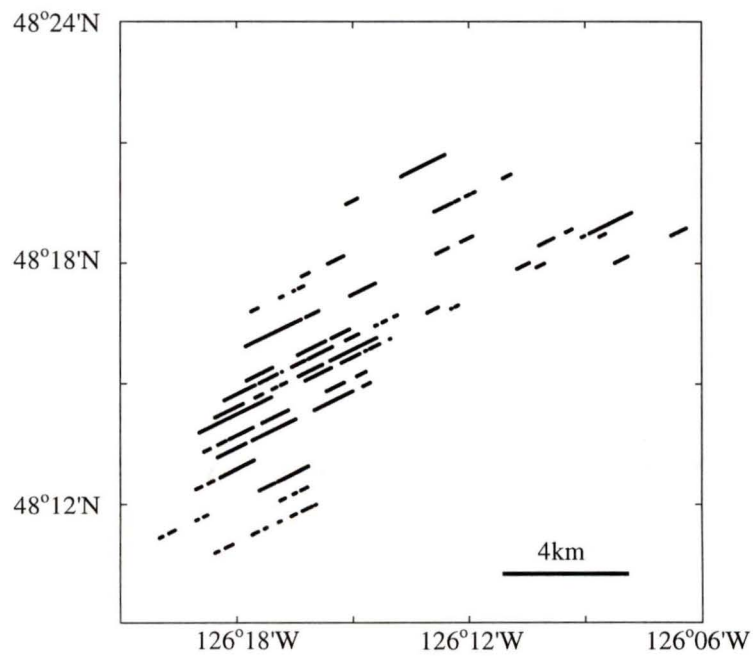


Figure 4.1(b): Spatial distribution of points over which BSR amplitudes were picked

4.2.1 Picking of amplitudes

Event horizons for the seafloor, BSR and the seafloor water bottom multiple (WBM) were picked interactively from the stacked sections. The WBM was recorded only for water depths less than 1470 m or 2.0 s two-way-time. Amplitude picking was done by selecting the maximum positive amplitudes for the seafloor (over a time window of 60 ms) and maximum negative amplitudes for BSR and seafloor WBM (over a time window of 30 ms). The seafloor reflection was of good quality and amplitude picking was done for large number of sections (Figure 4.1a). Picking of the BSR amplitudes was difficult especially over regions where strong sediment reflections were present. Compared to the traveltimes data used for heat flow calculations in the preceding chapter, there was much less BSR amplitude data of adequate quality for calculation of reflection coefficients. This was due to the fact that the traveltimes data (for heat flow calculations) were obtained from migrated stack sections which had a higher signal to noise ratio than the unmigrated stack sections used for amplitude picking. In the migrated sections, diffraction effects due to dipping horizons and localized faults were minimized to a large extent, thus providing a well defined BSR. In the stack sections, even if the BSR was well defined, the BSR amplitudes were contaminated by the diffraction effects due to the faults. BSR amplitude picking was done only for those traces where the BSR continuity was well defined and the amplitudes were not contaminated (Figure 4.1b).

4.2.2 Determination of conversion factor

The seafloor reflection coefficient (RC_{sf}) can be calculated from the amplitudes of the seafloor primary reflection and the seafloor water bottom multiple reflection by using the following relation (Warner, 1990):

$$RC_{sf} = \frac{C_1 \times A_{sf_multiple}}{A_{sf_primary}} \quad 4.1$$

where $A_{sf_multiple}$ is the amplitude of seafloor water bottom multiple, $A_{sf_primary}$ is the amplitude of the seafloor primary reflection and C_1 is a spherical divergence correction factor (Figure 4.2). If a spherical divergence correction has already been applied during data processing, the C_1 equals to unity.

The reflection coefficient of the BSR (RC_{bsr}) is calculated from seafloor reflection coefficient by taking the ratio of BSR and seafloor amplitudes, with additional consideration of transmission loss. For an incident wave of unit amplitude (Figure 4.2), the amplitude of down-going transmitted wave at the seafloor is $1-RC_{sf}$. The up-going transmitted wave has an amplitude of $1+RC_{sf}$, as the reflection coefficient changes its sign for the up-going wave on account of phase reversal. The ratio of amplitudes of the seafloor and the BSR can be written as:

$$\frac{A_{sf}}{A_{bsr}} = \frac{RC_{sf}}{(1 - RC_{sf})RC_{bsr}(1 + RC_{sf})} \quad 4.2$$

where A_{bsr} is the raw amplitude of the BSR. Re-arranging equation 4.2 we get:

$$RC_{bsr} = \frac{A_{bsr}}{A_{sf}} \times \frac{RC_{sf}}{(1 - RC_{sf}^2)} \quad 4.3$$

Warner’s method of calculation of reflection coefficients is based on the following assumptions:

1. Receiver offset should be small compared to the water depth so that the wave propagation can be considered as normal incidence. After NMO correction, the stack section is almost zero-

offset, and so this premise is satisfied.

2. Seafloor is assumed to be a simple interface between liquids and elastic solid half space such that no energy is lost due to non-elastic processes. However, from physical property measurements of sediment cores collected in this

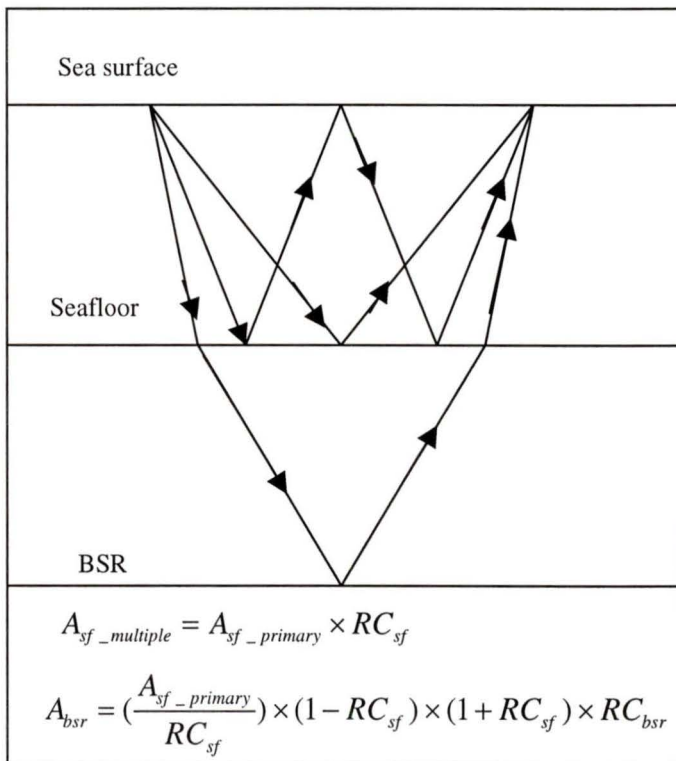


Figure 4.2: Seafloor and BSR reflection coefficient calculation using multiple/primary method

region (Mi, 1998), it was observed that the seafloor is

generally covered by a layer of soft mud with a maximum thickness of 2.5 m. This layer of mud, with density as low as 1300 kg/m³, overlies the normal, denser glacial clay with a bulk density of about 1600 kg/m³. Thus, this premise is not strictly satisfied.

3. Seafloor is assumed to be flat and smooth and scattering and defocussing effects due to topographic variations were neglected. However, in the region of study, scattering due to small scale topographic variations are an important source of energy loss. Unfortunately, it is difficult to have a quantitative estimate of this loss as the roughness of the seafloor is unknown. Also, the tilt of the streamer cable was different when shooting along the direction of the wind/swell compared to the tilt when shooting against the wind/swell. Thus, though the scattering and defocussing effects were neglected during the process of calculation of the reflection coefficients, they do affect the amplitudes of the seafloor and the BSR.

In practice, equations 4.1 and 4.3 are not applied to every trace in the survey where amplitudes are measured. Rather, a conversion coefficient is found that maps seafloor amplitudes to reflection coefficients, and the conversion coefficient is applied to the measured amplitudes.

Equation 4.1 can be rewritten as:

$$RC_{sf} = C_1 \times C \times A_{sf_primary} \quad 4.4$$

where C is the conversion factor given by:

$$C = \frac{A_{sf_multiple}}{A_{sf_primary}^2} \quad 4.5$$

Similarly, equation (4.3) can be re-arranged to yield the BSR reflection coefficient, in terms of seafloor amplitude, BSR amplitude and conversion factor (C), as follows:

$$RC_{bsr} = \frac{A_{bsr} \times C}{(1 - A_{sf}^2 C^2)} \quad 4.6$$

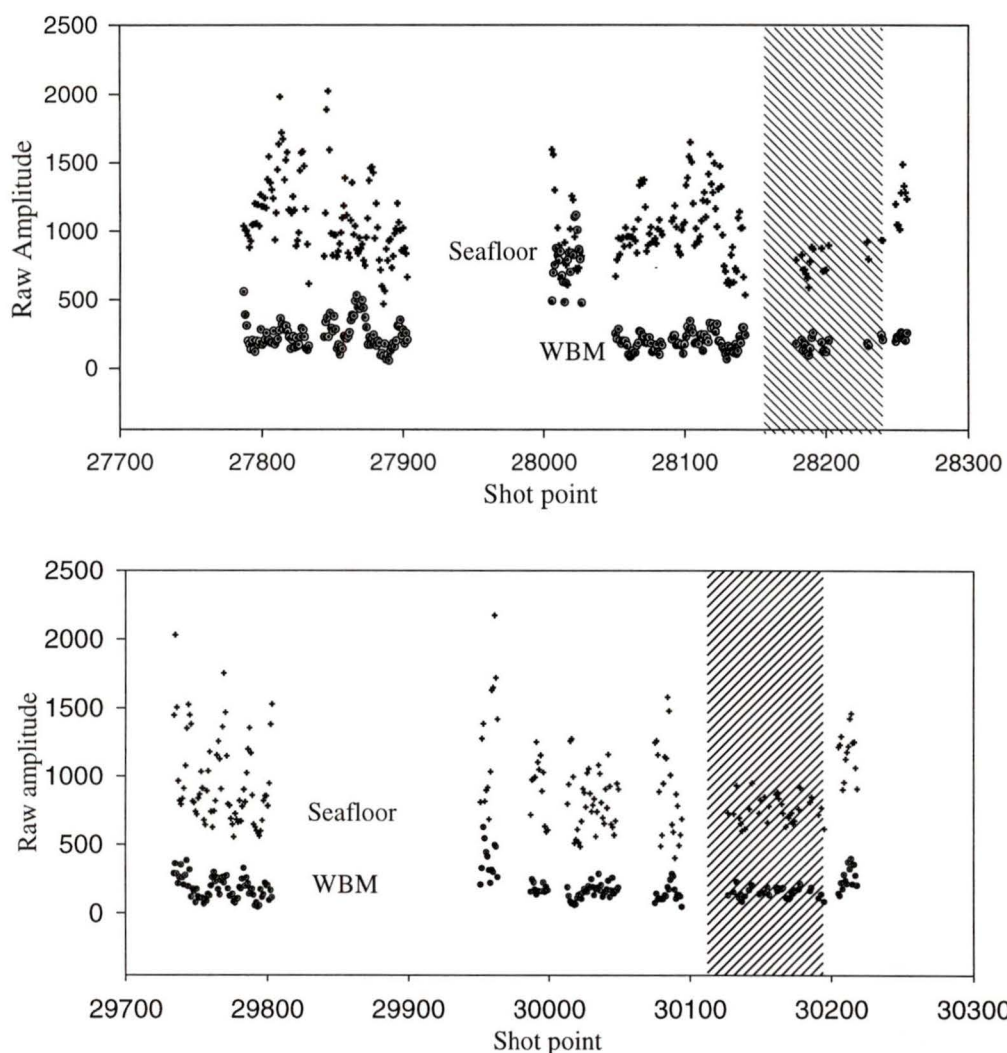


Figure 4.3: Computation of conversion factor. The flat portion (shaded area) of lines L-16 (above) and L-18 (below) were chosen for the computation of conversion factor. An average factor of 0.000265 was determined

The value of this conversion factor (C) is computed from equation (4.5) using values of amplitudes of primary and multiple reflections of the seafloor over a region where the effects of defocussing and scattering are minimum. In practice, this should be over the flattest portion of the area. Use of a single conversion factor for the entire region is based on the assumption that the source amplitude remains constant over the entire region and there is no gain control applied to the

seismic data during processing. The gun pressure for the area of study was kept at a constant value of 1800 PSI, justifying the validity of the constant source assumption.

Selection of seismic lines for the calculation of the conversion factor is very crucial. Figure 4.3 shows the raw amplitudes of the seafloor primary reflection and WBM for lines L16 and L18 - which were used in the computation of the conversion factor. For line L16, the average raw amplitude of the seafloor primary reflection was found to be 805. The corresponding average value for WBM was 173, yielding a conversion factor of 0.000267 (equation 4.5). For line L18, the average values of raw amplitudes were 759 and 151, for the seafloor primary reflection and WBM respectively. The conversion factor calculated from the data of line L18 was 0.000263. A mean of the two values, which is 0.000265, was used for the calculation of reflection coefficients. This compared well with the calculations of Mi (1998), who found a conversion coefficient of 0.000288 for data that was collected earlier during the same survey.

4.3 Results and discussion

The reflection coefficient values for the seafloor, derived from scaling of raw seafloor amplitudes, span a wide range from 0.05 to as high as 0.48. A total of 7578 shot points were used to compute the reflection coefficient values for the seafloor. Most of these values (almost 63%) were between 0.10 and 0.2 and less than 2% had values greater than 0.3 (Figure 4.4a). The reflection coefficients computed from the seismic amplitudes were found to be in close agreement with those observed from

actual physical property measurements (Mi, 1998) for drill cores A07, A08 and A09 (Table 4.1).

Core #	Average seafloor density (from cores)	Seafloor RC from cores	Seafloor RC from seismic amplitudes	Percentage difference
A07	1.676	0.23	0.214	6.9%
A08	1.713	0.24	0.236	1.6%
A09	1.789	0.26	0.244	6.1%

Table 4.1: Comparison of seafloor reflection coefficients computed from seismic amplitudes with those computed from core measurements. For the core measurements, only the density contrast was used in computing the seafloor reflection coefficients. A seawater density of 1.05 gm/cm^3 was assumed.

The reflection coefficients for the BSR had a range from 0.01 to 0.25. A total of 1980 points were used to compute the BSR reflection coefficients. Most of the values (almost 60%) were within 0.03 and 0.12. Only 8% of the values were found to be greater than 0.21 (Figure 4.4b).

The contour maps of Figure 4.5 show the spatial distribution of the seafloor reflection coefficients, superimposed with the seafloor topography. To compensate for the effects of wind and swell, which might have affected the reflection amplitudes in a random fashion along the seismic lines, the reflection coefficients are normalized such that the mean value for each seismic line equals the global mean over the entire region of study. The normalization process is bound to smooth out the long wavelength variations of the reflection coefficients. However, the contour map of Figure 4.5a, which shows the distribution of the seafloor reflection coefficients before normalization, does not reveal any such regional trend - thereby justifying the normalization process.

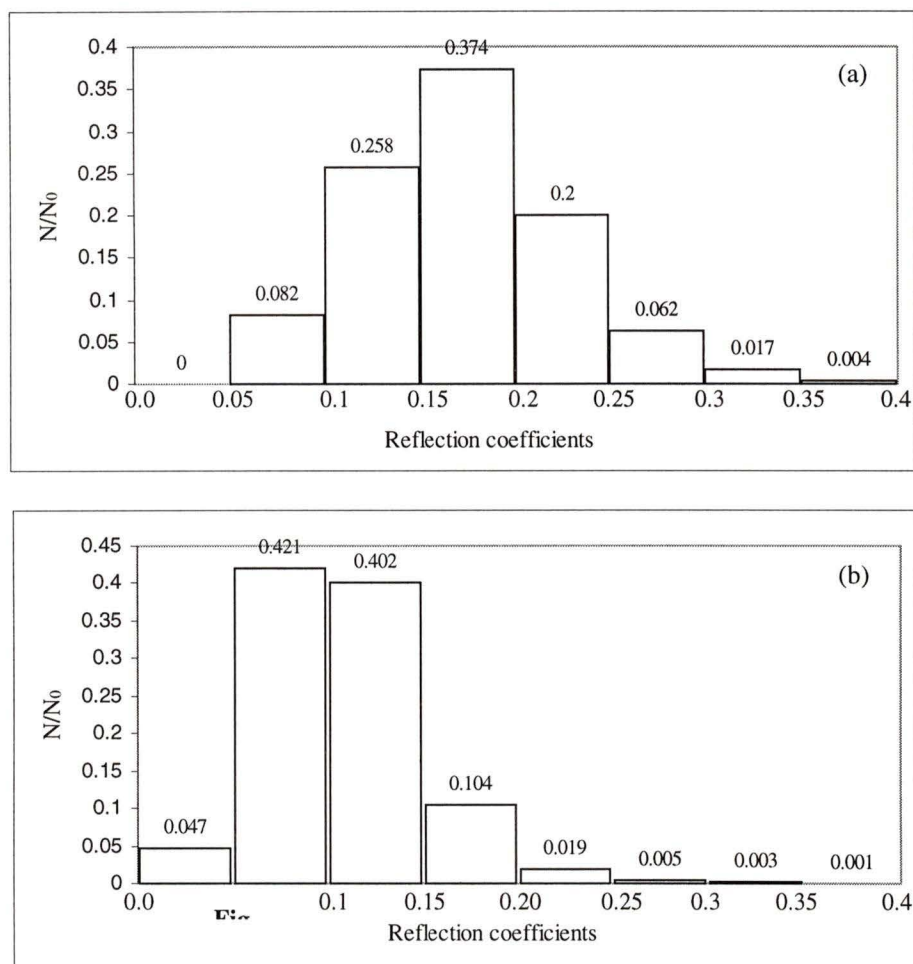


Figure 4.4(a): Distribution of seafloor reflection coefficients. N_0 represents the total number of points used (7578). Most of the values (63%) were between 0.10 and 0.20. Values greater than 0.30 have been ignored in the preparation of the contour maps. **(b):** Distribution of BSR reflection coefficients ($N_0 = 1980$). Most of the values (83%) were between 0.05 and 0.15. Reflection coefficients greater than 0.2 have been ignored in the preparation of the contour maps.

High values for seafloor reflection coefficients were observed at the North East corner of the region, where the water depth is as low as 700 m. High seafloor reflection coefficients were also observed at the south-west corner, over a local topographic high. The contour map suggests that there are coherent signals oriented roughly along the strike of the deformation front. To investigate the physical basis of

this correlation, the reflection coefficient profiles over groups of adjacent seismic lines were examined.

The reflection coefficient profiles for lines L-09, L10 and L-11 are shown in Figure 4.6. High reflection coefficients, which were coherent along the three lines, were observed over a depression at $\sim 126.28^{\circ}\text{W}$ (Figure 4.6). A possible reason for these high values may be focussing effects due to the depression. High values were also observed near the toe of the steeper slope at $\sim 126.22^{\circ}\text{W}$ (Figure 4.6). All three lines indicate roughly the same average values of about 0.2 at shallower depths farther up the slope.

Figure 4.7 shows three adjacent lines (L-16, L-17 and L-18) over more complicated bathymetry. High reflection coefficients (~ 0.3) is consistently observed over parts of the wide depression between 126.25°W and 126.30°W , and also near the trough at about 126.2°W . Again, average patterns of about 0.2 are consistent over the shallower portions of the lines.

In Figure 4.8, there is some evidence of correlation of relatively high reflectivity values at the local high between 128.28°W and 128.32°W . Significant gaps in the data preclude any detailed assessment of the correlation over other parts of these two lines.

In general, although there appears to be some examples of consistency between portions of adjacent seismic lines, the overall correlation with topography or structural features is low. The reflection coefficient variation is also related to changes in the seafloor materials. However, without more ground truth data, it is not possible to examine the correlation with physical properties.

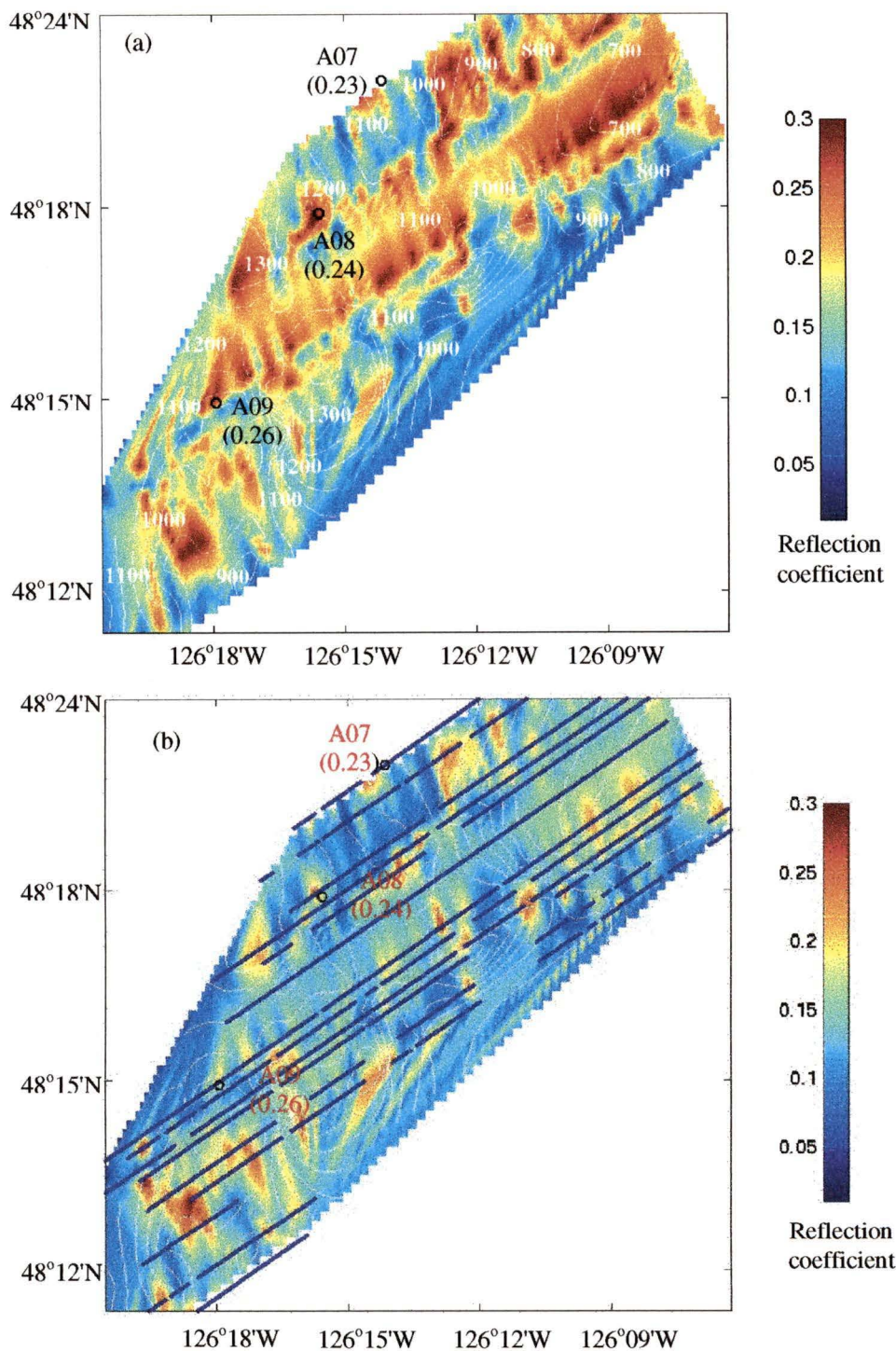


Figure 4.5: Contour maps showing the spatial distribution of seafloor reflection coefficients. The colours represent the reflection coefficients while the contour lines indicate depth of the seafloor. The reflection coefficients have been normalized such that the average value along each line equals the mean of the entire region of study. Figure (a) shows the spatial distribution before normalization while the distribution of the normalized values is shown in the contour map of (b). The seafloor contour values are shown in (a) while in (b) the seafloor seismic amplitude data points are superimposed.

The spatial distribution of the BSR reflection coefficients is shown in Figure 4.9. The reflection coefficients were normalized to compensate for the effects of wind and swell. The overall pattern of the BSR reflection coefficients is quite uniform. However, some anomalous regions of high BSR reflection coefficients were observed at the north-east corner (shallow seafloor topography) and south-west corner (localized topographic high). There seems to be a certain correlation between the BSR reflection coefficient and seafloor topography, which is further substantiated by the reflection coefficient profiles along the seismic line L-22 (Figure 4.10). The correlation, however, is not as strong as that observed by Fink and Spence (1998) over a region farther north. High reflection coefficients were also observed over a channel between two topographic highs (Figure 4.11). This high over the channel may be due to a large sedimentation at this channel. Hydrate dissociates at its base as more sediments are added, and the extra gas either causes a higher velocity contrast due to its lower velocity, or more hydrate is created just above it.

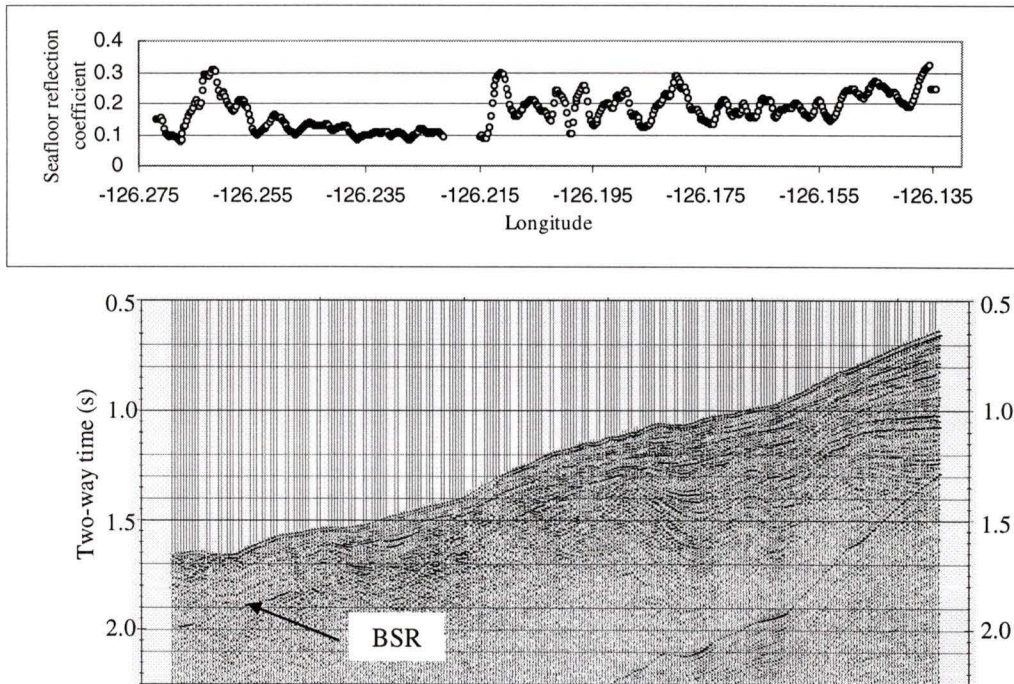


Figure 4.6(a): Reflection coefficient profile across line L-09.

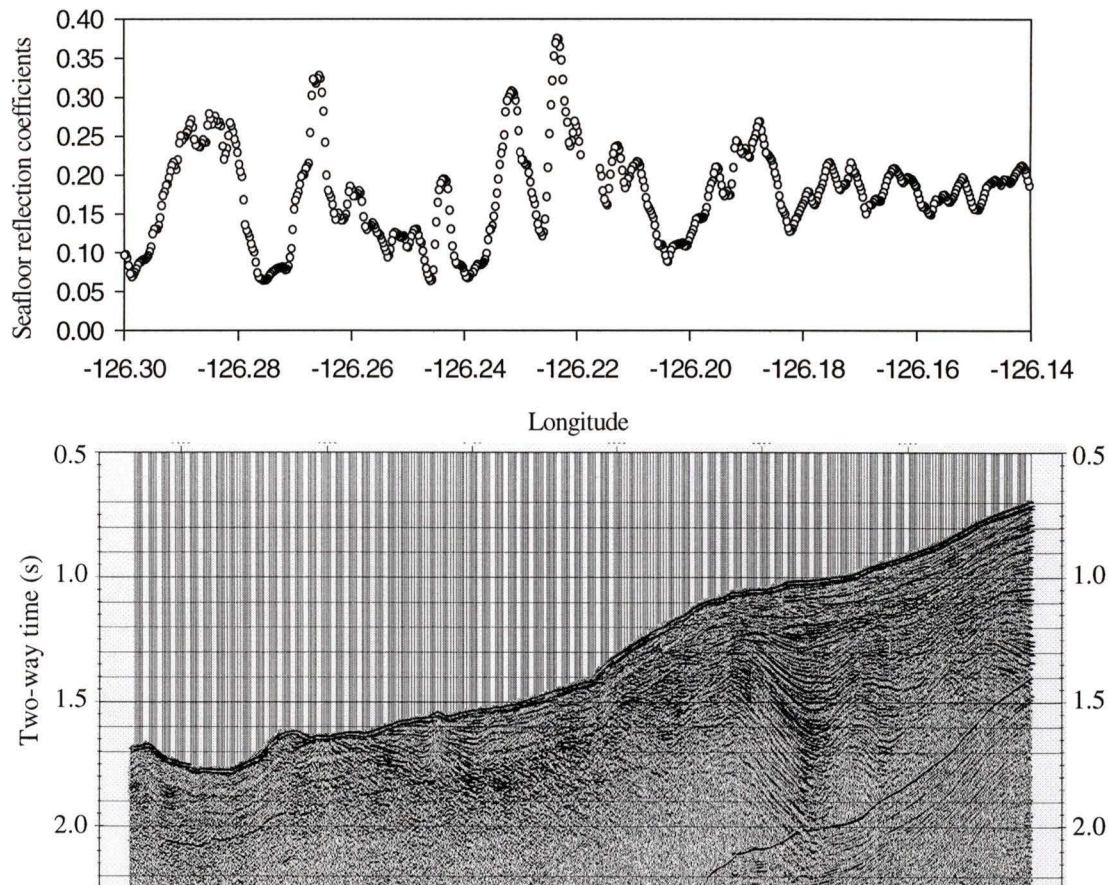


Figure 4.6(b): Reflection coefficient profile across line L-10.

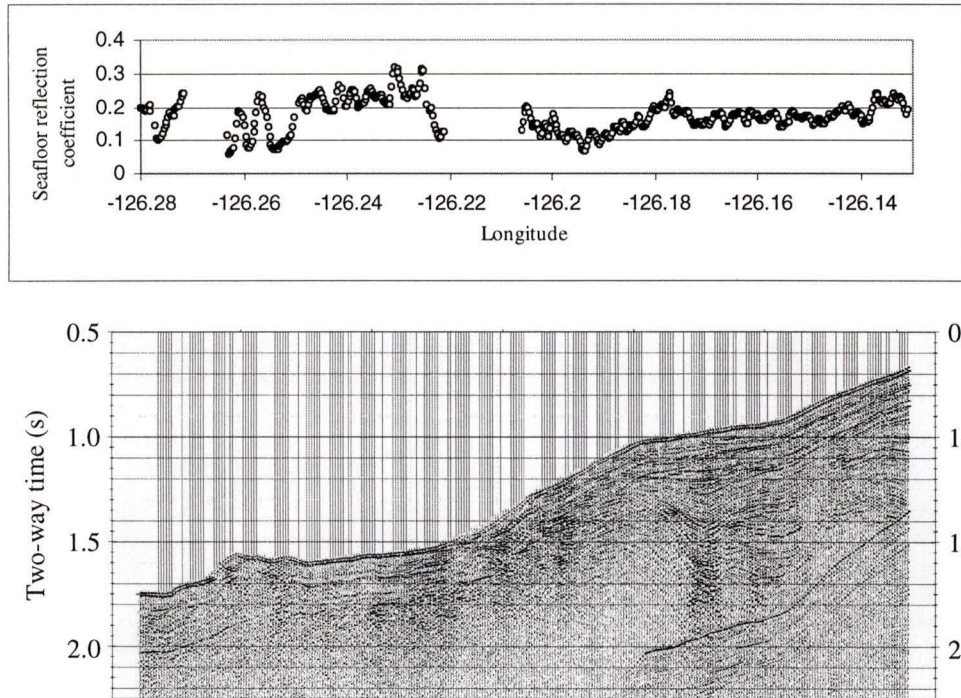


Figure 4.6(c): Reflection coefficient profile across line L-11.

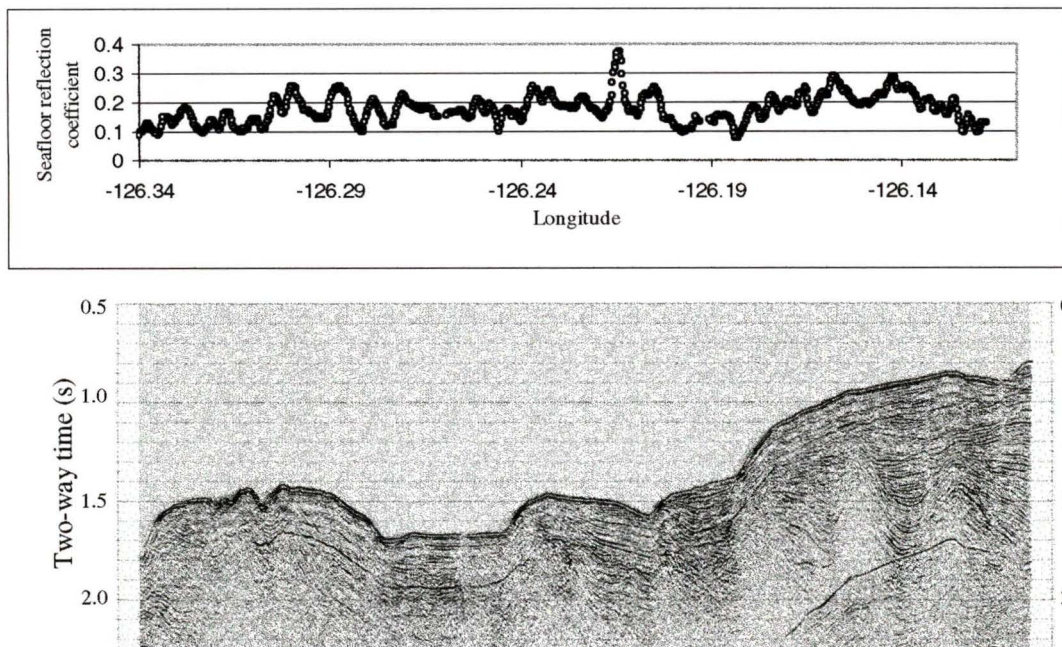


Figure 4.7(a): Reflection coefficient profile across line L-16.

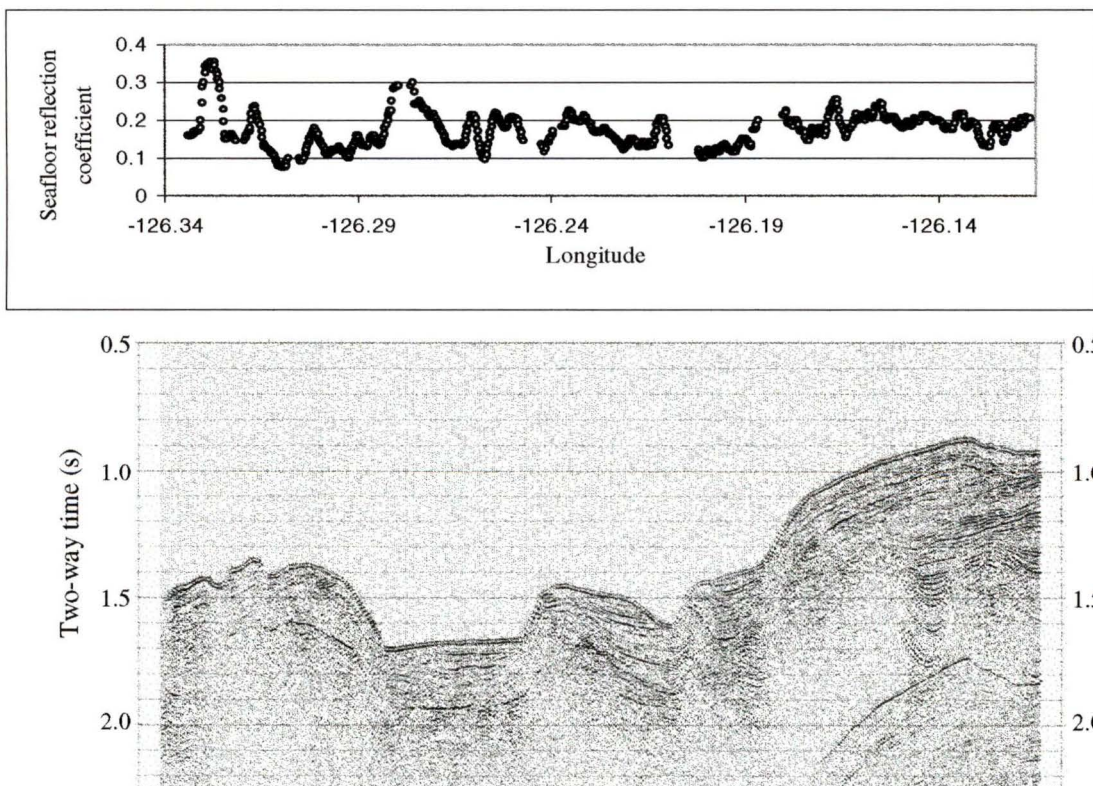


Figure 4.7(b): Reflection coefficient profile across line L-17.

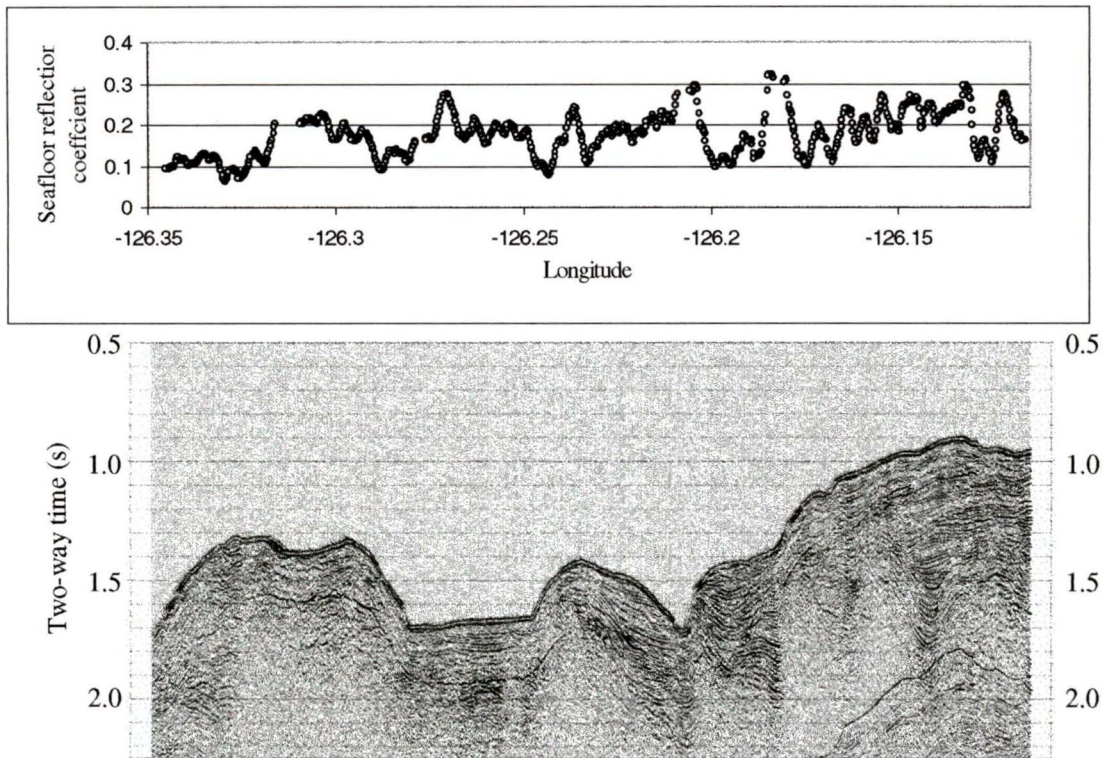


Figure 4.7(c): Reflection coefficient profile across line L-18.

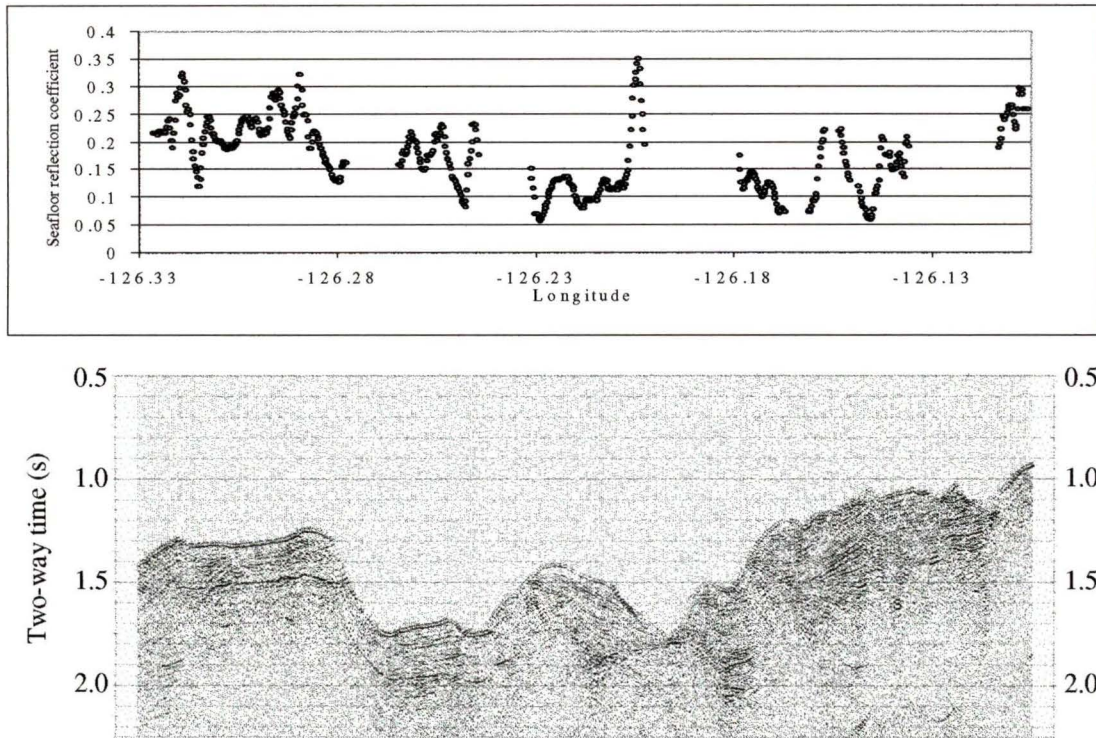


Figure 4.8(a): Reflection coefficient profile across line L-21.

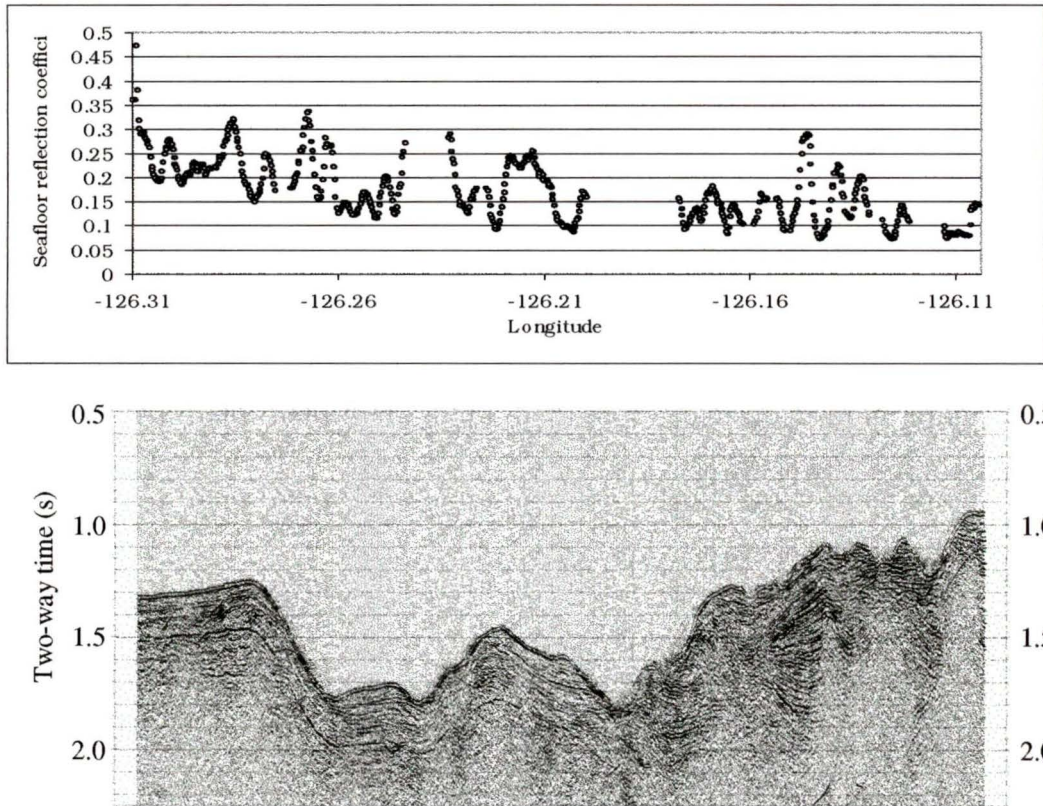


Figure 4.8(b): Reflection coefficient profile across line L-22.

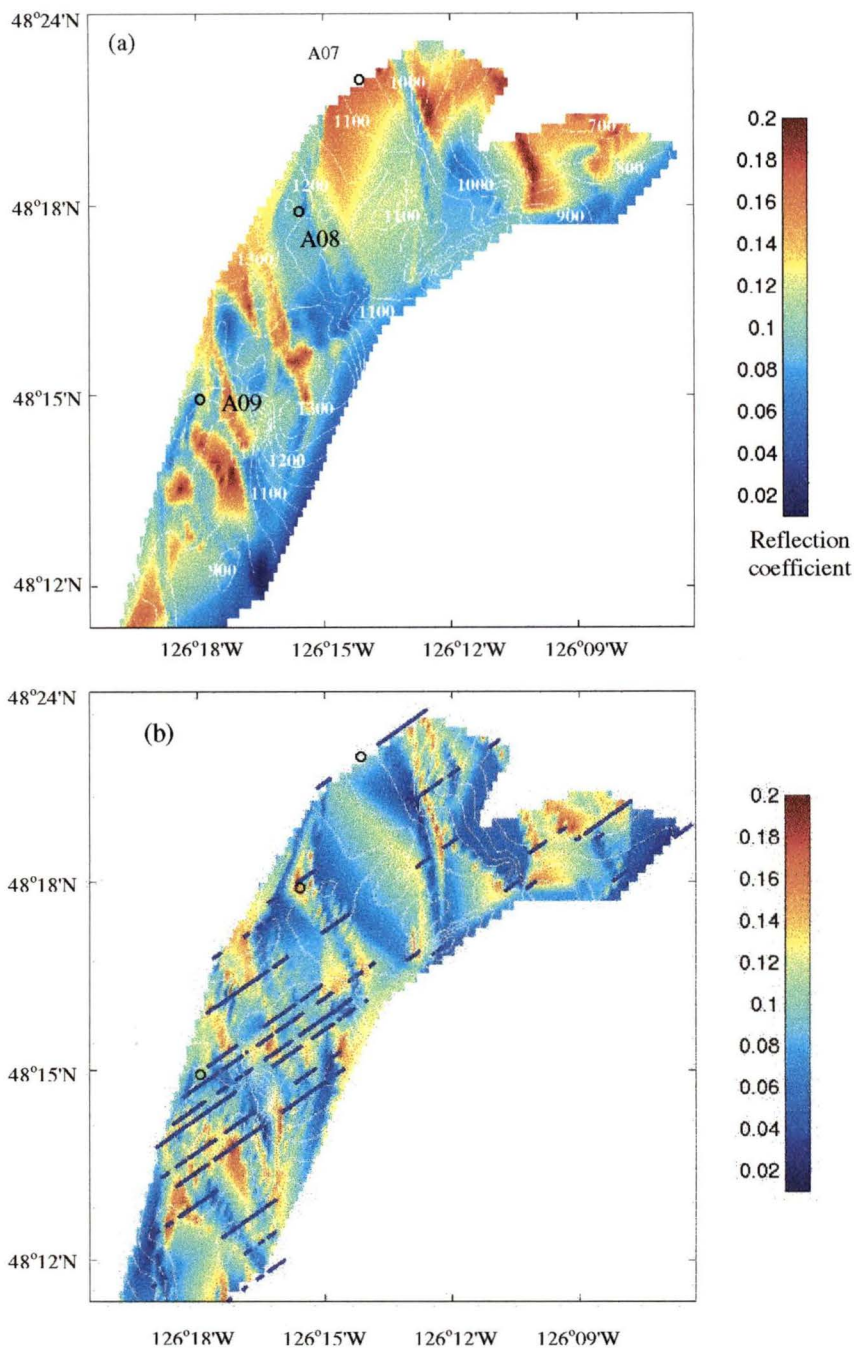


Figure 4.9 Contour maps showing the spatial distribution of BSR reflection coefficients. The colours represent the reflection coefficient while the contour lines indicate depth of the seafloor. The BSR reflection coefficients have been normalized using the same process that was used for normalizing the seafloor reflection coefficients. Figure (a) shows the spatial distribution before normalization while the normalized reflection coefficients are shown in (b). Seafloor contour values are shown in (a) while in (b), the locations of BSR amplitude data points are shown.

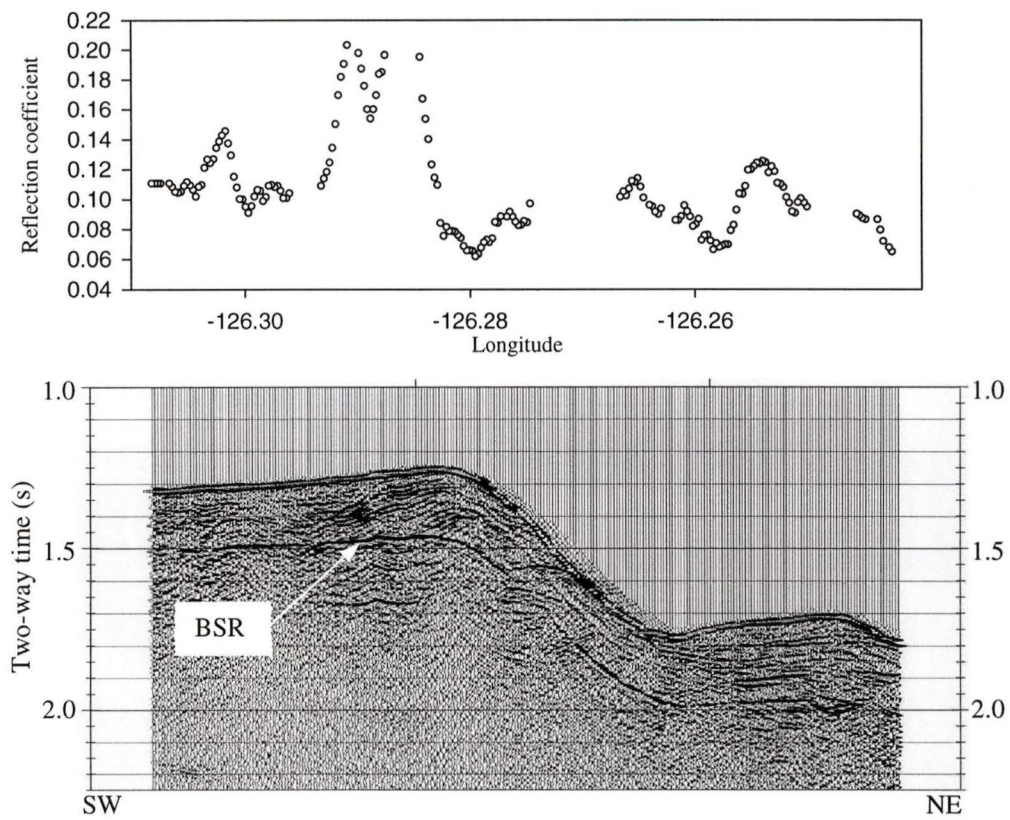


Figure 4.10: BSR reflection coefficients over part of line L-22 showing high reflection coefficients over topographic highs.

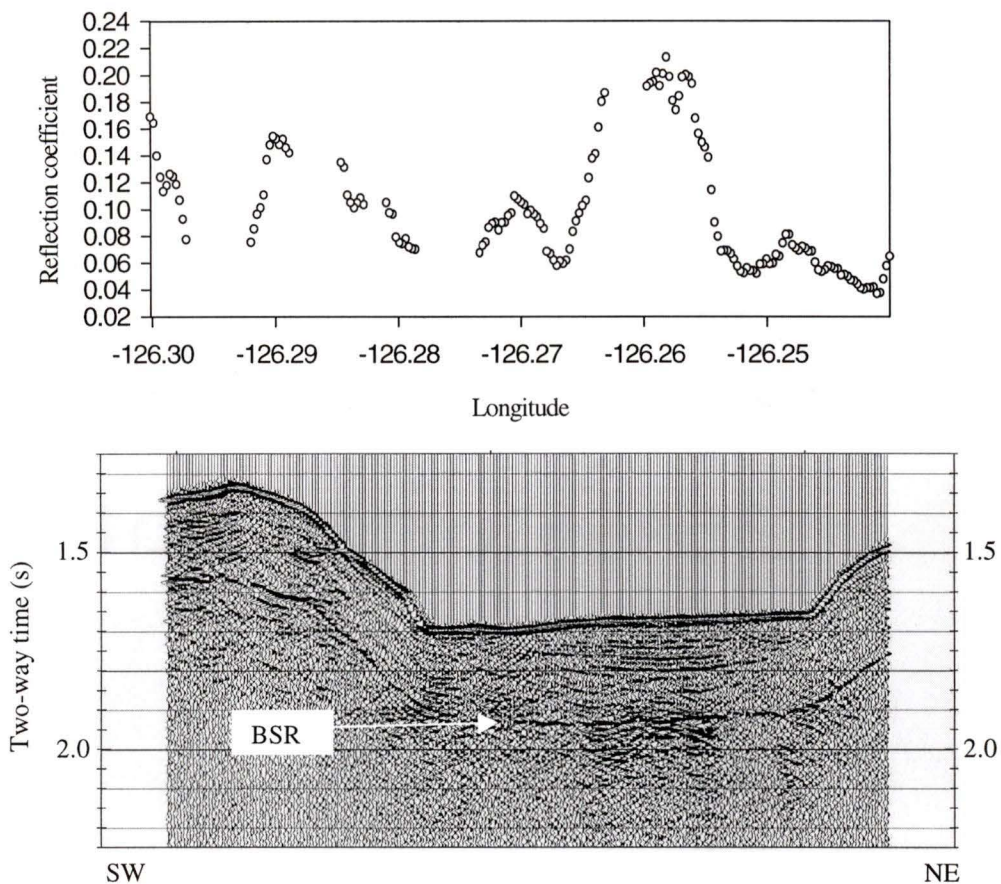


Figure 4.11(a): Reflection coefficients over part of line L-18 showing high values over a channel between two topographic highs. These high reflection coefficients seem coherent with those observed over adjacent seismic line L-17 (Figure 4.11b). High BSR reflection coefficients were also observed over the topographic high on the SW part of the line segment.

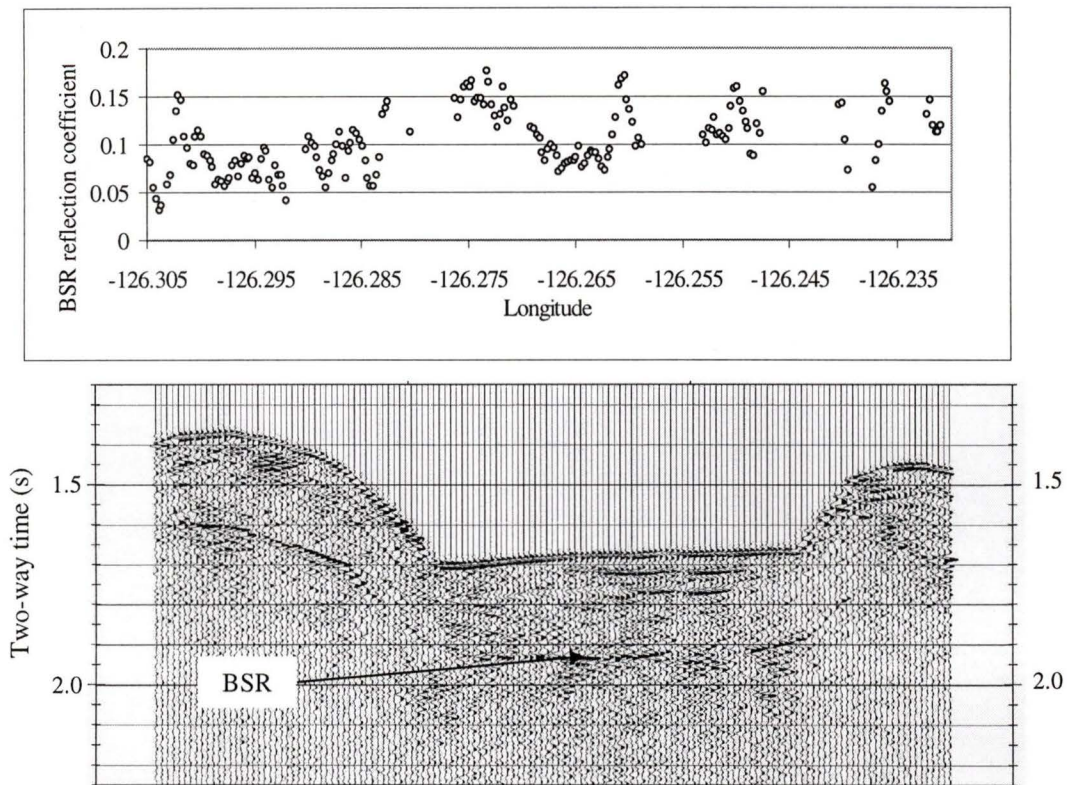


Figure 4.11(b): Reflection coefficients over part of line L-17 showing high values over a channel between two topographic highs. These high reflection coefficients seem coherent with those observed over adjacent seismic line L-18 (Figure 4.11a). High BSR reflection coefficients were also observed over the topographic high on the SW part of the line segment.

CHAPTER 5 CONCLUSIONS

Detailed analysis of multichannel seismic reflection data in an area offshore Vancouver Island, combined with more regional data, has revealed the heat flow pattern of the region. The conclusions from this study can be summarized as follows:

1. The average heat flow value of the 10 km by 20 km region of study was between 70 and 80 mW/m². This is consistent with the estimates from multichannel seismic line 89-03, which are recalculated by assuming a lithostatic density model for consistency with the current study. The average value is slightly higher than the estimates of heat flow from BSR depth computed by Davis et al., (1990) over a region 50 km farther north. However, heat flow values estimated in this study are lower than the heat probe measurements, reported in Davis et al. (1990), which average around 90 mW/m². No explanation was found for this difference.
2. Though there are many second order spatial variations, there is a clear regional trend of heat flow decreasing landward across the margin, from an average of around 80 mW/m², at a distance of 15 km from the deformation front, to an average of around 65 mW/m², at a distance of 40 km from the deformation front. This regional trend reflects the combined effects of the processes of sedimentation in the Cascadia basin, tectonic sediment thickening in the accretionary prism and subduction of the Juan de Fuca plate. This regional

trend is in agreement with the numerical models of Hyndman et al. (1993), which take into account the effects of sediment thickening and fluid expulsion. However, the estimated values of heat flow from BSR depth are found to be slightly higher than those predicted by the regional model of Hyndman et al. (1993).

3. A consistent pattern of high heat flow values over flanks of topographic highs and low heat flow values over the topographic highs themselves was observed. This variation is attributed mostly to the distortion in the thermal gradients caused by the seafloor topography, as suggested by use of the numerical models of Lachenbruch (1968). No strong thermal evidence was found suggesting any significant channelized migration of fluids along thrusts and other hydrologic conduits. However, given the uncertainty in computing the effect of seafloor topography on heat flow, an integrated quantitative analysis, involving channelized fluid flow, topographic distortion and downward movement of cold sediments along faults, is required to get a complete understanding of the local variations of heat flow in the Cascadia margin.

In the second part of the thesis, reflection coefficients of the seafloor and the BSR were examined. Although there appears to be some examples of consistency between reflection coefficient values of adjacent seismic lines, no strong correlation between the seafloor topography and seafloor reflection coefficients, as reported in Fink (1995) and Fink and Spence (1998), was observed. The BSR reflection coefficients seem to have a certain correlation with the seafloor topography, though this correlation is not so strong as observed by Fink and Spence (1998) over an area

farther north. High BSR reflection coefficients were observed over topographic highs and also over a channel between two topographic highs.

BIBLIOGRAPHY

Amestoy, P., Gardner, G.H.F., Larssonneur, J.L., and Leiss, E.L., 1987. Phase-shift based prestack depth migration for laterally varying velocities. *Expanded Abstracts*, 57th Annual International Meeting, Society of Exploration Geophysicists, **87**: S14.7

Ashi, J., and Taira, A., 1993. Thermal structure of the Nankai accretionary prism as inferred from gas hydrate BSR's. In Underwood, M.B. (editor), *Thermal evolution of the Tertiary Shimanto Belt, Southwest Japan: An example of ridge-trench interaction*, **273**: 137 – 149.

Atwater, T., 1970. Implications of plate tectonics for the Cenozoic tectonic evolution of North America. *Geological Society of America Bulletin*, **81**: 3513 – 3536.

Atwater, T., 1989. Plate tectonic history of the northeast Pacific and western North America. In Wineter, E.L., Hussong, D.M., and Decker, R.W. (editors), *The Eastern Pacific Ocean and Hawaii*. Geological Society of America, Geology of North America Ser., N: 21 – 72.

Backus, M.M., 1978. Water reverberations – their nature and elimination. In Webster, G.M. (editor), *Geophysics Reprint Series – Deconvolution*. Society of Exploration Geophysicists. 136 – 164.

Bell, P.R., 1983. Methane hydrate and the carbon dioxide question. In Clark, W.C. (editor), *Carbon dioxide Review*. Oxford University Press, New York, 401 – 406.

Bily, C., and Dick, J.W.L., 1974. Naturally occurring gas hydrates in the Mackenzie Delta. *N.W.T. Bulletin of Canadian Petroleum Geology*, **32**: 340 – 352

Birch, F., 1950. Flow of heat in the Front Range, Colorado, *Bulletin of Geological Society of America*, **61**: 567 – 630.

Birch, F., 1967. Low values of oceanic heat flow, *Journal of Geophysical Research*, **72(8)**: 2261 – 2262.

Blackwell, D.D., 1991. Heat flow in the state of Washington and thermal conditions in the Cascade range. *Journal of Geophysical Research*, **95**: 19495 – 19516.

Bornhold, B.D., and Prior, D.B., 1989. Sediment blocks on the sea floor in British Columbia fjords. *Geo-Marine Letters*, **9**: 135 – 144.

Borowski, W.S., Paull, C.K., and Ussler, W., 1996. Marine pore water sulphate profiles indicate in situ methane flux from underlying gas hydrate. *Geology*, **24(7)**: 655 – 658.

Brooks, J.M., Kennicutt, M.C. II, Fay, R.R., McDonald, T.J., and Sassen, R., 1984. Thermogenic gas hydrates in the Gulf of Mexico, *Science*, **225**: 409 – 411.

Brooks, J.M., Cox, H.B., Bryant, W.R., Kennicutt, M.C. II, Mann, R.G., and MacDonald, T.J., 1985. Association of gas hydrates and oil seepage in the Gulf of Mexico, *Advanced Organic Geochemistry*, **10**: 221 – 234.

Bullard, E.C., 1938. The disturbance of the temperature gradient in the earth's crust by inequalities of height, *Monthly Notices, Royal Astronomical Society, Geophysics Supplement*, **4**: 360 – 362.

Bugge, T., Befring, S., Belderson, R.H., Eidvin, T., Jansen, E., Kenyon, N.H., Holtedahl, H., and Sejrup, H.P., 1987. A giant three-stage submarine slide off Norway. *Geo-Marine Letters*, **7**: 191 – 198.

Carpenter, G., 1981. Coincident sediment slump/clathrate complexes on the U.S. Atlantic continental slope. *Geo-Marine Letters*, **1**: 29 – 32.

Carson, B., Westbrook, G.K., Musgrave, R.J., and Suess, E., 1995. *Proceedings of the Ocean Drilling Program (scientific results)*. College Station, Texas.

Cherskiy, N.V., Tsarev, V.P. and Nikitin, S.P., 1985. Investigation and prediction of conditions of accumulation of gas resources in gas hydrate pools. *Petroleum Geology*, **21**: 65 – 89.

Clowes, R.M., Brandon, M.T., Green, A.G., Yorath, C.J., Sutherland Brown, A., Kanasewich, E.R., and Spencer, C., 1987a. Lithoprobe – Southern Vancouver Island: Cenozoic subduction complex imaged by deep seismic reflections. *Canadian Journal of Earth Sciences*, **24**: 31 –51.

Clowes, R.M., Yorath, C.J., and Hyndman, R.D., 1987b. Reflection mapping across the convergent margin of western Canada. *Geophysical Journal of Royal Astronomical Society*, **89**: 79 – 84.

Clowes, R.M., Hyndman, R.D., Yorath, C.J., and Davis, E.E., 1990. The northern Cascadia subduction zone at Vancouver Island: Seismic structure and tectonic history. *Journal of Geophysical Research*, **93**: 13,391 – 13,405.

Collet, T.S., Kvenvolden, K.A., and Magoon, L.B., 1990. Characterization of hydrocarbon gas within the stratigraphic interval of gas hydrate stability on the north slope of Alaska, U.S.A. *Applied Geochemistry*, **5**: 279 – 287.

Crosson, R.S., and Owens, T.J., 1987. Slab geometry of the Cascadia subduction zone beneath Washington from earthquake hypocentres and teleseismic converted waves. *Geophysical Research Letters*, **14**: 824 – 827.

Davidson, D.W., El-Defrawy, M.K., Fulgem, M.O., and Judge, A.S., 1978. Natural gas hydrates in northern Canada. In *Third International Conference on Permafrost*, National Research Council of Canada, Ottawa, Canada. **1**: 938 – 943.

Davis, E.E., and Seemann, D.A., 1981. A compilation of seismic reflection profiles across the Juan de Fuca Ridge: ridge-crest migration over a heterogeneous asthenosphere, *Earth and Planetary Science Letters*, **79**: 385 – 396.

Davis, E.E., Curie, R.G., Sawyer, B.S., and Kosalos, J.G., 1986. The use of swath bathymetric and acoustic image mapping tools in marine geoscience. *Marine Technology Society Journal*, **20**: 17 – 27.

Davis, E.E., and Hyndman, R.D., 1989. Accretion and recent deformation of sediments along the northern Cascadia subduction zone. *Geological Society of America Bulletin*, **101**: 1465 – 1480.

Davis, E.E., Hyndman, R.D., and Villinger, H., 1990. Rates of fluid expulsion across the northern Cascadia accretionary prism: constraints from new heat flow and multichannel seismic reflection data. *Journal of Geophysical Research*, **95**: 8869 – 8889.

Davy, H., 1811. On some of the combinations of oxy-muratic gas and oxygen, and on the chemical relations of the principles to inflammable bodies. *Philosophical Transactions of the Royal Society of London*, **101**(1).

Dickens, G.R., and Quinby-Hunt, M.S., 1994. Methane hydrate stability in sea water, *Geophysical Research Letters*, **21**: 2115 – 2118.

Ellis, R.M. et al., 1983. The Vancouver Island seismic project: a COCRUST onshore-offshore study of the convergent margin. *Canadian Journal of Earth Sciences*, **20**: 719 – 741.

Engebretson, D.C., Cox, A., and Thompson, G.A., 1984. Correlation of plate motions with continental tectonics. *Tectonics*, **3**: 115 – 120.

Engebretson, D.C., Cox, A., and Gordon, R.G., 1985. Relative motions between oceanic and continental plates in the Pacific basin. Special paper, *Geological Society of America*, 206.

Englezos, P., and Bishnoi, P.R., 1988. Prediction of gas hydrate formation in aqueous solutions, *American Institute of Chemical Engineers*, **34**: 1718 – 1721.

Fink, C.R., 1995. Methane distribution offshore Vancouver Island from detailed single channel seismic studies. *Master's thesis*, University of Victoria.

Fink, C.R., and Spence, G.D., 1998. Hydrate distribution off Vancouver Island from multi-frequency single channel seismic reflection data. Submitted to the *Journal of Geophysical Research*.

Fisher, A.T., and Hounslow, M.W., 1990. Transient fluid flow through the toe of the Barbados accretionary complex: constraints from ODP Leg 110 heat flow studies and simple models, *Journal of Geophysical Research*, **95**: 8845 – 8858.

Ginsburg, G.D., Guseynov, R.A., Dadashev, A.A., Ivanov, G.A., Kazantsev, S.A., Soloviev, V.A., Telepnev, E.V., Askeri-Nasirov, R. Y., Yesikov, A.D., Maltseva, V.I.,

Mashirov, Y.G., and Shabayeva, I.Y., 1992. Gas hydrates of the southern Caspian. *International Geological Review*, **34**: 765 – 782.

Gornitz, V., and Fung, I., 1994. Potential distribution of methane gas hydrates in the world's oceans, *Global Biogeochemical Cycles*, **8(3)**: 335 - 347.

Green, A.G., Clowes, R.M., Yorath, C.J., Spencer, C., Kanasewich, E.R., Brandon, M.T., and Sutherland Brown, A., 1986. Seismic reflection imaging of the subducting Juan de Fuca plate. *Nature*, **319**: 210 – 213.

Griffiths, L.J., Smolka, F.R., and Trembly, L.D., 1978. Adaptive deconvolution – a new technique for processing time varying seismic data. *Geophysics*, **42(4)**: 742 – 759.

Hannay, D.E., 1995. Analysis of geoacoustic shot run data from the Pacific shelf experiment, *DREP contractor report*, JASCO Research Ltd., Sidney, B.C., Canada.

Holder, G.D., Kamath, V.A., and Godbole, S.P., 1984. The potential of natural gas hydrates as energy resource. *Review of Energy*, 9: 427 – 455.

Hitchon, B., 1974. Occurrence of natural gas hydrates in sedimentary basins. In Kaplan, I.R. (*editor*), *Natural gases in marine sediments*, Plenum Press, New York. 195 - 225.

Hobro, J.W.D., Minshull, T.A., and Singh, S.C., 1998. Tomographic seismic studies of the methane gas hydrate stability zone in the Cascadia margin, in Henriot, J-P and Mienert, J. (editors), *Gas Hydrates*. Geological Society of London, Special Publications, 137: 133 - 140.

Holder, G.D., Kamath, V.A., and Godbole, S.P., 1984. The potential of natural gas as an energy resource, *Annual Review of Energy*, **9**: 427 – 445.

Hyndman, R.D., 1983. Geothermal heat flux, Juan de Fuca plate map, *Juan de Fuca Plate Map series*, Pacific Geoscience Centre, Geological Survey of Canada.

Hyndman, R.D., 1988. Dipping reflectors, electrically conductive zones and free water beneath a subduction zone. *Journal of Geophysical Research*, **93**: 13,391 – 13,405.

Hyndman, R.D., Yorath, C.J., Clowes, R.M., and Davis, E.E., 1990. The northern Cascadia subduction zone at Vancouver Island; Seismic structure and tectonic history, *Canadian Journal of Earth Sciences*, **27**: 313 – 329.

Hyndman, R.D., and Davis, E.E., 1992. A mechanism for the formation of methane hydrate and seafloor bottom simulating reflectors by vertical fluid expulsion. *Journal of Geophysical Research*, **97**: 7025 – 7041.

Hyndman, R.D., and Spence, G.D., 1992. A seismic study of methane hydrate marine bottom simulating reflector. *Journal of Geophysical Research*, **97**: 6683 – 6698.

Hyndman, R.D., and Hamilton, T.S., 1993. Queen Charlotte area Cenozoic tectonics and volcanism and their association with relative plate motions along the northeastern Pacific margin. *Journal of Geophysical Research*, **98**: 14,257 – 14,277.

Hyndman, R.D., and Wang, K., 1993. Thermal constraints on the zone of major thrust earthquake failure: the Cascadia subduction zone. *Journal of Geophysical Research*, **98**: 2039 – 2060.

Hyndman, R.D., Wang, K., Yuan, T., and Spence, G.D., 1993. Tectonic sediment thickening, fluid expulsion and the thermal regime of subduction zone accretionary

prisms: the Cascadia margin off Vancouver Island. *Journal of Geophysical Research*, **98**: 21,865 – 21,876.

Hyndman, R.D., Spence, G.D., Yuan, T., and Davis, E.E., 1994. Regional geophysics and structural framework of the Vancouver Island margin accretionary prism. In Westbrook, G.K., Carson, B., and Musgrave, R.J. (editors), *Proceedings of the Ocean Drilling Program, initial reports*, **146(1)**: 399 – 419.

Jaeger, J.C., 1965. Application of the theory of heat conduction to geothermal measurements, in Lee, W.H.K. (editor), *Terrestrial heat flow, Geophysical Monograph*, **8**: 7 – 23.

Jaeger, J.C., and Sass, J.H., 1963. Lee's topographic correction in heat flow and the geothermal flux in Tasmania, *Geofis., Pura Appl.*, **54**: 53 – 63.

Jansen, E.S., Befring, T., Bugge, T., Eidvin, T., and Sejrup, H.P., 1987. Large submarine slides on the Norwegian continental margin: sediments, transport and timing. *Marine Geology*, **78**: 77 – 107.

Jeffreys, H., 1938. The disturbance of the temperature gradient in the earth's crust by inequalities of height, *Monthly Notices, Royal Astronomical Society, Geophysics Supplement*, **4**: 309 – 312.

Jovanovich, D.B., Summer, R.D., and Akins-Easterlin, S.L., 1983. Ghosting and marine signature deconvolution – a prerequisite for detailed seismic interpretation. *Geophysics*, **48(11)**: 1468 – 1485.

Judge, A.S., 1982. Natural gas hydrates in Canada. In French M.H.(editor), *Proceedings of the 4th Canadian Permafrost Conference, 1981*, Roger J.E. Brown Memorial volume, Ottawa, Canada, 320 – 328.

Kayen, R.E., and Lee, H.J., 1991. Pliocene slope instability of gas hydrate laden sediment on the Beaufort Sea margin. *Marine Geotechnology*, **10**: 125 – 141.

Kurtz, R.D., Delaurier, J.M., and Gupta, J.C., 1986. A magnetotelluric sounding across Vancouver Island detects the subducting Juan de Fuca plate. *Nature (London)*, **321**: 596 – 599.

Kvenvolden, K.A., and McMennamin, M.A., 1980. Hydrates of natural gas: a review of their geological occurrence.

Kvenvolden, K.A., 1982. Occurrence and origin of methane gas hydrates. In French M.H. (editor), *Proceedings of the 4th Canadian Permafrost Conference, 1981*, Roger J.E. Brown Memorial volume, Ottawa, Canada, 305 – 311.

Kvenvolden, K.A., and Barnard, L.A., 1983. Hydrates of natural gas in continental margins. *American Association of Petroleum Geologists Memoir*, **34**: 631 – 640.

Kvenvolden, K.A., and McDonald, T.J., 1985. Gas hydrate of Middle America Trench - DSDP Leg 84, In von Huene, R. et al., (editors), Initial reports : Deep Sea Drilling Project, **84**: 667 - 682.

Kvenvolden, K.A., 1988. Methane hydrate - a major reservoir of carbon in the shallow geosphere ? *Chemical Geology*, **71**: 41 - 51.

Kvenvolden, K.A., and Grantz, A., 1990. Gas hydrates of the arctic ocean region. In Grantz, A., Johnson, L., and Sweeney, J.F. (editors), *Geology of North America; The Arctic Ocean Region*, Geological Society of America, Boulder, Colorado. **50**: 539 – 549.

Kvenvolden, K.A., Ginsburg, G.D., and Soloviev, V.A., 1993. Worldwide distribution of sub-aquatic gas hydrates. *Geo-Marine Letters*, **13**: 32 – 40.

Kvenvolden, K.A., 1993. Gas hydrate – geological perspective and global change. *Review of Geophysics*, **31**: 173 – 187.

Kvenvolden, K.A., 1994. Natural gas hydrate occurrence and issues. In Sloan, E.D. Jr., Happel, J., Hnatow, A. (editors), *International Conference on Natural Gas Hydrates*, Annals of the New York Academy of Sciences, **715**: 232 – 246.

Lachenburch, A.H., 1968. Rapid estimation of the topographic disturbance to superficial thermal gradients, *Review of Geophysics*, **6**: 365 – 400.

Lewis, T.J., Bentkowski, W.H., Davis, E.E., Hyndman, R.D., Souther, J.G., and Wright, J.A., 1988. Subduction of the Juan de Fuca plate: Thermal consequences. *Journal of Geophysical Research*, **93**: 15,207 – 15,225.

Lewis, T.J., Bentkowski, W.H., and Hyndman, R.D., 1991. Crustal temperature near the LITHOPROBE Southern Cordilleran Transect. *Canadian Journal of Earth Sciences*, **29**: 1197 – 1214

MacDonald, G.T., 1983. The many origins of natural gas. *Journal of Petroleum Geology*, **5**: 341 - 362.

MacDonald, G.T., 1990. The future of methane as an energy resource, *Annual Review of Energy*, **15**: 53 - 83.

Mackay, M.E., Jarrard, R.D., Westbrook, G.K., Hyndman, R.D., and the Shipboard Scientific Party of ODP Leg 146, 1994. Origin of the bottom simulating reflectors: geophysical evidence from the Cascadia accretionary prism. *Geology*, **22**: 459 – 462.

Makogon, Y.F., Trebin, F.A., Tofimuk, A.A., Tsarev, V.P., and Cherskiy, N.V., 1972. Detection of a pool of natural gas in a solid (hydrated gas) state. *Doklady Academy of Science, Earth Science Section*, **196**: 197 – 200.

Makogon, Y.F., 1974. *Hydrates of natural gas*, Nedra, Moscow, Russia.

Makogon, Y.F., 1995. Principles and experience of the development of gas hydrate deposits. In Sloan, E.D., (*editor*), Proceedings on a conference on drilling hydrates in offshore Japan. 280 – 297.

Markl, R.G., Bryan, G.M., and Ewing, J.I., 1970. Structure of the Blake – Bahama Outer Ridge. *Journal of Geophysical Research*, **75**: 4539 – 4555.

McIver, R.D., 1977. Hydrates of natural gas – important agent in geological processes. Abstracts with programs: *Geological Society of America*, **9**: 1089 – 1090.

McIver, R.D., 1982. Role of naturally occurring gas hydrates in sediment transport. *American Association of Petroleum Geologists Bulletin*, **66**: 789 – 792.

Mi, Y., 1998. Seafloor sediment coring and multichannel seismic studies of gas hydrate, offshore Vancouver Island, *M.Sc. thesis, University of Victoria*.

Minshull, T., and White, R., 1989. Sediment compaction and fluid migration in the Makran accretionary prism, *Journal of Geophysical Research*, **89**: 11,549 – 11,559.

Minshull, T., Singh, S.C., and Westbrook, G.K., 1994. Seismic velocity structure at a gas hydrate reflector offshore western Colombia, from full waveform inversion. *Journal of Geophysical Research*, **99**: 4715 – 4734.

Neave, K.G., Judge, A.S., Hunter, J.A., and MacAulay, H.A., 1978. Offshore permafrost distribution in the Beaufort Sea as determined from temperature and seismic observations. In *Geological Survey of Canada, Current Research, Part C, Paper 78-1C*. 13 –78.

Nisbet, E.G., 1990. The end of the ice age. *Canadian Journal of Earth Sciences*, **27**: 148 –157.

Parsons, B. and Sclater, J.G., 1977. An analysis of the variation of ocean floor bathymetry and heat flow with age. *Journal of Geophysical Research*, **32**: 803 – 827.

Paull, C.K., Ussler, W III, and Borowski, W.S., 1994. Sources of biogenic methane to from marine gas hydrates: In situ production or upward migration? *New York Academy of Science Annals*, 392 – 409.

Pearson, C.F., Murphy, J., and Hermes, R., 1986. Acoustic and resistivity measurements on rock samples containing hydrates: laboratory analogues to natural hydrate deposits. *Journal of Geophysical Research*, **91**: 14,132 – 14,138.

Pflueger, J., 1972. Spectra of water reverberations for primary and multiple reflections. *Geophysics*, **37(5)**: 788 – 796.

Potential Gas Committee, 1981. Potential supply of natural gas in the United States (as of December, 1990). *Technical report, Potential Gas Agency*, Colorado School of Mines, Golden, Colorado.

Reed, D.L., Silver, E.A., Tagudin, J.E., Shipley, T.H., and Vrolijk, P., 1990. Relations between mud volcanoes, thrust deformation, slope sedimentation and gas hydrate, offshore North Panama. *Marine Petroleum Geology*, **7**: 44 – 54.

- Riddihough, R.P., 1979. Structure and gravity of an active margin – British Columbia and Washington. *Canadian Journal of Earth Sciences*, **16**: 350 – 363.
- Riddihough, R.P., 1984. Recent movements of the Juan de Fuca plate system. *Journal of Geophysical Research*, **89**: 6980 – 6994.
- Robinson, E.A. and Treitel, S., 1980. *Geophysical Signal Analysis*. Prentice Hall Inc.
- Rogers, G.C., 1983. Some comments on the seismicity of the northern Puget Sound – southern Vancouver island region. *Open file report – U.S. Geological Survey*, **83-19**: 19 –39.
- Shine, K.P., Derwent, R.G., Wuebbles, D.J., and Morcrette, J-J., 1990. In Houghton, J.T., Jenkins, G.J., and Ephramus, J.J. (editors), *Climate change, The IPCC Scientific Assessment*. Cambridge University Press, Cambridge. 1 – 40
- Shiple, T.H., Houston, M.H., Buffler, R.T., Shaub, K.J., McMillen, J.W., and Warzel, J.L., 1979. Seismic reflection evidence for the widespread occurrence of possible gas hydrate horizons on continental slopes and rises. *American Association of Petroleum Geologists Bulletin*, **63**: 2204 – 2213.
- Shouldice, D.H., 1971. Geology of the western Canada continental shelf. *Bulletin of Canadian Petroleum Geology*, **19**: 405 – 436.
- Singh, S.C., and Minshull, T.A., 1994. Velocity structure of a gas hydrate reflector at Ocean Drilling Program site 889 from global seismic waveform inversion. *Journal of Geophysical Research*, **99**: 204 – 207.
- Sinton, J.B., Ward, R.W., and Watkins, J.S., 1978. Suppression of long delay multiple reflections by predictive deconvolution. *Geophysics*, **43(7)**: 1352 – 1367.

Sloan, E.D., 1990. *Clathrate hydrates of natural gas*. Marcel Dekker, New York edition.

Spence, G.D., Minshull, T.A., and Fink, C., 1995. Seismic structure of methane gas hydrate, offshore Vancouver Island, in Carson, B., Westbrook, G.K., Musgrave, R.J., and Suess, E. (editors), *Proceedings of the Ocean Drilling Program, Scientific Results*, **146**, College Station, Texas, 163 – 174.

Spence, G.D., Clowes, R.M., and Ellis, R.M., 1985. Seismic structure across the active subduction zone of western Canada. *Journal of Geophysical Research*, **90**: 6745 – 6772.

Spence, G.D., Hyndman, R.D., Langton, S.G., Davis, E.E., and Yorath, C.J., 1991a. Multichannel seismic reflection profiles across the Vancouver Island continental shelf and slope. Technical report. *Open file report, Geological Survey Of Canada*.

Spence, G.D., Hyndman, R.D., Davis, E.E., and Yorath, C.J., 1991b. Seismic structure of the northern Cascadia accretionary prism: evidence from new multichannel seismic reflection data. In Meissner, R., et al., (editors) *Continental Lithosphere, Deep Seismic Reflections*. American Geophysical Union, Washington, D.C. volume 22 of Geodynamic Series. 257 – 263.

Stock, J.M, and Molnar, P., 1988. Uncertainties and implications of the late Cretaceous and Tertiary positions of North America relative to the Farallon, Kula and Pacific plates. *Tectonics*, **6**: 1339 – 1384.

Stoll, R.D., Ewing, J.I., and Bryan, G.M., 1971. Anomalous wave velocities in sediments containing gas hydrates. *Journal of Geophysical Research*, **76**: 2090 – 2094.

Summerhayes, C.P., Bornhold, B.D., and Embley, R.W., 1979. Surficial slides and slumps on the continental slope and rise of south west Africa: a reconnaissance study. *Marine Geology*, **31**: 265 – 277.

Sutherland Brown, A., and Yorath, C.J., 1985. LITHOPROBE profile across southern Vancouver Island: Geology and tectonics, trip 8. In *Field guides to geology and mineral deposits in the southern Canadian Cordillera*, Geological Society of America – Cordilleran Section Meeting. **8**: 1 –23.

Townend, J., 1997. Estimates of conductive heat flow through bottom simulating reflectors on the Hikurangi and southwest Fiordland continental margins, New Zealand, *Marine Geology*, **141**: 209 – 220.

Trehu, A.M., Lin, G., Maxwell, E., and Goldfinger, C., 1995. A seismic reflection profile across the Cascadia subduction zone offshore central Oregon: New constraints on methane distribution and crustal structure. *Journal of Geophysical Research*, **100**: 15,101 - 15,116.

Tucholke, B.E., Bryan, G.M., and Ewing, J.I., 1977. Gas hydrate horizons detected in seismic-profiler data from the western North Atlantic. *American Association of Petroleum Geologists Bulletin*, **61**: 698 – 707.

Waldron, D.A., Clowes, R.M., and White, D.J., 1990. Seismic structure of a subducting oceanic plate off western Canada. In Green, A.G.(editor), *Studies of laterally heterogeneous structures using seismic refraction and reflection data*, *Geological Survey of Canada*, paper 89-13: 105 – 113.

Wang, K., Hyndman, R.D., and Davis, E.E., 1993. Thermal effects of sediment thickening and fluid expulsion in accretionary prisms: model and parameter analysis, *Journal of Geophysical Research*, **98**: 9975 – 9984.

Wang, X., and Clowes, R.M., 1995. Seismic structure across the Cascadia subduction zone off Vancouver Island: new evidence from seismic refraction and wide angle reflection data. In *Final Program and Abstracts, Geological Society of Canada/Mineralogical Association of Canada Annual Meeting*. Victoria, B.C.

Warner, M., 1990. Absolute reflection coefficients from deep seismic reflections, *Tectonophysics*, **173**: 15 –23.

Watson, R.T., Rodke, H., Oeshger, H., and Siegenthaler, U., 1990. Greenhouse gases and aerosols. In Houghton, J.T., Jenkins, G.J., and Ephramus, J.J. (*editors*), *Climate change, The IPCC Scientific Assessment*, Cambridge University Press, Cambridge, England. 1 – 40.

Weaver, J.S., and Stewart, J.M., 1982. In situ hydrates under the Beaufort Sea shelf. In French M.H.(*editor*), *Proceedings of the 4th Canadian Permafrost Conference, 1981*, Roger J.E. Brown Memorial volume, Ottawa, Canada, 312 – 319.

Wells, R.E., Engebretson, D.C., Snively, P.D., and Coe, R.S., 1984. Cenozoic plate motion and the volcano-tectonic evolution of western Oregon and Washington. *Tectonics*, **3**: 275 – 294.

Westbrook, G.K., Carson, B., and Musgrave, R.J., et al., 1994. *Proceedings of the Ocean Drilling Programs (ODP) – Initial reports*. Volume 146.

Yamano, M., Uyeda, S., Aoki, Y., and Shipley, T.H., 1982. Estimates of heat flow derived from gas hydrates, *Geology*, **10**: 339 – 343.

Yilmaz, O., 1987. *Seismic data processing*. Society of Exploration Geophysicists, Tulsa, Oklahoma.

Yorath, C.J., Green, A.G., Clowes, R.M., Sutherland Brown, A., Brandon, M.T., Kanasewich, E.R., Hyndman, R.D., and Spencer, C., 1985. LITHOPROBE phase I, southern Vancouver Island: Seismic reflection sees through Wrangellia to the Juan de Fuca plate. *Geology*, **13**: 759 – 762.

Yorath, C.J., Clowes, R.M., MacDonald, R.D., Spencer, C., Davis, E.E., Hyndman, R.D., Rohr, K., Sweeney, J.F., Currie, R.G., Halpenny, J.F., and Seeman, D.A., 1987. Marine multichannel seismic reflection, gravity and magnetic profiles – Vancouver Island continental margin and Juan de Fuca ridge. *Open file report*, Geological Survey of Canada.

Yuan T., Spence, G.D., and Hyndman, R.D., 1994. Seismic velocities and inferred porosities in the accretionary wedge sediments at the Cascadia margin. *Journal of Geophysical Research*, **99**: 4413 – 4427

Yuan, T., Hyndman, R.D., Spence, G.D., and Desmons, B., 1996. Seismic velocity increase and deep-sea gas hydrate concentration above a bottom simulating reflector on the northern Cascadia margin. *Journal of Geophysical Research*, **101**: 13,655 – 13,671

Zwart, G., Moore, J.C., and Cochrane, G.R., 1995. Variations in temperature gradients identify active faults in the Oregon accretionary prism. *Earth and Planetary Science Letters*, **139**: 485 – 495.

Vita

Surname: Ganguly

Given name: Nilanjan

Place of Birth: Calcutta, Republic of India.

Educational Institutions Attended:

University of Victoria 1996 to 1998

Indian Institute of Technology 1991 to 1996

Degrees Awarded:

B.Sc. in Geological Sciences, 1994 Indian Institute of Technology

M.Sc. in Exploration Geophysics, 1996 Indian Institute of Technology

Honours and Awards:

University of Victoria Graduate Fellowship, 1997-98

Canadian Society of Exploration Geophysicists Trust Fund scholarship, 1997.

University of Victoria Graduate Fellowship, 1996-97.

Publications:

S.K. Singh, S.K. Nath, N. Ganguly, S.Chakraborty and S. Sengupta., 1997. Cross-hole tomography using evolutionary programming. Indian Journal of Petroleum Geology. 6(1): 77 - 86.

PARTIAL COPYRIGHT LICENSE

I hereby grant the right to lend my thesis to the users of the University of Victoria Library, and to make single copies only for such users or in response to a request from the Library of any other university, or similar institution, on its behalf or for one of its users. I further agree that permission for extensive copying of this thesis for scholarly purposes may be granted by me or a member of the University designated by me. It is understood that copying or publication of this thesis for financial gain shall not be allowed without my written permission.

Title of Thesis:

Marine gas hydrates: Seismic analyses and thermal regime

Author


Nilanjan Ganguly

December 14, 1998.